New Physics with Neutrinos

Dissertation zur Erlangung des Grades
"Doktor der Naturwissenschaften"
am Fachbereich Physik, Mathematik und Informatik
der Johannes Gutenberg-Universität
in Mainz

Mona Inge Dentler
geboren in München

Mainz, den 23.11.2018

Abstract

Due to open problems in theory and unresolved anomalies in various oscillation experiments, neutrino physics appears to be an excellent starting point in the quest for physics beyond the Standard Model (SM). The $3+1$ framework featuring an additional, sterile neutrino mixing with the known neutrinos, is a minimalist extension of the SM which can account for oscillation phenomenology beyond the standard three flavor paradigm. However, two orthogonal arguments militate against this model.

First, the increasing amount of ambiguous experimental results makes a consistent interpretation of the data in the $3+1$ framework appear unlikely. In this regard, global fits provide a useful tool to investigate this objection. This thesis reports on the results of an up-to-date global fit to all relevant, available datasets, including the data corresponding to the reactor antineutrino anomaly (RAA), the gallium anomaly and the short baseline (SBL) anomaly. The reactor data as a special case can plausibly be explained by the hypothesis of a misprediction of the reactor antineutrino flux. Therefore, this hypothesis is tested against the $3+1$ framework. Both hypotheses are found to be similarly likely, with a slight preference for the $3+1$ framework, mainly driven by the data from DANSS and NEOS, which measure antineutrino spectra. However, a combination of both hypotheses fits the data best, with the hypothesis of a mere misprediction of the reactor flux rejected at 2.9σ. Despite mild tensions, adding the remaining datasets in the $\overset{(-)}{\nu}_e$ disappearance channel increases the evidence for the $3+1$ framework to 3.2σ. This result is independent from any prediction on the reactor flux. Similarly, the data taken in the $\overset{(-)}{\nu}_e$ appearance channel favor the $3+1$ framework with a significance of up to 6.5σ, depending on the LSND datasets included, although the goodness of fit (GOF) is poor. These results are in strong contrast to the lack of evidence for the $3+1$ framework in the $\overset{(-)}{\nu}_\mu$ disappearance channel. Especially driven by the new results from IceCube and MINOS, this allows for rigorous constraints on the parameter space in the $\overset{(-)}{\nu}_\mu$ disappearance channel. The combined fit to the global data proves that the different subsets are incompatible with each other at the 4.7σ level. This tension is in particular driven by LSND and robust with regard to the choice of the fitted dataset and the underlying reactor flux model.

The second objection to the $3+1$ framework are the strong constraints on the effective number N_{eff} and the sum of masses $\sum m_\nu$ of neutrino-like particles implied by different cosmological probes. These constraints are in conflict with the presence of an additional, sterile neutrino species in the early universe. However, if their production was prevented throughout the evolution of the universe, the constraints from cosmology would not apply for sterile neutrinos. The generation of sterile neutrinos can be suppressed by a new type of interaction, termed “secret interaction”. Still, as this thesis confirms, the secret interaction model is disfavored in all of the viable parameter space. Therefore, inverse symmetry breaking, additional sterile neutrinos, additional free-streaming particles or neutrino decay are proposed as potential extensions of the secret interaction model.

Contents

List of tables

List of figures

List of abbreviations and acronyms

BBN	Big Bang nucleosynthesis	37
BFP	best fit point	48
BSM	Beyond Standard Model	23
CC	charged current	5
CCQE	charged-current quasi-elastic	78
CDM	cold dark matter	31
CL	confidence level	52
CMB	cosmic microwave background	37
DaR	decay at rest	67
DC	DeepCore	61
DiF	decay in flight	67
DOF	degree of freedom	30
EWS	electroweak symmetry breaking	7
FD	far detector	79
FTD	finite temperature and density	16
GOF	goodness of fit	iii
GR	general relativity	29
GUT	grand unified theory	98
IBD	inverse beta decay	49
IC	IceCube	61
IH	inverted hierarchy	13
ISW	integrated Sachs-Wolfe	42
LBL	long baseline	47
LHC	large hadron collider	1
LSS	large scale structure	41
MSW	Mikheyev-Smirnov-Wolfenstein	13
NC	neutral current	5

ND	near detector	57
NH	normal hierarchy	13
NuMI	Neutrinos at the Main Injector	79
PG	parameter goodness of fit	47
PMNS	Pontecorvo-Maki-Nakagawa-Sakata	6
PMT	photomultiplier tube	78
QCD	quantum chromodynamics	33
QED	quantum electrodynamics	97
QFT	quantum field theory	14
RAA	reactor antineutrino anomaly	iii
SBL	short baseline	iii
SK	SuperKamiokande	61
SM	Standard Model	iii
SPS	Super Proton Synchrotron	68
vev	vacuum expectation value	7

1 Introduction: boring and annoying?

Leaving the introduction to the topic of this thesis, neutrinos, to somebody who knows very well how to write about physics, these elementary particles can be characterized as follows:

> “Many a time I have stressed [. . .] that neutrinos are boring, though I should specify that they are boring from the point of view of a theoretical physicist.” [1]

This description of neutrinos was penned by the physicist Adam Falkowski, who writes as “Jester” in his witty, illuminating and knowledgeable blog “Résonaances” about various topics affecting the high energy physics community. While the above quotation quite probably should be taken as an humorous exaggeration, he certainly has a point there: On the event display of a particle detector, for example at the large hadron collider (LHC), neutrinos leave no tracks, they cause no spectacular jets or showers. They are light and stable on large timescales, they do not decay. Most of the time, neutrinos do not do anything at all, but traverse idly throughout the universe. Hence indeed, neutrinos appear rather boring.

Nevertheless, in the last decades, huge efforts have lead to sophisticated experiments that can actually measure the properties these particles, despite the rarity of interactions used to detect them. However, also from an experimental point of view, neutrinos do not seem to be very favorable objects, or, quoting once again “Jester”:

> “For experimentalists, on the other hand, neutrinos are first of all annoying. Indeed, taking part in a neutrino experiment seems the shortest path to trouble, because of weird anomalies affecting every other experiment.” [1]

In conclusion, the topic of this work could polemically be described as “boring and annoying”. This, of course, does not seem like a promising starting point. Yet, this thesis subscribes to a different point of view. The very properties that make neutrinos appear boring, the rarity of their interactions together with their tiny masses, are on the other hand properties that make neutrinos unique and interesting in the context of the SM. For instance, neutrinos are the only elementary particles for which the phenomenon of oscillations has been observed. The measurement of these oscillations, with ever increasing precision, has evolved into a fruitful field of research. The respective oscillation parameters may be related to questions as profound as why the universe consists mainly of matter and not equal parts antimatter. The properties of the neutrino also assign it a special role in the later history of the universe, because it is for example the only massive particle that becomes free-streaming very early on, which crucially impacts the formation of structures. Without neutrinos, the universe would not have evolved to the state we know. Furthermore, while neutrinos might feature fewer characteristic properties than other elementary particles, the theoretical modeling of these properties is much less well established. For example the exact mechanism that endows neutrinos with their tiny mass is currently not known and is almost inevitably related to new physics beyond the SM.

Quite contrary to the first quotation, it is hence very likely that neutrinos have the potential to reveal much about the universe and the law of physics governing it. However, to explore this potential, experiments need to measure neutrino properties to a high level of precision. Yet, while many great experimental results were achieved over the last decades, it is also true what is stated in the second quotation: there are indeed several experiments – both old and new – that apparently contradict the standard picture which can be extracted from the remaining data. While the cause for any of these anomalous results could in principal be something as annoying as a mere statistical fluke or a loose cable, it is also true that it is the unexpected results which often turn out to be the most interesting ones. Therefore, instead of considering them as an annoyance, in this work, the anomalies in various neutrino oscillation experiments are taken as an opportunity to develop and test new models beyond the SM.

Hence, countering the humorous quotations above, this thesis takes a stab at proving that neutrinos are neither boring nor annoying, but offer interesting opportunities for both theoretical and experimental exploration. This endeavor is organized as follows: chapter 2 introduces neutrinos in the context of the SM and presents their characteristic oscillation phenomenology. Furthermore, some open questions in the current theory of neutrinos, like the origin of the neutrino masses and the number of neutrino species are briefly discussed. Chapter 3 gives a short overview of the thermal history of the universe with a special regard to the crucial role of neutrino-like particles. Moreover, the most important cosmological probes and their sensitivity to characteristic neutrino properties are described. Chapter 4 reviews in detail the anomalies detected in various oscillation experiments. Motivated by these observations, the $3+1$ framework is introduced as a minimal extension of the SM. Based on the publications [2] and [3], this framework is subsequently tested on various subsets of the global oscillation data. The chapter concludes with a global fit of all datasets in the $3+1$ framework, revealing strong tensions among the different subsets. Irrespective of these tensions, the $3+1$ framework is also in conflict with the constraints on various properties of neutrinos imposed by cosmological probes. Based on the publication [4], chapter 5 reviews an extension of the $3 + 1$ model featuring an additional, "secret" interactions among the right-handed neutrinos. Subsequently, the incompatibility of this model with constraints arising from cosmological probes is carefully examined. The chapter concludes by proposing several extensions of the secret interaction scenario that potentially reconcile the $3 + 1$ model with cosmological constraints. Finally, chapter 6 provides a short summary of the results presented in this thesis.

2 Neutrino phenomenology

2.1 Neutrinos in the Standard Model

The SM describes three generations of neutrinos, labeled electron, muon and tau neutrino. Their interactions are specified by the terms

$$\mathcal{L} \supset \frac{g}{2\cos\theta_W} \sum_{\alpha=e,\mu,\tau} \bar{\nu}_\alpha \gamma^\mu P_\mathrm{L} \nu_\alpha Z^0_\mu + \frac{g}{\sqrt{2}} \sum_{\alpha=e,\mu,\tau} \bar{\ell}_\alpha \gamma^\mu P_\mathrm{L} \nu_\alpha W^+_\mu + \text{h.c.} \tag{2.1}$$

in the Lagrangian $\mathcal{L}$. These terms express the *weak interaction* of leptons, parametrized by the coupling constant g and the Weinberg angle θ_W. The weak interaction is mediated by the three gauge bosons Z^0, W^+ and $(W^+)^\dagger = W^-$, where the terms involving Z^0 are usually called *neutral current (NC) interactions* and the terms involving W^+ and W^- are usually called *charged current (CC) interactions*. The NC interaction couples two neutrino fields of the same type, denoted by $\overset{(-)}{\nu}_\alpha$ in eq. (2.1), while the CC interactions couple a neutrino field to a charged lepton field of the same type, denoted by $\overset{(-)}{\ell}_\alpha$ eq. (2.1). Remarkably, the weak interaction is maximally parity violating, to be specific, it couples only to left-handed fields or to the respective right-handed conjugated fields. This is reflected by the projection operator P_L in eq. (2.1), defined by

$$P_\mathrm{L} := \frac{1-\gamma_5}{2}, \tag{2.2}$$

which projects out the left-handed component of a field or the right-handed component of its conjugated field. The corresponding operator projecting out the right-handed component of a field or the left-handed component of its conjugated field is given by

$$P_\mathrm{R} := \frac{1+\gamma_5}{2}. \tag{2.3}$$

The weak interaction of neutrinos can equivalently be written as

$$\mathcal{L} \supset \frac{g}{2\cos\theta_W} \sum_i \bar{\nu}_i \gamma^\mu P_\mathrm{L} \nu_i Z^0_\mu + \frac{g}{\sqrt{2}} \sum_i \sum_{\alpha=e,\mu,\tau} \bar{\ell}_\alpha \gamma^\mu P_\mathrm{L} U_{\alpha i} \nu_i W^+_\mu + \text{h.c.}. \tag{2.4}$$

Compared to the form given in eq. (2.1), in the above expression eq. (2.4), the vector $\nu = (\nu_e, \nu_\mu, \nu_\tau)^T$ is transformed to the new basis $B = (\nu_1, \nu_2, \nu_3)$ by means of the unitary transformation matrix U, such that each field ν_α is given by the linear combination $\nu_\alpha = \sum_i U_{\alpha i}\nu_i$. Any general complex unitary matrix can be parametrized in terms of three angles and six phases as follows: [5, 6]

$$\begin{multline} U = \begin{pmatrix} 1 & 0 & 0 \\ 0 & e^{i(\epsilon-\gamma)} & 0 \\ 0 & 0 & e^{i(\zeta-\gamma)} \end{pmatrix} \\ \begin{pmatrix} c_{12}c_{13} & s_{12}c_{13} & s_{13}e^{-i\delta} \\ -s_{12}c_{23} - c_{12}s_{23}s_{13}e^{i\delta} & c_{12}c_{23} - s_{12}s_{23}s_{13}e^{i\delta} & s_{23}c_{13} \\ s_{12}s_{23} - c_{12}c_{23}s_{13}e^{i\delta} & -c_{12}s_{23} - s_{12}c_{23}s_{13}e^{i\delta} & c_{23}c_{13} \end{pmatrix} \\ \begin{pmatrix} e^{i\alpha} & 0 & 0 \\ 0 & e^{i\beta} & 0 \\ 0 & 0 & e^{i\gamma}, \end{pmatrix} \tag{2.5} \end{multline}$$

where the definitions $c_{ij} := \cos\theta_{ij}$ and $s_{ij} := \sin\theta_{ij}$ have been used. However, considering only the interaction Lagrangian eq. (2.1), each of the six fields $\overset{(-)}{\ell}_\alpha$, $\overset{(-)}{\nu}_i$ is invariant under the multiplication by a phase. Hence, by redefining these fields, the five phases factored out to the left and right in eq. (2.5) and parametized by α, β, γ, ϵ and ζ can be absorbed. After this transformation U is hence given given by

$$\begin{aligned} U &= \begin{pmatrix} c_{12}c_{13} & s_{12}c_{13} & s_{13}e^{-i\delta} \\ -s_{12}c_{23} - c_{12}s_{23}s_{13}e^{i\delta} & c_{12}c_{23} - s_{12}s_{23}s_{13}e^{i\delta} & s_{23}c_{13} \\ s_{12}s_{23} - c_{12}c_{23}s_{13}e^{i\delta} & -c_{12}s_{23} - s_{12}c_{23}s_{13}e^{i\delta} & c_{23}c_{13} \end{pmatrix}, \\ &= O_{23}(\theta_{23})\, V_{13}(\theta_{13},\delta)\, O_{12}(\theta_{12}) \end{aligned} \tag{2.6}$$

where $O_{ij}(\theta_{ij})$ denotes a real rotation matrix corresponding to a rotation in the (ij)-plane parametrized by the rotation angle θ_{ij}, and V_{13} denotes a complex rotation matrix parametrized by the angle θ_{13} and a phase δ. While it is not unique, the particular parametrization in terms of three real parameters expressed by angles and one complex parameter expressed by a phase, as given in eq. (2.6), is convenient and widely used [7].

At this point, the transformation performed in eq. (2.4) is arbitrary, since in the absence of further terms in the Lagrangian, the only physically observable entities are the fields ν_α, because these couple to the weak interaction. However, if further terms, which couple to the fields ν_i, are introduced in the Lagrangian, these fields also correspond to physical observables. Indeed, as the following section illustrates, the fields ν_i can be identified with fields of definite mass. In that case, the matrix U given in eq. (2.6) is usually called Pontecorvo-Maki-Nakagawa-Sakata (PMNS) or leptonic mixing matrix, and becomes in principal measurable by experiments.

2.2 Neutrino mass

Unlike the interaction terms in the SM Lagrangian reviewed above, the form of the neutrinos mass terms is not established. While the discovery of neutrino oscillations, awarded with the Nobel Prize in Physics 2015 for Takaaki Kajita and Arthur B. McDonald [8], proves that neutrinos indeed have masses, their values have neither been measured nor is the mechanism known that generates them. Arguably the most straightforward approach to give masses to neutrinos would be to adopt the same model as in the case of the other fermions, which leads after electroweak symmetry breaking (EWS) to a *Dirac mass term*

$$\begin{aligned}\sum_{\alpha,\beta=e,\mu,\tau} Y_{\alpha\beta}\frac{v}{\sqrt{2}}\,\overline{\nu_{\alpha\mathrm{R}}}\nu_{\beta\mathrm{L}} + \mathrm{h.c.} &= \sum_{\alpha,\beta}\sum_{i} V_{\alpha i} m^D_{ii} U^\dagger_{i\beta}\frac{v}{\sqrt{2}}\,\overline{\nu_{\alpha\mathrm{R}}}\nu_{\beta\mathrm{L}} + \mathrm{h.c.} \\ &=: \sum_i m^D_{ii}\left(\overline{\nu_{i\mathrm{R}}}\nu_{i\mathrm{L}} + \overline{\nu_{i\mathrm{L}}}\nu_{i\mathrm{R}}\right),\end{aligned}$$

where the variables $\nu_{\alpha\mathrm{L}}$ and $\nu_{\alpha\mathrm{R}}$ denote the left- and right-handed components of the field ν_α, given by $P_\mathrm{L}\nu_\alpha$ and $P_\mathrm{R}\nu_\alpha$, respectively, with the projection operators P_R and P_L defined in eqs. (2.2) and (2.3), and similarly for the conjugated fields. Furthermore, in the above equation, Y denotes the neutrino Yukawa matrix, which is a general, complex 3×3 matrix and v is the vacuum expectation value (vev) of the Higgs field. The diagonal, positive definite Dirac mass matrix $m^D = \mathrm{diag}(m_1, m_2, m_3)$ derives from the Yukawa matrix Y through the transformation $Yv/\sqrt{2} \equiv M^D = Vm^DU^\dagger$, where V and $U^\dagger$ are two unitary matrices. Note that such a transformation is always possible. In the last line of eq. (2.7) the definition

$$\nu_{i\mathrm{L}} = \sum_\alpha U^\dagger_{i\alpha}\nu_{\alpha\mathrm{L}} \tag{2.7}$$

$$\nu_{i\mathrm{R}} = \sum_\alpha V^\dagger_{i\alpha}\nu_{\alpha\mathrm{R}} \tag{2.8}$$

were used [9]. Hence, identifying the fields ν_i in eq. (2.7) with the corresponding fields in eq. (2.4), the matrix $U^\dagger$ in eq. (2.7) can be recognized as the adjugate of the matrix defined in eq. (2.6).

However, as can be seen in eq. (2.1), the right-handed fields $\nu_{\alpha\mathrm{R}}$ do not appear in the SM interaction Lagrangian describing the neutrino interactions, because the weak interaction is found to be maximally parity violating. This implies that the right-handed fields do not interact in the SM, hence they are called “sterile”. Since they do not interact in SM, there is no definite evidence that these fields actually exist, much less if the mechanism described above indeed generates the neutrino masses. Furthermore, experimental efforts to directly measure the neutrino mass have so far only resulted in upper limits. These limits, however, restrict neutrinos to be lighter than $\sim 2\,\mathrm{eV}$ [7, 10], which is orders of magnitude lower than the masses of all other SM particles. This implies that also the Yukawa coupling constants for neutrinos, which encode their interaction with the Higgs field, are much smaller than the corresponding coupling constants for all other SM particles. While this fact might just be a lusus naturae, it is often considered “unnatural”.

Irrespective of these considerations, the extension of the SM particle content by the right-handed neutrino fields $\nu_{\alpha\mathrm{R}}$ allows for a new term in the Lagrangian, given by [9]

$$\sum_{s,s'} \frac{1}{2} \overline{\nu_{s\mathrm{R}}} M^R_{ss'} (\nu_{s'\mathrm{R}})^c + \mathrm{h.c.} \tag{2.9}$$

In the above expression, the superscript c denotes the charge-conjugation operation, which converts a particle into its antiparticle. Furthermore, M^R is a complex matrix, which has to be symmetric, due to the properties of the charge conjugation [9]. The term given in eq. (2.9) is called Majorana mass term, because it can be constructed for particles which obey the Majorana condition

$$\psi = \psi^c, \tag{2.10}$$

that is, particles and antiparticles cannot be distinguished. This condition is fulfilled for right-handed neutrinos $\nu_{s\mathrm{R}}$ and their left-handed antiparticles $(\nu_{s\mathrm{R}})^c$, because they are assigned no quantum number that might distiguish particles from antiparticles [9]. Unless applying additional arguments, as for instance imposing further symmetries, the term eq. (2.9) is hence expected to contribute to the neutrino phenomenology. The two terms, eqs. (2.7) and (2.9) combined can be recast into a single term, as follows

$$\begin{aligned}
&\sum_{s,\alpha} \overline{\nu_{s\mathrm{R}}} M^D_{s\alpha} \nu_{\alpha\mathrm{L}} + \sum_{s,s'}^{N_s} \frac{1}{2} \overline{\nu_{s\mathrm{R}}} M^R_{ss'} (\nu_{s'\mathrm{R}})^c + \mathrm{h.c.} \\
=&\frac{1}{2} \sum_{s,\alpha} \overline{\nu_{s\mathrm{R}}} M^D_{s\alpha} \nu_{\alpha\mathrm{L}} + \frac{1}{2} \sum_{s,\alpha} \overline{(\nu_{\alpha\mathrm{L}})^c} (M^D)^T_{\alpha s} (\nu_{s\mathrm{R}})^c + \sum_{s,s'}^{N_s} \frac{1}{2} \overline{\nu_{s\mathrm{R}}} M^R_{ss'} (\nu_{s'\mathrm{R}})^c + \mathrm{h.c.} \\
=:&\frac{1}{2} \overline{(n_\mathrm{L})^c} M^{D+M} n_\mathrm{L} + \mathrm{h.c.},
\end{aligned} \tag{2.11}$$

where in the last line the column vector

$$n_\mathrm{L}^T := (\nu_{e\mathrm{L}}, \nu_{\mu\mathrm{L}}, \nu_{\tau\mathrm{L}}, (\nu_{s_1\mathrm{R}})^c, \ldots, (\nu_{N_s\mathrm{R}})^c) \tag{2.12}$$

was introduced. In the definition eq. (2.12), the expression $(\nu_{s_i\mathrm{R}})^c$ denotes the left-handed, sterile antiparticles of the right-handed sterile neutrinos $\nu_{s_i\mathrm{R}}$. Here, the number of SM neutrino species and the number of sterile neutrinos, N_s, are allowed to differ. Hence, unlike in eq. (2.7), the matrix $M^D_{s\alpha}$ is not required to be of square shape. Lastly, in the third line, the complex, symmetric $(3+N_s)\times(3+N_s)$ matrix was defined according to

$$M^{D+M} := \begin{pmatrix} 0 & (M^D)^T \\ M^D & M^R \end{pmatrix}. \tag{2.13}$$

The matrix M^{D+M} can be diagonalized with the unitary transformation matrix U, which results in the expression

$$\begin{aligned} &\frac{1}{2}\overline{(n_\mathrm{L})^c}(U^\dagger)^T M^{D+M} U^\dagger n_\mathrm{L} + \text{h.c.} \\ =&\frac{1}{2}\sum_i^{3+N_s} m_{ii}\overline{\nu_{i\mathrm{R}}}\nu_{i\mathrm{L}} + \text{h.c.} = \frac{1}{2}\sum_i^{3+N_s} m_{ii}\overline{N_i}N_i. \end{aligned} \tag{2.14}$$

In the last line the definitions

$$\nu_{i\mathrm{L}} := \sum_n^{3+N_s} U^\dagger_{in}\, n_{n\mathrm{L}} \tag{2.15}$$

$$\overline{\nu_{i\mathrm{R}}} := \sum_n^{3+N_s} \overline{(n_{n\mathrm{L}})^c}\, (U^\dagger)^T_{ni} = \sum_n^{3+N_s} (\overline{n_{n\mathrm{L}}} U_{ni})^c \tag{2.16}$$

and

$$N_i := \nu_{i\mathrm{L}} + \nu_{i\mathrm{R}} = (U^\dagger n_\mathrm{L})_i + ((U^\dagger n_\mathrm{L})^c)_i \tag{2.17}$$

were used. The fields N_i correspond to fields of definite mass $m_i := 1/2 m_{ii}$ and the fields $\nu_{i\mathrm{L}}$ and $\nu_{i\mathrm{R}}$ are their left- and right-handed components, respectively. Inserting the definition of the vector of left-handed fields, n_L, into eq. (2.15) gives

$$\nu_{i\mathrm{L}} = \sum_n^{3+N_s} U^\dagger_{in} n_{n\mathrm{L}} = \sum_{\beta=e,\mu,\tau} U^\dagger_{i\beta}\nu_{\beta\mathrm{L}} + \sum_{s'=s_1\ldots s_{N_s}} U^\dagger (\nu_{s'\mathrm{R}})^c. \tag{2.18}$$

Hence, the fields with definite mass are linear combinations of the fields ν_β, $\nu_{s'}$, which are the fields determined by the weak interaction. This equation can be inverted as follows

$$\sum_i^{3+N_s} U_{ni}\nu_{i\mathrm{L}} = n_{n\mathrm{L}} = \left\{ \begin{array}{lll} \nu_{\alpha\mathrm{L}} & n \leq 3, & \alpha \in \{e,\mu,\tau\} \\ (\nu_{sR})^c & n > 3, & s \in \{s_1 \ldots s_{N_s}\} \end{array} \right. . \tag{2.19}$$

Thus, the three left-handed SM neutrino field ν_α and the N_s left-handed, sterile neutrino fields $(\nu_{s\mathrm{R}})^c$, are linear combinations of the corresponding left-handed fields $\nu_{i\mathrm{L}}$ with definite mass. The respective equations for the antiparticles hold analogously. Similar equations could be listed for the right-handed fields as well. However, as noted above, these fields do not interact in the SM, and hence the corresponding expressions are irrelevant. Again, the fields ν_i in the above expression eq. (2.18) can be identified with the corresponding fields in the interaction Lagrangian eq. (2.4). In this case, the 3×3 sub-matrix $(U^\dagger)_{ij}$ with $1 \leq i, j \leq 3$ of the matrix $U^\dagger$ in eq. (2.18) is given by conjugate of the matrix U defined in eq. (2.5).

The mixing of different fields, expressed in eq. (2.19) can give rise to oscillations involving sterile neutrinos. This potential phenomenon is an interesting scenario beyond the SM. In fact, the neutrino oscillations in the presence of one sterile neutrino are a central part of this work and are discussed in detail in chapter 4.

Each of the fields N_i fulfills the Majorana condition eq. (2.10) [9]. Hence, although in the case at hand the SM model neutrinos feature a Dirac mass term, the Majorana mass term for the sterile neutrinos given in eq. (2.9) leads also to the Majorana term given in eq. (2.14) for fields of definite mass N_i. However, any field which obeys the Majorana condition given in eq. (2.9) is not invariant under the multiplication with a phase, since

$$\begin{aligned} &\psi \rightarrow \psi' = e^{-i\phi}\psi \\ &\psi^c \rightarrow \psi'^c = (e^{-i\phi}\psi)^c = e^{i\phi}\psi^c, \end{aligned} \tag{2.20}$$

and hence $\psi' = \psi'^c$ only for $\phi = 0$. But this in turn implies, that if neutrinos indeed have a Majorana mass term, the PMNS matrix introduced in section 2.1 features two additional phases, called Majorana phases. This is because out of the six generic phases of a complex unitary matrix, as parametrized in eq. (2.5), in this case only three phases can be absorbed by redefinition of the charged lepton fields.

Finally, while the model outlined above was introduced just as a straightforward implementation of a mass term for neutrinos, it furthermore might hint at an explanation for the peculiar fact that the neutrino masses are so much smaller than the masses of the other particles in the SM. As noted above, the term given in eq. (2.9) is expected to appear in the Lagrangian when right-handed neutrinos are introduced, unless explicitly forbidden by some additional constraints. However, this term is a priori not connected to a particular scale, by contrast to the Dirac mass term given in eq. (2.7), which is related to the value of the vev of the Higgs field. Hence, the entries of the matrix M^R in eq. (2.9) can exhibit arbitrary values. Furthermore, this term could arise due to some physical processes at very high energy scales. In this case the entries of the matrix M^R in eq. (2.9) are expected to be large compared to the entries of the Dirac mass matrix M^D, whose entries could be of the same order of magnitude as the corresponding matrix for the quarks. Then, the matrix M^{D+M} can be block-diagonalized according to [9]

$$W^T M^{D+M} W \simeq \begin{pmatrix} M_{\text{light}} & 0 \\ 0 & M_{\text{heavy}}, \end{pmatrix} \tag{2.21}$$

with a unitary transformation matrix W. The block-matrices in eq. (2.21) are given by

$$M_{\text{light}} \simeq -(M^D)^T (M^R)^{-1} M^D, \tag{2.22}$$

$$M_{\text{heavy}} \simeq M^R. \tag{2.23}$$

If the entries of M^R are very large, the entries of $(M^R)^{-1}$ are expected to be very small, and hence the entries of M_{light} are also expected to be accordingly small. The mechanism described above is one particular implementation of a general class of models, which are known by the name "see-saw" models.

2.3 Vacuum oscillations

As discussed above, the three generations of neutrinos stand out from the other elementary particles in the SM because of their tiny mass. While this peculiar fact might hint at some interesting underlying physics, the most important consequence from a phenomenological point of view is the occurrence of *neutrino oscillations*. This importance derives on the one hand from the crucial knowledge on neutrino properties provided by the measurement of oscillations, on the other hand oscillations are specific to neutrinos and are not observed with other elementary particles.

Physically, neutrino oscillations can be understood as interference phenomena between coherent superpositions of mass eigenstates. The superpositions of mass eigenstates come about in weak interactions, whose eigenstates are *flavor eigenstates*. Since in physical situations the production of a neutrino should be considered within a finite volume of space and during some finite time, the respective canonical conjugate variables momentum and energy feature an intrinsic uncertainty. The differences between the neutrino masses are so small that they are well within these uncertainties and hence the superposition of mass eigenstates has to be treated coherently.

Although neutrino oscillations are experimentally well established [7], their theoretical description is subtle and details are still debated on [11]. The standard approach, employed by many textbooks and introductory articles[1] is very convenient, because it allows to arrive straightforwardly at a result which turns out to be correct in all situation of current practical interest. However, this

---

[1] A couple of exemplary references employing the standard approach are enlisted in [11]

method relies on a number of assumptions, which are not necessarily satisfied. The usual starting point is to express a neutrino flavor state $|\nu_\alpha\rangle$ as a linear combination of mass eigenstates $|\mathbf{p}_{m_i}\rangle$, that is eigenstates of the free Hamiltonian, as follows:

$$|\nu_\alpha\rangle = \sum_i U^*_{\alpha i}\, |\mathbf{p}_{m_i}\rangle, \tag{2.24}$$

where $|\nu_\alpha\rangle$ is the one-particle eigenstate corresponding to the flavor α and $|\mathbf{p}_{m_i}\rangle$ is the one-particle eigenstate corresponding to the mass m_i and momentum $\mathbf{p}_{m_i}$. U denotes the unitary PMNS matrix introduced in eq. (2.4) in section 2.1. The amplitude for a neutrino to be detected again as flavor eigenstate at some space-time point $x = (T, \mathbf{L})$ is given by

$$\langle 0|\psi^\alpha(x) \sum_i U^*_{\alpha i}\, |\mathbf{p}_{m_i}\rangle,$$

where $\psi^\alpha(x)$ is the neutrino field operator corresponding to the flavor eigenstate α. Since neutrinos are fermions, $\psi^\alpha(x)$ should be a Dirac field. Yet, neutrinos of experimental interest are usual ultrarelativistic, such that up to corrections of order $\mathcal{O}(m/E)$ all but one of the spinor components are zero for a free particle [12]. Thus only one row of the above equation needs to be considered. Dropping therefore the spinor structure and treating $\psi^\alpha(x)$ as a scalar field $\psi^\alpha(x) \to \phi^\alpha(x)$ the amplitude becomes

$$\begin{aligned}\langle 0|\phi^\alpha(x) \sum_i U^*_{\alpha i}\, |\mathbf{p}_{m_i}\rangle =& \langle \mathbf{k}_{m_j}| \int \frac{d^3k}{(2\pi)^3 2E_\mathbf{k}} \sum_{i,j} U^*_{\alpha i} U_{\beta j} e^{-ik_{m_j}x}\, |\mathbf{p}_{m_i}\rangle \\ =& \sum_i U^*_{\alpha i} U_{\beta i}\, e^{-ip_{m_i}x}\end{aligned} \tag{2.25}$$

and hence the probability reads

$$\begin{aligned}|\langle 0|\phi^\alpha(x) \sum_i U^*_{\alpha i}\, |\mathbf{p}_{m_i}\rangle|^2 =& \sum_{i,k} U^*_{\alpha i} U_{\beta i} U_{\alpha k} U^*_{\beta k}\, e^{-ip_{m_i}x} e^{ip_{m_k}x} \\ =& \sum_{i,k} U^*_{\alpha i} U_{\beta i} U_{\alpha k} U^*_{\beta k}\, e^{-i(E_{m_i}-E_{m_k})T + i(\mathbf{p}_{m_i}-\mathbf{p}_{m_k})\mathbf{L}}.\end{aligned} \tag{2.26}$$

To arrive at the "standard oscillation formula", at this point further assumptions are needed. For instance, the "equal energy prescription" requires all mass eigenstates to have the same energy, that is $E_{m_k} = E$ holds for all m_k. With this prescription the time-dependence drops out. Assuming furthermore that $\mathbf{p}_{m_i}$ is parallel to $\mathbf{p}_{m_k}$ for all i, k and taking $\mathbf{L}$ in the direction of $\mathbf{p}_{m_i}$, $\mathbf{p}_{m_k}$, gives the standard oscillation formula

$$\begin{aligned} P_{\alpha\beta}(L) \equiv \left| \sum_i U^*_{\alpha i} U_{\beta i}\, e^{i|\mathbf{p}_{m_i}|L} \right|^2 &= \sum_{i,k} U^*_{\alpha i} U_{\beta i} U_{\alpha k} U^*_{\beta k}\, e^{i(|\mathbf{p}_{m_i}|-|\mathbf{p}_{m_k}|)L} \\ &\simeq \sum_{i,k} U^*_{\alpha i} U_{\beta i} U_{\alpha k} U^*_{\beta k}\, e^{\frac{-i\Delta m^2_{ik} L}{2E}}, \end{aligned} \tag{2.27}$$

where Δm^2_{ik} is defined by $\Delta m^2_{ik} := m_i^2 - m_k^2$, and $L = |\mathbf{L}|$. In the second line, the expression $|\mathbf{p}_{m_i}| - |\mathbf{p}_{m_k}| = \sqrt{E^2 - m_i^2} - \sqrt{E^2 - m_k^2}$ has been expanded assuming that the masses are small compared to $E \gg m_i,\, m_k$.

For *antineutrinos*, using the linear decomposition of a flavor eigenstate

$$|\bar{\nu}_\alpha\rangle = \sum_i U_{\alpha i}\, |\mathbf{p}_{m_i}\rangle, \tag{2.28}$$

an analogue calculation yields

$$P_{\bar{\alpha}\bar{\beta}}(L) = \sum_{i,k} U_{\alpha i} U^*_{\beta i} U^*_{\alpha k} U_{\beta k}\, e^{\frac{-i\Delta m^2_{ik} L}{2E}}. \tag{2.29}$$

The above expressions of the “standard oscillation probability” depend on the four parameters of the PMNS matrix and two mass-squared differences, since the third mass-squared difference can be expressed in terms of the remaining two. The current best fit values for these six parameters are summarized in table 2.1. Since the above formula depends only on mass-squared differences, the absolute neutrino masses cannot be determined from oscillation experiments in principle. However, from measurements of neutrinos from the sun undergoing the Mikheyev-Smirnov-Wolfenstein (MSW) effect (c.f. section 2.4) it is known that the mass eigenstate m_1 is lighter than the mass eigenstate m_2. For the third mass eigenstate, m_3, it is currently not resolved if it is lighter or heavier than the other two mass eigenstates. Since m_1 consists mostly of electron flavor, by analogy to the charged leptons, it would be “normal” that it was the lightest state. This hypothesis is therefore dubbed normal hierarchy (NH). The inverse case, where m_3 would be the lightest state, accordingly is dubbed inverted hierarchy (IH).

The oscillation probabilities given in eqs. (2.27) and (2.29) are obviously invariant under the transformation [9]

$$U_{\alpha i} \to e^{-i\phi_\alpha} U_{\alpha i} e^{i\phi_i} \tag{2.30}$$

of each entry $U_{\alpha i}$ of the PMNS matrix U. This implies in particular that the oscillation probability is not sensitive to the additional phases that cannot be

parameter	value NH	value IH
Δm^2_{21}	$7.37 \times 10^{-5}\,\mathrm{eV}^2$	
$\sin^2\theta_{12}$	0.297	
$\|\Delta m^2_{31}\|$	$2.56 \times 10^{-3}\,\mathrm{eV}^2$	$2.54 \times 10^{-3}\,\mathrm{eV}^2$
$\sin^2\theta_{23}$	0.425	0.589
$\sin^2\theta_{13}$	0.0215	0.0216
δ/π	1.38	1.31

Table 2.1: Best fit values of the oscillation parameters [7]. According to the convention followed here, Δm^2_{31} always refers to difference between the mass eigenstate consisting mostly of the electron flavor state, defined to be m_1, and the mass eigenstate m_3.

absorbed in the case discussed in section 2.2, where the fields of definite mass are Majorana fields. Thus, as respects the oscillation probability, only one phase is observable, and hence the parametrization given in eq. (2.6) is sufficient to fully characterize the PMNS matrix.

As stated above, the “standard oscillation formulas” eqs. (2.27) and (2.29) have been well confirmed in experiments [7], yet the above derivation should be taken with great caution. First, the “equal energy prescription” employed in eq. (2.27) is not fulfilled in most experimental situations, that is, there is no definite reason to assume that all mass eigenstates are produced with exactly the same energy. The argument could thus be adapted by taking into account that the production time and the production energy are not very well measured, such that the appropriate prescription is in fact averaging over these quantities. The second point is more profound. Treating the neutrino states as plane waves is actually contradicting the concept of oscillations in space, as a particle with definite momentum $\mathbf{p}_{m_i}$ would not be localized at all. Furthermore, because the uncertainty on the momentum for a plane wave is zero, no coherent superposition of such states would be possible. Therefore a theoretically much more convincing formalism is to describe the particles by quantum-mechanical wave packages. However, in this formalism the form of the wave packages has to be postulated, since the production of a particle can not be modeled in such a quantum mechanical approach [13]. Hence the most consistent description needs to be done in the full quantum field theory (QFT) framework. In this case, the particle production, propagation and detection are treated as one process. If the neutrinos are ultrarelativistic and their relative momenta are small compared to the momentum uncertainty, the respective amplitude factorizes. In this case, the amplitude corresponding to the propagation between the source and the detector, and hence the oscillation probability, can be extracted [13].

Since this work explores (new) phenomenology of neutrinos analyzing data from existing experiments or from cosmology, establishing a consistent theoretical framework for neutrino oscillations is beyond its scope. For a review of the different approaches to neutrino oscillations, their range of validity and possibly new phenomenology in future types of experiments c.f. for example [14]. Within this work, the "standard oscillation formulas" for neutrinos and antineutrinos, established in eq. (2.27) and eq. (2.29) are assumed to hold to very good approximation. Accordingly, the respective expressions previously dubbed "standard oscillation probabilities", are just called oscillation probabilities below.

When studying the phenomenology of neutrino oscillations, a useful way to recast the oscillation probability is given by

$$\begin{aligned} P_{\overset{(-)}{\alpha}\overset{(-)}{\beta}} = \delta_{\alpha\beta} - 4\sum_{i>j} \mathrm{Re}\left[(W_{ij}^{\alpha\beta})^{(*)}\right] \sin^2\left(\frac{\Delta m_{ij}^2 L}{4E}\right) \\ +2\sum_{i>j} \mathrm{Im}\left[(W_{ij}^{\alpha\beta})^{(*)}\right] \sin\left(\frac{\Delta m_{ij}^2 L}{2E}\right), \end{aligned} \qquad (2.31)$$

where $W_{ij}^{\alpha\beta}$ corresponds to the neutrino case, and $(W_{ij}^{\alpha\beta})^*$ to the antineutrino case and $W_{ij}^{\alpha\beta} = (U_{\alpha i}^* U_{\beta i} U_{\alpha j} U_{\beta j}^*)$ denotes the product of elements of the PMNS matrix, appearing in eq. (2.27). From this parametrization it is obvious that the oscillatory behavior of the detection probability is governed by the mass-squared differences Δm_{ij}^2, while the respective amplitudes are determined by $(W_{ij}^{\alpha\beta})^{(*)}$ and thus by the entries of the mixing matrix.

The parametrization given in eq. (2.31) furthermore reveals that a difference between the probability for an oscillation of a state of flavor α to a flavor β and the probability for an oscillation of the respective antiparticles, that is $P_{\alpha\beta} - P_{\bar{\alpha}\bar{\beta}}$, is only different from zero if

$$J_{ij}^{\alpha\beta} := \mathrm{Im}[(W_{ij}^{\alpha\beta})] \neq 0 \qquad\qquad \alpha \neq \beta, i \neq j, \qquad (2.32)$$

where J is known as Jarlskog invariant in the literature [15]. This case would imply CP violation. In the parametrization of the PMNS matrix given in eq. (2.6), J reads

$$J = \cos\theta_{12} \sin\theta_{12} \cos\theta_{23} \sin\theta_{23} \cos^2\theta_{13} \sin\theta_{13} \sin\delta, \qquad (2.33)$$

thus, if any of the mixing angles or the phase is zero, J is zero, and hence CP is conserved. Since J is invariant under rephasing of the neutrino field, the above statement is actually independent of the parametrization of the PMNS matrix.

In genuine experimental situations, it is often impossible to resolve all six parameters on which the oscillation probability depends. Therefore it is often justified to make further approximations that lead to simplifications of the expression for the oscillation probability. For example, as can be seen in table 2.1, $|\Delta m^2_{31}|$ is much larger than $|\Delta m^2_{21}|$. If L/E is of order $\mathcal{O}(L/E) \lesssim 1$, $|\Delta m^2_{21}|$ can be neglected compared to $|\Delta m^2_{31}| := \Delta m^2$ and $|\Delta m^2_{32}| = |\Delta m^2_{31}| - |\Delta m^2_{21}| \simeq |\Delta m^2|$, which gives the effective probability

$$P_{\overset{(-)}{\alpha}\overset{(-)}{\beta}} = \delta_{\alpha\beta} - 4|U_{\alpha 3}|^2 |U_{\beta 3}|^2 \sin^2\left(\frac{\Delta m^2 L}{4E}\right). \tag{2.34}$$

Examining once again table 2.1, $\sin^2\theta_{13}$ is observed to be small compared to the other parameters of the PMNS matrix. Approximating $\sin^2\theta_{13}$ therefore by zero leads to an effective two-flavor oscillation probability expressed by

$$\begin{aligned} P^{2\nu}_{\overset{(-)}{\mu}\overset{(-)}{\tau}} = P^{2\nu}_{\overset{(-)}{\tau}\overset{(-)}{\mu}} &= 1 - \sin^2(2\theta)\sin^2\left(\frac{\Delta m^2 L}{4E}\right) \\ P^{2\nu}_{\overset{(-)}{\mu}\overset{(-)}{\mu}} = P^{2\nu}_{\overset{(-)}{\tau}\overset{(-)}{\tau}} &= \sin^2(2\theta)\sin^2\left(\frac{\Delta m^2 L}{4E}\right), \end{aligned} \tag{2.35}$$

where $\theta \equiv \theta_{23}$ is the only parameter the mixing matrix $U^{2\nu}$ depends on in this case. Explicitly, $U^{2\nu} = (U^{2\nu\,\dagger})^T$ is given by

$$U^{2\nu} \equiv \begin{pmatrix} \cos\theta & \sin\theta \\ -\sin\theta & \cos\theta \end{pmatrix}. \tag{2.36}$$

This approximation describes very well experiments measuring muon neutrinos produced in the atmosphere. For different experimental situations, and thus for example different settings of the parameter L/E, different approximations are appropriate, leading to different versions of the two-flavor limit.

2.4 Oscillations at finite temperatures and densities

Since neutrinos infamously interact only weakly, it might seem a hopeless venture exploring the interactions of a test neutrino propagating through a background of finite density, unless considering very high energies. Interestingly, this is not necessarily the case when considering *forward scattering* between background particles and a test neutrino, as will be outlined below.

In contrast to the discussion in section 2.3, the phase-space is now populated by background particles of finite temperature and density (FTD). Typical examples for these background particles include electrons and nucleons for a test neutrino propagating through the earth or the sun. In astrophysical environments, also backgrounds made up by neutrinos of the same or a different flavor possibly need to be taken into account. For each background species, the

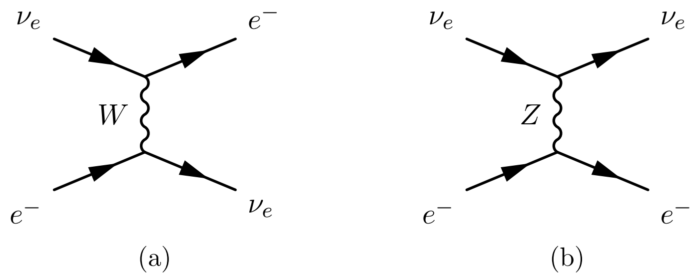

Figure 2.1: Diagrams contributing to the scattering of a test electron neutrino off a background electron due to CC (a) and NC (b) interactions[2]

respective temperature specifies the distribution function given by

$$\begin{aligned} n_f^{\pm}(p) &= \left[e^{(|p\cdot u| \mp \mu)/T} + 1\right]^{-1} \\ n_b^{\pm}(p) &= \left[e^{(|p\cdot u| \mp \mu)/T} - 1\right]^{-1}, \end{aligned} \tag{2.37}$$

with μ the chemical potential. The above equations determine the probability of a state being occupied. The subscript f (b) refers to fermions (bosons) and the superscript $+$ ($-$) refers to particles (antiparticles). The variable u denotes the 4-momentum of the heat bath of the respective particle species [16]. The test neutrino can interact with the background particles by exchange of a gauge boson. In the SM, this would be the W or Z boson, yet the concept remains valid also for a new, heavy vector mediator, as will be discussed in chapter 5.

A particular case is an interaction, at which the pair of ingoing and outgoing test neutrino and background particle each have exactly the same momentum, corresponding to forward scattering of the test neutrino. But such an interaction implicates that it cannot be resolved on which of the background particles the scattering event happens. Therefore in order to calculate the probability that a test neutrino interacts with a background particle at a point through forward scattering, one needs to sum up the scattering off any background particle at that point *coherently.* Thus the interaction probability in the case of forward scattering is proportional to the number density of background particles *squared*, in contrast to scattering with momentum transfer, where the interaction probability increases only linearly with the number density [17].

As a case study, let the test neutrino be an electron neutrino moving through a background of electrons, with the energies of the particles being small compared to the weak interaction gauge boson masses m_i, with $i = W, Z$. The boson propagator can then be expanded to give [16]

$$D_{\mu\nu}(\Delta) \simeq \frac{g_{\mu\nu}}{m_i^2} + \frac{g_{\mu\nu}\Delta^2 - \Delta_\mu \Delta_\nu}{m_i^4}, \tag{2.38}$$

---

[2] The Feynman diagrams shown in this thesis were produced with the LaTeX feynMP package.

with Δ denoting the momentum transferred, and m_i denoting the gauge boson masses. Using only the lowest order term of the expansion eq. (2.38), the tree-level matrix element for the interaction between a test neutrino of momentum k and a background electron of momentum p is given by

$$\begin{aligned}\mathcal{M} &= -\frac{g^2}{8m_W^2}\left[\bar{u}(k)\gamma_\mu(1-\gamma_5)u(p)\right]\left[\bar{u}(p)\gamma^\mu(1-\gamma_5)u(k)\right] \\ &= -\frac{G_F}{\sqrt{2}}\left[\bar{u}(k)\gamma_\mu(1-\gamma_5)u(k)\right]\left[\bar{u}(p)\gamma^\mu(1-\gamma_5)u(p)\right] \qquad (2.39)\end{aligned}$$

for a CC interaction, where g is the weak coupling constant and m_W^2 is the mass of the W. In the second line, the definition of the Fermi constant $G_F := \sqrt{2}g^2/(8m_W^2)$ has been inserted and a Fierz transformation has been applied. In the case of a NC interaction, the matrix element reads

$$\mathcal{M} = \frac{G_F}{2\sqrt{2}}\left[\bar{u}(k)\gamma_\mu(1-\gamma_5)u(k)\right]\left[\bar{u}(p)\gamma^\mu(1-\gamma_5-4\sin^2\theta_W)u(p)\right], \qquad (2.40)$$

with θ_W denoting the Weinberg angle. The tree-level diagrams corresponding to these matrix elements are shown in fig. 2.1.

As discussed above, to calculate the scattering amplitude, the matrix elements for all background particles need to be summed up coherently. These background particles are distributed among the states $|p\rangle$, corresponding to their respective momentum p, according to eq. (2.37). The orientation of the spins of the particles follows some distribution $f(s)$. Therefore summing over all background particles amounts to calculating

$$\begin{aligned}&-\frac{G_F}{\sqrt{2}}\int\frac{d^3p}{(2\pi)^3 2E_{\mathbf{p}}}n_f^+(p)\sum_s f(s)\left[\bar{u}^s(k)\gamma_\mu(1-\gamma_5)u^s(k)\right]\left[\bar{u}(p)\gamma^\mu(1-\gamma_5)u(p)\right] \\ &= -\frac{G_F}{\sqrt{2}}\int\frac{d^3p}{(2\pi)^3 2E_{\mathbf{p}}}n_f^+(p)\frac{1}{2}\,4p^\mu\left[\bar{u}(k)\gamma_\mu(1-\gamma_5)u(k)\right] \qquad \text{(medium unpolarized)} \\ &= -\frac{G_F}{\sqrt{2}}N_e\left[\bar{u}(k)\gamma_0(1-\gamma_5)u(k)\right], \qquad \text{(medium isotropic)}\end{aligned} \qquad (2.41)$$

for the CC matrix element given by eq. (2.39). In the equation above, N_e denotes the electron number density, defined by $N_e = \int n_f^+(p)\,D(p)d^3p$, with $D(p)$ the density of states. The second line follows assuming that the electron background is not polarized, i.e. $f(s) = 1/2$. The equality in the third line holds assuming that the momenta of the background electrons are distributed isotropically. Repeating the calculation for the NC matrix element, given by eq. (2.40), yields

$$\frac{G_F}{2\sqrt{2}}(1-4\sin^2\theta_W)\,N_e\left[\bar{u}(k)\gamma_0(1-\gamma_5)u(k)\right]. \qquad (2.42)$$

In the discussion so far, only the lowest order of the expansion of the boson propagator has been considered. Taking into account the next order in the expansion eq. (2.38) and assuming relativistic electrons, the term

$$-\frac{7\sqrt{2}\pi^2 G_F E_\nu}{90 m_W^2} T^4 \; [\bar{u}(k)\gamma_0(1-\gamma_5)u(k)] \tag{2.43}$$

needs to be added [16]. Interestingly, the expression above explicitly depends on the temperature T of the background medium, an effect that will become important in the framework to be discussed in chapter 5.

The expressions derived above can of course be evaluated. Yet, for the following discussion, it is more interesting to focus on a different point of view. In fact, the expressions eq. (2.41) and eq. (2.42), leaving aside the higher order term eq. (2.43) for the sake of clarity, can be interpreted as the matrix element describing the *effective interaction* corresponding to the Lagrangian [18]

$$\begin{aligned}
\mathcal{L}^{\text{eff}} \supset & \sum_{\alpha,\beta} \sqrt{2} G_F \left(\tfrac{1}{2} + 2\sin^2\theta_W\right) N_e \delta_{\alpha e}\delta_{\beta e} \bar{\nu}_{\alpha \mathrm{L}} \gamma_0 \nu_{\beta \mathrm{L}} \\
= & \sum_{i,j}\sum_{\alpha,\beta} \sqrt{2} G_F \left(\tfrac{1}{2} + 2\sin^2\theta_W\right) N_e \delta_{\alpha e}\delta_{\beta e} \bar{\nu}_{i\mathrm{L}} U^*_{i\alpha} \gamma_0 U_{\beta j} \nu_{j\mathrm{L}} \\
=: & \sum_{i,j}\sum_{\alpha,\beta} U^*_{i\alpha} (-\tilde{b})_{\alpha\beta} U_{\beta j} \bar{\nu}_{i\mathrm{L}} \gamma_0 \nu_{j\mathrm{L}} =: \sum_{i,j} (-b)_{ij} \bar{\nu}_{i\mathrm{L}} \gamma_0 \nu_{j\mathrm{L}} \\
\simeq & - b \bar{\nu}_{1\mathrm{L}} \gamma_0 \nu_{1\mathrm{L}}.
\end{aligned} \tag{2.44}$$

The first line in the expression above is denoted in the flavor basis, which was used implicitly above, whereas from the first to the second line, the basis is changed to the mass basis. The approximation in the last line relies on the fact the state corresponding to the mass eigenstate m_1 consists predominantly of electron flavor and $U_{1e} \gg U_{2e}, U_{3e} \sim 0$.

Consistent with the discussion above, this Lagrangian denotes an instance of forward scattering of a test neutrino off a background of electrons. Yet, by the very same line of argument as before, it cannot be determined how often the test neutrino scatters along its trajectory through the medium. Therefore, to calculate the amplitude for a test neutrino to propagate through the medium, the amplitude for propagation without scattering, the amplitude for propagation with scattering at one point, up to the amplitude of propagation with scattering at each point of the trajectory need to be summed up coherently, which can be expressed as follows:[3]

$$\frac{i(\not{p}+m)}{p^2-m^2} + \frac{i(\not{p}+m)}{p^2-m^2}(ib\gamma_0 P_L)\frac{i(\not{p}+m)}{p^2-m^2} + \cdots = \frac{i}{\not{p} - m + b\gamma_0 P_L}, \tag{2.45}$$

---

[3] The following expression applies only if the density of the background particles is constant. If the density is varying in space, one would formally need to transform to position space[19]

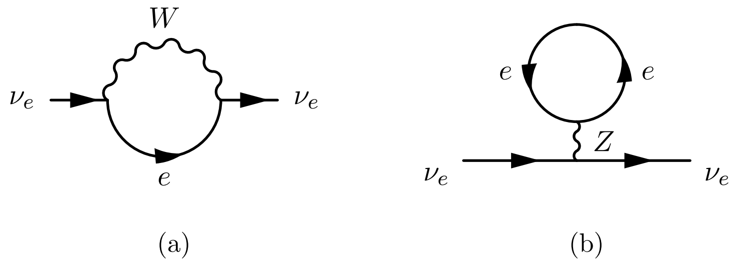

Figure 2.2: Diagrams contributing to the self-energy of an electron neutrino: bubble diagram (a) and tadpole diagram (b).

for a neutrino of momentum p and mass m, where the projection operator on left-handed states is denoted by $P_L := 1/2(1-\gamma_5)$. The equality follows from inserting the limit of the geometric series [19].

Equation (2.45) exhibits the modified propagator of an electron neutrino due to forward scattering in a bath of electrons at FTD. In the case at hand, the neutrino self-energy is given by

$$\Sigma = m - b\gamma_0 P_L = m - b\not{u} P_L, \tag{2.46}$$

where the second equality holds in the rest frame of the background bath, such that $u = (1,0,0,0)$. Repeating the calculation in eq. (2.45) for *antineutrinos* gives an additional minus-sign for the self-energy. The dispersion relation, given by

$$\det\big[\not{p} - \Sigma\big] = 0, \tag{2.47}$$

can be expanded in the ultrarelativistic limit $|b|$, $m \ll |\mathbf{p}| \approx p_0$ to give

$$p^0 = |\mathbf{p}| \pm \frac{m^2}{2|\mathbf{p}|} \mp b, \tag{2.48}$$

where the upper sign refers to neutrinos and the lower sign to antineutrinos. This equation manifests that the term b just adds to the total energy of the test particle, thus b acts as an effective potential

$$V_{\text{eff}} \equiv \mp b = \pm\sqrt{2} G_F \left(\tfrac{1}{2} + 2\sin^2\theta_W\right) N_e. \tag{2.49}$$

The different sign for neutrinos and antineutrinos can be understood from the fact that a force between two fermions of like charges, mediated by a vector boson, is repelling, while a force between two fermions of unlike charges is attractive [16].

The discussion so far was only concerned with the change in the self-energy due to scattering off the thermal background. But in fact the self-energy also receives contributions in vacuum, which are given by the loop corrections to the propagator. Two of the relevant diagrams at one loop order are depicted in fig. 2.2. Writing out the contribution Σ_0^{CC} of the first diagram fig. 2.2 (a) to the vacuum self-energy Σ_0 explicitly gives

$$\begin{aligned}-i\Sigma_0^{CC} &= -\frac{G_F}{\sqrt{2}}\int \frac{d^4p}{(2\pi)^4}\,\gamma^\mu(1-\gamma_5)\frac{i(\not{p}+m)}{p^2-m^2}\gamma_\mu(1-\gamma_5)\\ &= -\frac{G_F}{\sqrt{2}}\int \frac{d^4p}{(2\pi)^4}\,\gamma^\mu(1-\gamma_5)iS_0(p)\gamma_\mu(1-\gamma_5),\end{aligned} \tag{2.50}$$

where again the low energy expansion of the W propagator eq. (2.38) was used. iS_0 denotes the fermion propagator in vacuum. Formally, the expressions found above for the scattering matrix elements at FTD can be brought into a form similar to the one loop self-energy in vacuum. Considering for instance the CC interaction term, eq. (2.41) can be rearranged as follows:

$$\begin{aligned}&-\frac{G_F}{\sqrt{2}}\int \frac{d^3p}{(2\pi)^3 2E_{\mathbf{p}}} n_f^+(p)\frac{1}{2}\,4p^\mu\;[\bar{u}(k)\gamma_\mu(1-\gamma_5)u(k)]\\ &=\bar{u}(k)\left[-\frac{G_F}{\sqrt{2}}\int\frac{d^4p}{(2\pi)^4}\gamma^\mu(1-\gamma_5)n_f^+(p)i^2 2\pi\delta(p^2-m^2)(\not{p}+m)\gamma_\mu(1-\gamma_5)\right]u(k)\\ &\equiv\bar{u}(k)\left[-\frac{G_F}{\sqrt{2}}\int\frac{d^4p}{(2\pi)^4}\gamma^\mu(1-\gamma_5)i\Delta S_{FTD}(p)\gamma_\mu(1-\gamma_5)\right]u(k).\end{aligned} \tag{2.51}$$

The term in square brackets can now straightforwardly be interpreted as a contribution to the self-energy at FTD. Adding eqs. (2.50) and (2.51) gives the following contribution to the self-energy:

$$-i\Sigma_{FTD}^{CC} = -\frac{G_F}{\sqrt{2}}\int\frac{d^4p}{(2\pi)^4}\gamma^\mu(1-\gamma_5)iS_{FTD}(p)\gamma_\mu(1-\gamma_5), \tag{2.52}$$

and similarly, considering the NC terms in the scattering matrix and the vacuum self-energy, respectively, gives

$$-i\Sigma_{FTD}^{NC} = \frac{G_F}{2\sqrt{2}}\gamma_\mu(1-\gamma_5)\int\frac{d^4p}{(2\pi)^4}\mathrm{tr}\left[\gamma^\mu(1-\gamma_5-4\sin^2\theta_W)iS_{FTD}(p)\right], \tag{2.53}$$

where $iS_{FTD}(p)$ denotes the fermion propagator at FTD in the real time formalism given by [16]

$$\begin{aligned}S_{FTD}(p) &= S_0(p) + \Delta S_{FTD}(p)\\ &:= (\not{p}+m)\left[\frac{1}{p^2-m^2} + i2\pi\delta(p^2-m^2)\left[\theta(p^0)n_f^+ + \theta(-p^0)n_f^-\right]\right].\end{aligned} \tag{2.54}$$

Thus the fermion propagator $iS_{FTD}(p)$ at FTD is just the usual vacuum propagator iS_0, supplemented by the thermal correction $i\Delta S_{FTD}$. Below it shall be deemed that all quantities are *renormalized* such that the contributions due to loop corrections in vacuum exactly vanish at one loop order for an on-shell neutrino. Thus the neutrino propagator eq. (2.45) and the dispersion relation eq. (2.47) are not affected by loop corrections in vacuum.

The conclusion of the discussion above is that obviously two different approaches lead to the same result for the self-energy of the neutrino at FTD to lowest order: on the one hand, these corrections can be calculated directly by considering scattering off background particles at tree level and subsequently summing coherently over all background states. Alternatively, the same result can be obtained by calculating the one-loop corrections to the neutrino propagator and using the FTD correction $i\Delta S_{FTD}$ for the internal fermion propagator.

Of course this correspondence between the two approaches is no coincidence. Comparing the diagrams in fig. 2.1 and fig. 2.2, obviously the scattering diagrams fig. 2.1 (a) and (b) can be produced from the respective loop diagrams in fig. 2.2 by cutting the electron propagator. This equivalence has to be understood by analogy with the optical theorem, which relates the imaginary part of the matrix element of a loop diagram to the combination of the two subdiagrams resulting from cutting the loop [20]. The imaginary part of the matrix element can be obtained by replacing in the internal propagators $1/(p_i^2 - m_i^2 + i\epsilon)$ by delta functions $-2i\pi\delta(p_i^2 - m_i^2)$. Physically, this can be interpreted as setting the internal particles on shell. The optical theorem thus states that a loop process with the internal particles set on shell can equivalently be considered as two consecutive processes, where the initial particles go to some intermediate state particles which then in a second process go to the final particles, and the contribution of all possible intermediate particles are summed over.

Since the thermal part of the propagator, $i\Delta S_{FTD}$, is defined such that the usual denominator of the propagator is substituted by $2i\pi\delta(p_i^2 - m_i^2)$ times the distribution function $n_f^{\pm}$, a similar line of argument as for the optical theorem can be used to relate the loop diagrams in fig. 2.2 to the scattering diagrams in fig. 2.1. In fact, calculating the matrix element for the diagrams in fig. 2.2, using $i\Delta S_{FTD}$ for one of the propagators, sets the respective particle on shell. The matrix element can then be equivalently understood as a sum, weighted by $n_f^{\pm}$, over all possible states corresponding to these particles, which are now considered external. This discussion demonstrates the physical implication of the thermal propagator defined in eq. (2.54), yet it is intended to motivate rather than to derive the expression for the thermal propagator. For a more complete treatment of the thermal propagator within the framework of the real time formalism c.f. for example [21].

The above analysis of the effect of a thermal background on the propagation of a test neutrino was restricted to the case of the test electron (anti)neutrino forward scattering off a background of electrons. Of course the scattering of neutrinos of any flavor off any kind of backgrounds is equally interesting. Repeating the above calculations for these cases is straightforward. However, starting from general considerations on Lorentz invariance, it can be derived that at one-loop level, the self-energy is given by [22][4]

$$\pm\Sigma(p) = m - (a\not{p} + b\not{u})P_L, \tag{2.55}$$

where a, b are Lorentz-invariant functions, and the upper sign refers to neutrinos while the lower sign refers to antineutrinos, which generalizes the result eq. (2.46).

Evaluating the dispersion relation eq. (2.47) for the general self-energy eq. (2.55) in the ultrarelativistic limit $|b|$, $|a|$, $m \ll |\mathbf{p}| \approx p_0$ to lowest order in small quantities does not alter the result found in eq. (2.48). This means, to lowest order, also in the general case given in eq. (2.55), the dispersion relation of a (anti)neutrino gets corrected only by a potential energy term $V_{\text{eff}} \equiv \mp b$, where b can be extracted from the general self-energy eq. (2.55) by the following equation:

$$b = \frac{1}{2\mathbf{p}^2}\Big[\big[(p^0)^2 - \mathbf{p}^2\big]\mathrm{tr}\big(\not{u}\Sigma(p)\big) - p^0\mathrm{tr}\big(\not{p}\Sigma(p)\big)\Big]. \tag{2.56}$$

The change in the dispersion relation at FTD is very sensitively probed by neutrino oscillations. As discussed in section 2.3, neutrino oscillations are an interference phenomenon due to slightly different dispersion relations of the different mass eigenstates. Therefore a change in the dispersion relation changes the interference pattern, and thus the oscillations. However, this effect only occurs if the dispersion relation is not changed uniformly for all states, since this would just give rise to an overall phase in the transition amplitude, which is not observable in the oscillation probability. This condition is fulfilled for many situations of experimental interest, for instance in the common case when the background consists of atoms. While the interaction with the nucleons is the same for all flavor states, the interaction with the electrons in the atoms is different for electron neutrinos and neutrinos of different flavors. In fact, the case of an electron neutrino scattering off a background of electrons has been calculated in detail above,[5] with the respective Feynman diagrams depicted in fig. 2.1. For a neutrino of different flavor, the interaction shown in fig. 2.1 (a) is suppressed due to lepton family number conservation. Therefore the only contribution to V_{eff} relevant to oscillations at FTD in ordinary matter is due to the CC interaction depicted in fig. 2.1 (a), given by

$$V^e_{\text{eff}} = -b = \sqrt{2}G_F N_e. \tag{2.57}$$

---

[4] If CP violation is not maximal, as it can be the case for Beyond Standard Model (BSM) scenarios, similar terms proportional to P_R need to be added.

[5] The calculation was done assuming a free Fermi gas for the electrons, which is only an approximation for electrons bound in matter.

Neglecting again the subtleties discussed in section 2.3, the time-independent oscillation probability given in the first line of eq. (2.27) still holds, yet $|\mathbf{p}_{m_i}|$ is now given in the ultrarelativistic limit by

$$|\mathbf{p}_{m_i}| \simeq E^2 - \frac{m_i^2}{2E} - \tilde{V}^e_{\mathrm{eff},i}, \tag{2.58}$$

where $\tilde{V}^e_{\mathrm{eff},i}$ is the effective potential in the mass basis. Inserting now this relation into the first line of section 2.3 gives

$$\begin{aligned} P_{\alpha\beta}(L) &\simeq \left| \sum_i U^*_{\alpha i} U_{\beta i}\, e^{i(E^2 - \frac{m_i^2}{2E} - \tilde{V}^e_{\mathrm{eff},i})L} \right|^2 \\ &= \left| \exp\left[-iU(\mathrm{diag}\left(\frac{m_i^2}{2E}\right) + \tilde{V}^e_{\mathrm{eff}})U^\dagger L \right]_{\alpha,\beta} \right|^2 \\ &= \left| \exp\left[-i(U_{\mathrm{eff}}\,\mathrm{diag}\left(\frac{m^2_{\mathrm{eff},i}}{2E}\right) U^\dagger_{\mathrm{eff}})L \right]_{\alpha,\beta} \right|^2 \\ &= \sum_{i,k} U^*_{\mathrm{eff},\alpha i} U_{\mathrm{eff},\beta i} U_{\mathrm{eff},\alpha k} U^*_{\mathrm{eff},\beta k}\, \exp\left[\frac{-i\Delta m^2_{\mathrm{eff},ik} L}{2E} \right], \end{aligned} \tag{2.59}$$

where U_{eff}, $U^\dagger_{\mathrm{eff}}$ are the transformation matrices that diagonalize the matrix $U(\mathrm{diag}(m_i^2/2E) + \tilde{V}^e_{\mathrm{eff}})U^\dagger$ appearing in the second line, and $m^2_{\mathrm{eff},i}$ are its eigenvalues.

As discussed in section 2.3, it is often justified to work in a two-flavor approximation, where the two dimensional matrix $U^{2\nu}$ defined in eq. (2.36) can be used for U. In cases where such an approximation is legitimate, also the transformation matrices U_{eff} and $U^\dagger_{\mathrm{eff}}$ can be cast into this form by defining an effective mixing angle θ_{eff} at FTD as follows:

$$\sin^2 2\theta_{\mathrm{eff}} := \frac{\sin^2 2\theta_0}{\left(\cos 2\theta_0 + \frac{2E}{\Delta m^2} V_{\mathrm{eff}}\right)^2 + \sin^2 2\theta_0}, \tag{2.60}$$

where θ_0 is the corresponding two-flavor mixing angle in vacuum. Accordingly, the mixing matrix $U_{\mathrm{eff}} = (U^{2\nu\,\dagger}_{\mathrm{eff}})^T$ then reads

$$U^{2\nu}_{\mathrm{eff}} = \begin{pmatrix} \cos\theta_{\mathrm{eff}} & \sin\theta_{\mathrm{eff}} \\ -\sin\theta_{\mathrm{eff}} & \cos\theta_{\mathrm{eff}} \end{pmatrix}. \tag{2.61}$$

The respective two-flavor probability at FTD can be readily inferred to be

$$\begin{aligned} P^{2\nu}_{\overset{(-)}{\alpha}\overset{(-)}{\alpha}} &= 1 - \sin^2(2\theta_{\mathrm{eff}}) \sin^2\left(\frac{\Delta m^2_{\mathrm{eff}} L}{4E}\right) \\ P^{2\nu}_{\overset{(-)}{\alpha}\overset{(-)}{\beta}} &= \sin^2(2\theta_{\mathrm{eff}}) \sin^2\left(\frac{\Delta m^2_{\mathrm{eff}} L}{4E}\right), \end{aligned} \tag{2.62}$$

where Δm^2_{eff} can be calculated to be

$$\Delta m^2_{\text{eff}} = 2E\sqrt{\left(\tfrac{\Delta m^2}{2E}\cos 2\theta_0 + V_{\text{eff}}\right)^2 + \left(\tfrac{\Delta m^2}{2E}\right)^2 \sin^2 2\theta_0}. \tag{2.63}$$

Equation (2.62) is again of the same form as the corresponding two-flavor limit in vacuum, which has been derived for $\alpha, \beta = \mu, \tau$ in eq. (2.35). However, unlike in the vacuum case, where the amplitude of the oscillation, $\sin^2(2\theta_0)$, is solely dependent on the entries of the PMNS matrix and thus determined by nature, the amplitude in eq. (2.62) in addition depends via eq. (2.60) on V_{eff} and the energy E of the neutrino. Since V_{eff} is in turn determined by the physical properties of the background and E is determined by the neutrino source, the oscillation amplitude at FTD can in principal be explored experimentally. In particular, eq. (2.60) states that however small, yet non zero, the vacuum mixing angle θ_0 might be, if the *resonance condition*

$$\cos 2\theta_0 = -\tfrac{2E}{\Delta m^2} V_{\text{eff}} \tag{2.64}$$

holds, the amplitude of the mixing probability will always be maximal. Since neutrinos emitted by some source often follow a distribution, it is very likely that some of them will hit the resonance condition eq. (2.64) if the spectrum lies in the right range. Conversely, V_{eff} depends on the properties of the background, like the temperature or the electron number density for example in the case of the effective potential given in eq. (2.57). But it is usually not possible to prepare the background at scales necessary for oscillation experiments on earth. However, in astrophysical environments, different backgrounds are naturally provided. A special case is the sun, which produces electron neutrinos. It offers a special environment with very high pressure in the center slowly decreasing towards its outside. A neutrino produced at the center of the sun can be described as a state in the effective mass basis, which is the basis in which the Hamiltonian including V_{eff} at this point is diagonal. Thus an electron neutrino is given by

$$|\nu_e\rangle = \sum_i U^*_{\text{eff},ei}\, |\mathbf{p}_{m_{\text{eff},i}}\rangle, \tag{2.65}$$

where in the two-flavor approximation, U^*_{eff} is given by the transpose of eq. (2.61). At the center of the sun, V_{eff} is large, and hence $\cos^2 2\theta_{\text{eff}}$ approaches one, while $\sin^2 2\theta_{\text{eff}}$ can be neglected. Thus, at the center of the sun, the effective mass basis and the flavor basis can considered to be aligned, and the electron state coincides with one of the effective mass eigenstates. But if V_{eff} changes *adiabatically*, the initial eigenstate will stay an eigenstate of the Hamiltonian up to small corrections proportional to the rate of change of the effective mixing angle defined in eq. (2.61). However, its flavor composition slowly changes because θ_{eff} evolves into θ_0. In the center of the sun, $|(V_{\text{eff}}2E)/\Delta m^2|$ is much larger than $1 \geq \cos 2\theta_0$, while outside the sun, $|(V_{\text{eff}}2E)/\Delta m^2|$ is zero. Therefore, for V_{eff} varying continuously, the resonance condition eq. (2.64) is met if $\Delta m^2 > 0$ somewhere along the trajectory of a neutrino from the center to the outside of the sun. In that case, the validity of the adiabatic approximation depends on the size of the region where the resonance condition is fulfilled compared to the oscillation length, and thus the neutrino energy. Measurements of energy spectra of solar neutrinos demonstrated that adiabatic as well as non-adiabatic flavor conversions occur in the sun. These are well in agreement with theory beyond the adiabatic approximation and reveal that solar neutrinos indeed meet the resonance condition eq. (2.64) while propagating through the sun, and hence the sign of $\Delta m^2 > 0$ could be determined, as was mentioned in section 2.3 [7].

The various implications of a thermal background on neutrino mixing discussed in the above section commonly go under the name Mikheyev-Smirnov-Wolfenstein (MSW) effect [23, 24].

2.5 Experimental evidence for neutrino oscillations

Having set up the stage by recapitulating the phenomenology of the SM neutrino oscillations, it is now time to confront these predictions with the reality in the form of data taken in numerous experiments around the globe. Since the first compelling evidences for neutrino oscillations from the measurements of solar and atmospheric neutrino fluxes, numerous experiments probing the SM oscillation hypothesis have been conducted. These experiments have measured for neutrinos from as different sources as reactors, the atmosphere, the sun as well as beams produced in laboratories. The initial neutrino species in the different types of experiments have either been particles or antiparticles of electron or muon flavor. Neutrinos of all three flavors have been registered. Between the experiments, the length of the baseline from the source to the detector ranges from $\mathcal{O}(100\,m)$ to the distance between the earth and the sun, and the energy of the neutrino ranges from $\mathcal{O}(1\,MeV)$ to $\mathcal{O}(100\,GeV)$. Lastly, neutrinos which have propagated through vacuum as well as matter have been studied [25]. The crucial question obviously is if all these experimental data match the oscillation formulas eq. (2.27) and eq. (2.29), and if all results can be fitted with the same values for the PMNS matrix. The Review of Particle Physics, which features a comprehensive review of the experimental data in particle physics, states on that matter:

> "With the exception of a few possible anomalies such as LSND, current neutrino data can be described within the framework of a 3×3 mixing matrix between the flavor eigenstates ν_e, ν_μ, and ν_μ and the mass eigenstates ν_1, ν_2, and ν_3." [7]

It seems therefore justified to conclude that the standard oscillation picture discussed in this chapter indeed exhibits a valid model. However, there are few experiments reporting data that cannot be fitted satisfyingly with the parameters preferred by the majority of experiments. Even more intriguing, these *anomalies* occur in experiments using different channels, techniques and baselines. Therefore a common explanation of these anomalies, which is independent of the experimental systematics of the respective experiments, seems to suggest itself. In this regards, an interesting idea is the extension of the three-flavor oscillation model to a $3 + 1$ model, which incorporates a fourth, light, "sterile" state. This theory will be explored extensively in chapter 4.

3 Brief introduction to the early universe

3.1 Thermal history of the early universe

Following up on the summary of the characteristic properties of neutrinos given in the last chapter, the current chapter discusses how particles with these properties impact the evolution of the universe. In this regard, sections 3.2.2 to 3.2.4 explain how various cosmological probes require very specific values for several characteristic properties of neutrinos or other neutrino-like particles that were present throughout the thermal history of the universe. To illustrate how these constraints come about, the following section provides a short review of the standard picture of the evolution of the early universe.

The universe at large scales is dominated by gravity. At these scales, gravity is described by general relativity (GR). In this theory, Einstein's equations, given by [26]

$$\mathcal{R}_{\mu\nu} - \frac{1}{2}\mathcal{R}\, g_{\mu\nu} = 8\pi G_{\mathrm{N}} T_{\mu\nu} + \Lambda g_{\mu\nu}, \tag{3.1}$$

with G_{N} Newton's gravitational constant, express the fundamental relations between matter, energy and space-time. In detail, in eq. (3.1) $g_{\mu\nu}$ denotes the metric tensor associated with space-time. The terms $\mathcal{R}_{\mu\nu}$ and $\mathcal{R}$ refer to geometrical measures which quantify how much an arbitrary Riemannian manifold differs from flat Euclidean space [27]. $T_{\mu\nu}$ represents the energy-momentum tensor, which measures the flux of the μth component of the four-momentum through a surface of fixed ν-coordinate. Hence for example T_{00} corresponds to the energy density of the respective object described by $T_{\mu\nu}$ whereas the diagonal entries T_{ii} correspond to the pressure on the surface perpendicular to x_i . Finally Λ is a constant called cosmological constant. $\Lambda g_{\mu\nu}$ can be interpreted as a second energy-momentum tensor. Since the case of $T_{\mu\nu} = 0$ corresponds to vacuum, $\Lambda g_{\mu\nu}$ has then to be taken as the energy-momentum tensor associated with the vacuum.

Despite the beautifully simple form of eq. (3.1), Einstein's equations are only solvable in special cases. The universe with its vast amount of matter clustered in complex structures does not appear to be predisposed for being solvable. However, to good approximation, the universe in fact is such a special case, due to the cosmological principal. This principal expresses the notable experimental observation that at large scales, the universe is homogeneous and isotropic. This implies that the metric tensor $g_{\mu\nu}$ has to equal the diagonal Robertson-Walker metric

$$g_{\mu\nu} = \mathrm{diag}\left(1, \frac{-a(t)}{1-kr^2}, -a(t)r^2, -a(t)\sin^2\theta\right), \tag{3.2}$$

where $k \in \{-1, 0, 1\}$ is the curvature constant, which determines the geometry of 3-dimensional space to be either closed, open or spatially flat. The factor $a(t)$ represents the scale factor of the universe. Imposing also isotropy and homogeneity on the energy-momentum tensor $T_{\mu\nu}$ leads to significant simplifications: all off-diagonal entries have to vanish to leave $T_{\mu\nu}$ invariant in a rotated reference frame. Furthermore, the energy density ρ and the pressure p cannot depend on the spacial coordinate. This particular form of $T_{\mu\nu}$ corresponds to a perfect fluid[1], which is a fluid characterized by vanishing viscous shear and vanishing heat flux. In the rest frame of the perfect fluid the energy-momentum then reads [26]

$$T_{\mu\nu} = -pg_{\mu\nu} + (p+\rho)g_{00}. \tag{3.3}$$

with $g_{\mu\nu}$ the Robertson-Walker metric defined in eq. (3.2). There are two noteworthy special cases: [26]

$$p = 0 \qquad \text{dust} \tag{3.4}$$

$$p = \frac{1}{3}\rho \qquad \text{radiation} \tag{3.5}$$

The special case of zero pressure, eq. (3.4) is called *dust*. It corresponds to an ideal gas in the limit of low velocities and is thus a good approximation for non-relativistic matter. Since $\rho = 3p$ is the equation of state for a relativistic gas, the corresponding energy-momentum tensor using the relation eq. (3.5) is a good approximation for *radiation*. In general, the universe contains both, dust and radiation. However, it turns out that to good approximation at each moment of time one particular component dominates.

The perfect fluid form of $T_{\mu\nu}$ can be considered as a global picture of the dynamical degrees of freedom (DOFs), which applies to the universe on average. Locally, there are small deviations in $T_{\mu\nu}$ probably initiated at very early times in the universe. Therefore, the dynamical DOFs of the universe are usually modeled as a background described as perfect fluid with small, local perturbations $\delta T_{\mu\nu}$ to the energy-momentum tensor. These can be differentiated into perturbations

---

[1] Strictly speaking, a collisionless set of particles, as for example cold dark matter or neutrinos after decoupling, do not constitute a fluid, however formally, the fluid form of $T_{\mu\nu}$ can still be used to model these “collisionless fluids” [28].

that preserve the perfect fluid form of $T_{\mu\nu}$ and perturbations that do not preserve it, which are called *anisotropic stress* [29]. Since anisotropic stress involves p, only relativistic particles can contribute to it. However, it turns out that for strongly coupled particles the effect is negligible, because in this case variations in the distribution function are small on length scales comparable with the mean free path [30]. By contrary for free-streaming relativistic particles $T_{\mu\nu}$ receives local contributions of anisotropic stress. This applies in particular to neutrinos, which decouple quite early and consequently become free-streaming while the universe is still radiation dominated.

Inserting the perfect fluid energy-momentum tensor for the background, eq. (3.3), and the Robertson-Walker metric eq. (3.2) in Einstein's equations eq. (3.1) results in the Friedmann equations [26]

$$H^2 := \left(\frac{\dot{a}}{a}\right)^2 = \frac{8\pi G_{\mathrm{N}}\rho}{3} - \frac{k}{a^2} + \frac{\Lambda}{3} \tag{3.6}$$

$$\frac{\ddot{a}}{a} = \frac{\Lambda}{3} - \frac{4\pi G}{3}\left(\rho + 3p\right), \tag{3.7}$$

where the variable H defined in eq. (3.6) is called the Hubble parameter. In addition, accounting for local energy conservation, gives a third equation

$$\dot{\rho} = -3H(\rho + p). \tag{3.8}$$

Up to this point, all considerations solely relied on the cosmological principal. From now on, the discussion is restricted to the ΛCDM framework, which is the standard model of cosmology. This model combines GR including a small but non-zero cosmological constant Λ with the particle content from the Standard Model of particle physics. In addition, one particle species beyond SM is required, which is collisionless and cold. This new particle is called cold dark matter (CDM). It is of minor importance for this thesis, and hence not discussed in detail here. In the ΛCDM framework, assuming sharp transitions from relativistic to nonrelativistic velocities, essentially all particles can be assumed to be either dust or radiation, as defined in eqs. (3.4) and (3.5). In addition, $\Lambda g_{\mu\nu}$ corresponds to a fluid with $p = -\rho$. This follows from interpreting $\Lambda g_{\mu\nu}$ again as the energy-momentum tensor for the vacuum. The equation of state $p = -\rho$ then derives from comparing the terms proportional to Λ with the corresponding terms originating from $T_{\mu\nu}$ in eqs. (3.6) and (3.7).

The Hubble parameter was measured to be positive. This implies that the universe is expanding, because the scale factor increases. But from eq. (3.7) follows, using the experimental fact that Λ is small[2], that the change in the

---

[2] This holds only in the early universe. Since the energy density of matter and radiation constantly decreases due to the expansion of the universe, Λ, which is constant, will eventually be larger than the term proportional to $(\rho + p)$ in eq. (3.6).

expansion rate constantly decreases. In turn this means that the expansion rate has always been positive and the universe has always been expanding. Reversing this argument the only logical solution then is that the universe earlier on was very small and due to the laws of thermodynamics much denser and hotter than it is today. In particular, there seems to have been a singularity of space-time, usually called “the Big Bang” from which the expansion started.

Almost the complete history of the universe since the Big Bang can be described quite accurately by the Friedmann equations eqs. (3.6) and (3.7) and the laws of thermodynamics as demonstrated in the following very brief review. The Friedmann equations encode the evolution of the universe in terms of the energy density ρ. The energy density for a single particle species i can in turn be calculated according to

$$\rho = \frac{g}{(2\pi)^3} \int d^3p \, E(\mathbf{p}) n^{\pm}_{f/b}(p) \tag{3.9}$$

where g is the number of internal DOFs for this particle, and $n^{\pm}_{f/b}(p)$ are the distribution functions defined in eq. (2.37). In the ultrarelativistic limit, eq. (3.9) can be evaluated to [26]

$$\rho_i \simeq \begin{cases} \frac{7}{8}\frac{\pi^2}{30} g T^4 & \text{fermions} \\ \\ \frac{\pi^2}{30} g T^4 & \text{bosons} \end{cases} . \tag{3.10}$$

On the other hand, in the nonrelativistic limit, ρ is expressed by [26]

$$\rho_i \simeq g \left(\frac{m_i T}{2\pi}\right)^{3/2} e^{-(m_i-\mu)/T} \left(m_i + \frac{3T}{2}\right), \tag{3.11}$$

with μ the chemical potential and m_i the mass of the particle. The total energy density is just the sum of the individual ρ_i, that is $\rho = \sum_i \rho_i$.

Leaving aside the speculative first moments of the universe including possible inflation and the electroweak phase transition, the thermal history revised here starts at a very high temperatures $T \sim 100\,\mathrm{GeV}$ some picoseconds after the Big Bang. Due to the extreme hot and dense environment, all particle species are initially relativistic and in thermal equilibrium, and their respective energy densities are given by the expressions in eq. (3.10). At this epoch, the universe is *radiation dominated.* Hence, the approximation eq. (3.5) is legitimate and the total energy density is given by [26]

$$\begin{aligned} \rho = \sum_i \rho_i \simeq & \sum_j g^f_j \frac{7}{8}\frac{\pi^2}{30} T_j^4 + \sum_k g^b_k \frac{\pi^2}{30} T_k^4 \\ = & \frac{\pi^2}{30} g_*(T)\, T^4, \end{aligned} \tag{3.12}$$

with the *effective number of degrees of freedom*, $g_*(T)$, is defined by

$$g_*(T) := \sum_j g_j^b \left(\frac{T_j}{T}\right)^4 + 7/8 \sum_k g_k^f \left(\frac{T_k}{T}\right)^4 , \tag{3.13}$$

where the g_j^b and g_k^f are the numbers of internal DOFs for bosons and fermions, respectively, and the $T_{j/k}$ are the individual temperatures of the particles. As long as all particles are in thermal equilibrium, their respective temperatures are the same, $T_j = T_k = T$. Usually the photon temperature T_γ is taken as reference temperature T. Therefore, T denotes the photon temperature in what follows.

During radiation domination, using eq. (3.12), eq. (3.8) can be integrated to give the relation between the energy density and the expansion rate, [26]

$$\rho = \frac{\pi^2}{30} g_*(T)\, T^4 \propto a^{-4} \qquad \text{(radiation domination).} \tag{3.14}$$

Thus, according to this equation $T \propto a^{-1}$. This proofs that the universe cools down as it expands. During this process, its temperature gradually drops below the rest mass of the heavier particles. This implies that the respective particles become nonrelativistic and annihilate with the respective antiparticles. At the same time, these particles are no longer recreated efficiently by pair production from the vacuum. The energy due to potentially heavy particles remaining after the annihilation is negligible at high temperatures as can be seen from comparing eq. (3.10) and eq. (3.11). Consequently the total energy density is still given by eq. (3.12), whereas g_* reduces whenever T drops below the rest mass of a particle. This process continues with the slight complication of the quantum chromodynamics (QCD) phase-transition, during which hadrons form from previously free quarks and gluons. Finally, the only remaining relativistic particles are electrons, positrons, neutrinos and photons, which gives four internal fermion DOFs for the charged leptons, two internal fermion DOFs for each of the three SM neutrino species as well as two internal boson DOFs for the photon, and hence $g_* = 2 + 7/8 \times 4 + 7/8 \times 6 = 10.75$.

As the universe expands further, it becomes less and less likely that two particles meet. If this probability becomes too small for a specific particle, its reaction rate becomes virtually zero. However, interactions are necessary to establish thermal equilibrium. Consequently, a particle that does not interact with the bath of remaining particles drops out of thermal equilibrium. As a minimal condition for a particle i to be in thermal equilibrium it is usually required to react on average at least once during the history of the universe [26]. This condition is expressed by

$$\Gamma_i \sim n_i \langle \sigma v \rangle > H, \tag{3.15}$$

where Γ_i is the interaction rate, n_i is the number density and $\langle\sigma v\rangle$ is the thermally averaged cross section. For neutrinos, which only interact through the weak interaction with small cross section, the condition eq. (3.15) is no longer fulfilled around $T \sim 1\,\mathrm{MeV}$. Hence, neutrinos at this temperature cease to be in thermal equilibrium with the bath of particles and *decouple* or "freeze out". From this moment on, neutrinos essential stream freely, only their momentum p redshifts by the factor $a/a_{\text{freeze out}}$. Since only the ratio $p'/T_\nu = pa/(T_\nu a_{\text{freeze out}})$ appears in the distribution function defined in eq. (2.37), equivalently the temperature T_ν can be considered to scale with the inverse factor $a_{\text{freeze out}}/a$.

Soon after the decoupling of the neutrinos, the temperature drops below the rest mass of the electron and thus the electrons and positrons become nonrelativistic. The only remaining relativistic species in the SM are therefore photons and neutrinos. The subsequent annihilation of electrons and positrons into photons enhances the temperature of the photon bath. However, neutrinos are no longer in thermal contact with the photons and therefore the photon temperature T and the neutrino temperature T_ν differ after the annihilation of electrons and positrons. The ratio between the two temperatures can be calculated by imposing entropy conservation,

$$\mathrm{d}(sa^3) = 0, \tag{3.16}$$

where $s = S/V$ is the entropy density. This is justified because the increase in entropy in any single process is negligible compared to the total entropy of the universe [31]. The entropy density s_i due to a specific particle species, in the limit of vanishing chemical potential, is given by [31]

$$s_i = \frac{S_i}{V} = \frac{\rho_i + p_i}{T_i}. \tag{3.17}$$

Accordingly, the total entropy density for relativistic particles reads

$$s = \sum_i s_i = \frac{2\pi^2}{30} g_{*s} T^3, \tag{3.18}$$

where g_{*s} is by analogy to eq. (3.13) defined as [31]

$$g_{*s}(T) := \sum_j g_j^b \left(\frac{T_j}{T}\right)^3 + \frac{7}{8}\sum_k g_k^f \left(\frac{T_k}{T}\right)^3. \tag{3.19}$$

Applying entropy conservation to the total entropy density eq. (3.18) results in [31]

$$g_{*s}(T) T^3 a^3 = \text{const.} \tag{3.20}$$

On the other hand, as argued above, the neutrino temperature T_ν scales with a^{-1}, and hence also

$$T_\nu^3 a^3 = \text{const} \tag{3.21}$$

holds. Combining these relations results in [31]

$$g_{*s}(T)\left(\frac{T}{T_\nu}\right)^3 = \text{const}, \tag{3.22}$$

Before electrons and positrons become nonrelativistic, they contribute to g_{*s}, which hence amounts to

$$g_{*s} = g_* = 2 + 3.5 + 5.25 = 10.75 \qquad \text{(before } e^-\, e^+ \text{ annihilation)}. \tag{3.23}$$

After this process, inserting the photon and neutrino DOFs and T_ν into eq. (3.19) g_{*s} gives

$$g_{*s} = 2 + 5.35\left(\frac{T_\nu}{T}\right)^3 \qquad \text{(after } e^-\, e^+ \text{ annihilation)}. \tag{3.24}$$

Evaluating the condition eq. (3.22) for the situation at a temperature T_0 before neutrino decoupling and at a temperature T after electrons and positrons have annihilated finally results in

$$\begin{aligned} 10.75\left(\frac{T_0}{T_{0,\nu}}\right)^3 &= \left(2 + 5.35\left(\frac{T_\nu}{T}\right)^3\right)\left(\frac{T}{T_\nu}\right)^3 \\ \Rightarrow \frac{T_\nu}{T} &= \left(\frac{4}{11}\right)^{\frac{1}{3}}, \end{aligned} \tag{3.25}$$

using that before neutrino decoupling $T_0 = T_{0,\nu}$.

The evolution of the universe, its scale factor and expansion rate are correlated with the energy density, as expressed by the Friedmann equations eqs. (3.6) to (3.8). Hence, the result eq. (3.25) derived above is very important, because it allows to calculate g_* according to eq. (3.13), and consequently the important energy density in relativistic DOFs. Explicitly, using eq. (3.12), ρ can be estimated according to

$$\begin{aligned} \rho \simeq \frac{\pi^2}{30} g_*(T)\, T^4 &= \frac{\pi^2}{30}\left(2 + \frac{7}{8} \times 2 \times 3 \times \left(\frac{T_\nu}{T}\right)^4\right) T^4 \\ &= \frac{\pi^2}{30}\left(2 + \frac{7}{4} \times 3 \times \left(\frac{4}{11}\right)^{\frac{4}{3}}\right) T^4. \end{aligned} \tag{3.26}$$

The above equation does not hold exactly. This is on the one hand due to the relativistic approximation eq. (3.10), on the other hand the above derivation of the ratio T_ν/T relied on the assumption that neutrinos are completely decoupled at the time of the electron-position annihilation. However, since the neutrino momenta are distributed according to eq. (2.37), the decoupling condition eq. (3.15) is not met simultaneously by all neutrinos and a small fraction is still in thermal contact with the photon bath at the time of electron-position annihilation. Taking into account these effects as well as corrections due to flavor oscillations, the energy density can be calculated to higher accuracy. In that case, it is convenient to parametrize the energy density due to relativistic DOFs by analogy to eq. (3.26) as [31]

$$\rho := \frac{\pi^2}{30}\left(2 + \frac{7}{4} \times N_{\text{eff}} \times \left(\frac{4}{11}\right)^{\frac{4}{3}}\right) T^4, \tag{3.27}$$

where N_{eff} is the *effective number of relativistic species* beyond the well-established photons. N_{eff} is thus measured in units of the number of SM neutrino species in the limit of instantaneous decoupling [32]. It is currently calculated to [33]

$$N_{\text{eff}} = 3.045. \tag{3.28}$$

Any measurement of an excess of this number would hint at additional relativistic species in the early universe.

After the decoupling of the neutrinos and the annihilation of electrons and positrons, the universe expands and cools further. So far neutrons and protons are converting constantly in one another other, with an inter-conversion rate of $\Gamma_{p\leftrightarrow n} \sim G_{\mathrm{F}}^2 T^5$. Hence, neutrons and protons are in thermal equilibrium, with their respective number densities distributed according to the ratio $n/p = e^{-Q/T}$, with $Q = 1.293\,\mathrm{MeV}$ denoting the mass difference between neutrons and protons [34]. On the other hand, in the early universe, the Hubble parameter can be estimated from the first Friedmann equation eq. (3.6) to give

$$H^2 \simeq \frac{8\pi G_{\mathrm{N}}\rho}{3} \simeq \sqrt{g_* G_{\mathrm{N}}} T^2, \tag{3.29}$$

neglecting the small cosmological constant Λ and the term $ka^{-2} \ll \rho \propto a^{-4}$, which is legitimate for the small a in the early universe. Comparing eq. (3.29) to the inter-conversion rate $\Gamma_{p\leftrightarrow n}$, reveals that the equilibrium condition eq. (3.15) ceases to hold at some temperature [34]

$$T_{p/n} \sim (g_* G_{\mathrm{N}}/G_{\mathrm{F}}^4)^{\frac{1}{6}} \sim 1\,\mathrm{MeV}. \tag{3.30}$$

Thus, the ratio $n/p = e^{-Q/T_{p/n}}$ at this point is sensitive to g_* and hence N_{eff}. Since from the point when $T_{p/n}$ is reached neutrons and protons are no longer in equilibrium, neutrons decay and consequently the ratio $n/p = e^{-Q/T_{p/n}}$ reduces further. However, as the temperature of the universe continues to decrease, at some point it drops below the nuclear binding energy $\sim 0.1\,\mathrm{MeV}$. As a consequence, light nuclei form from the previously free protons and neutrons. This process is known by the name of *Big Bang nucleosynthesis (BBN)*. The ratio between the various light elements produced during BBN depends on the relative densities of protons and neutrons. These initial ratios are still correlated with the fractions of the respective light elements measured today. In particular, BBN is the only notable source of deuterium. Therefore, the deuterium abundance today is directly linked to the densities of protons and neutrons at the time of BBN [34].

As the temperature falls well beneath the ionization energy of hydrogen at about 300.000 years after the Big Bang, electrons and protons in the plasma *recombine* to hydrogen atoms. Since up to this point, the dominant interaction process for photons is Thompson scattering on free electrons, the interaction rate of photons is drastically reduced after recombination because virtually no more free electrons and protons are existent. Hence, photons from that moment on start streaming freely and light can spread for the first time. This also implies that all photons present at that moment essential travel without change of polarization and direction from the point of their last scattering during recombination up to date. Along the way their temperature changes according to $T \propto a^{-1}$ due to redshift in the same way as explained for neutrinos above, because the universe continues to expand. Consequently these photons today have wavelengths in the microwave range and are hence known by the name *cosmic microwave background (CMB)*. Neglecting secondary effects impacting the photons since decoupling, the CMB photons measured today arrive from a shell consisting of the points where the last scattering event before decoupling happened, called “last scattering surface”. In the limit of instantaneous decoupling, all the photons in the CMB were released at the same moment in time, hence by looking at these today, one sees a redshifted “snapshot” of the universe at the time of recombination.

The CMB measured today exhibits an almost perfect blackbody spectrum. Since each photon essentially points back to the last scattering event, this implies that the universe was extremely isotropic at the time of recombination. However, an expansion of the CMB power spectrum in spherical harmonics reveals small but very important features. In particular, traces of small fluctuations in the matter density can be observed. These are the seeds for the complex structures observed today, because overdense regions are the source of slightly stronger gravitational potentials which attract matter from slightly underdense regions. As a result initially overdense regions accredit more and more matter. For ordinary matter this process could only start after photon decoupling, because it was previously inhibited by radiation pressure. Before photon decoupling, the counteracting impulses of gravity and pressure induce oscillations in the plasma, which give rise to sound waves. The pattern of the sound waves of various modes translates to the CMB power spectrum, because areas of different densities in the plasma have slightly different temperatures. After decoupling, these variations result in peaks at certain values of the multipoles in the power spectrum of the CMB, known as *acoustic peaks.* These peaks correspond to maximally overdense or underdense regions in the plasma and hence accord with those modes of the plasma oscillation, which exhibit a maximum or minimum at the time of decoupling [35]. Sticking with the metaphor of a photograph, the “snapshot” of the universe at the time of recombination is “blurred” because of a long “exposure time” [31]. This is because the decoupling of the photons from the plasma did not happen instantaneously but in fact their coupling to the plasma first decreased, leading to an intermediate phase where photons would diffuse rather than freestream. This makes the “snapshot” “blurred”, since this diffusion phase washes out small scale structures and hence suppresses anisotropies at high multipoles. This effect is known as *Silk damping* [36].

Of course the history of the universe does not end after recombination and the release of the CMB. However, the details of the physical processes happening at later times are less important in the context of this work and therefore not included in this short review. Based on evolution of the early universe presented here, the next sections give a more detailed analysis of the specific role of neutrinos and more generally light, weakly-interacting species.

3.2 Cosmological probes sensitive to neutrino-like particles

3.2.1 Neutrinos and neutrino-like particles

The short review in the previous section revealed in particular the crucial impact of relativistic species on the evolution of the early universe. For most of this epoch, neutrinos and photons are the only relativistic species in the ΛCDM framework. In particular, neutrinos constitute 40% of the total energy density during radiation domination [37]. Neutrinos in addition decouple early on, therefore, besides being a dominant ingredient they are also a very peculiar case, as their evolution is significantly different from other particles. Therefore, it does hardly come as a surprise that various cosmological probes proved very efficient in constraining neutrino parameters. The set of parameters cosmology is sensitive to is, however, different to that measured in direct neutrino detection experiments. This is because cosmology is dominated by gravity, whereas gravity is negligible in earthbound neutrino experiments. In particular, cosmological probes are not very sensitive to SM neutrino oscillations and they are less sensitive to cross sections. By contrary, as discussed in the following sections, very stringent bounds on the sum of neutrino masses and the number of neutrinos can be derived from various cosmological probes, assuming the ΛCDM framework. Therefore, the results from earthbound neutrino experiments and cosmology are vastly complementary.

It is, however, very important to note that the constraints from cosmology are based on the underlying model. In particular, going beyond the ΛCDM model adopted so far, it is not straightforwardly provided that the two sets of constraints actually apply to the same particles. For instance, it would in principal be conceivable that neutrinos were not produced in the early universe for some unknown reason or decayed, which would imply that the bounds from cosmology would not apply to neutrinos measured for example in oscillation experiments [32]. However, there are three characteristic parameters that can be probed independently using cosmological observables, as will be discussed in the following sections: the value N_{eff}, the existence of a free-streaming species during recoupling and the smallness of the corresponding mass-parameter. The combination of the results on each of these characteristic parameters from various cosmological probes confine the most likely interpretation to *neutrino-like* particles [32]. These particles share some fundamental features with the SM neutrinos. In detail, these features comprise a very low mass, such that the particles are relativistic at least during radiation domination. Furthermore the coupling to other species has to be small enough, such that the particles decouple very early on and become free-streaming, but strong enough such that they were in thermal equilibrium initially. To keep agnostic about the nature of the particles probed by cosmological observables as well as to stay as general as possible, the following analysis refers to neutrino-like particles, defined by the features described above.

3.2.2 Constraints based on N_{eff}

This section discusses constraints on N_{eff}, defined in eq. (3.27). As explained above, this number is a measure for the number of relativistic species except photons during radiation domination. According to the ΛCDM model, this number is associated with the number of SM neutrino species and expected to be 3.045. Different cosmological probes are sensitive to this value and can hence provide constraints, as reviewed in what follows.

The first bound is established by the CMB. As stated in eq. (3.29), the Hubble rate is directly related to g_* and hence N_{eff}. The main effect of increasing (decreasing) H on the CMB power spectrum is due to an increase (decrease) of the Silk damping scale. In principal, varying N_{eff} has further and more drastic effects on the CMB spectrum, but these are degenerate with the impact of varying other parameters. Thus, to avoid these drastic effects on the CMB spectrum, which would be strongly disfavored, the degenerate parameters can be varied simultaneously. This applies for example for the density of dark matter: to compensate for the effect of N_{eff} on the CMB spectrum, a higher dark matter density has to be assumed. However, an increased dark matter density impacts structure formation, which induces secondary effects on the CMB spectrum through weak lensing [32]. The current bound from the Planck measurement of the CMB, including weak lensing effects, is [3]$N_{\mathrm{eff}} = 3.11^{+0.44}_{-0.43}$, in agreement with the ΛCDM expectation [38].

The second constraint derives from BBN. As discussed previously, the relative abundance of light elements measured today is still correlated with the relative abundance of these elements produced during BBN. However, this relative abundance depends on the temperature at which the inter-conversion ceased being efficient. This temperature $T_{p/n}$ was estimated above according to eq. (3.30), which depends explicitly on g_* and hence N_{eff} [34]. Adding results from the measurements of the primordial light element abundances to the result from CMB measurements quoted above reduces the error by up to 30% compared to the value quoted above, to give [4]$N_{\mathrm{eff}} = 3.06^{+0.26}_{-0.28}$ [38].

The correlation between N_{eff} and the dark matter density imposed by the CMB spectrum finally gives rise to a third constraint which is due to the angular matter power spectrum. This spectrum is a power spectrum of the matter density in universe as a function of scale. It provides a measure of how matter structures formed from initial perturbations. Before photon decoupling, dark matter and baryonic matter behave differently, and hence their impact on the early structure formation is different: baryons exhibit acoustic oscillations as described previously, while dark matter falls unimpededly into gravitational wells and starts building up structure earlier on. Therefore, increasing the dark matter density as required due to the degeneracy with N_{eff}, while leaving the density of baryonic matter fixed, changes the matter power spectrum. However, constraints derived from the analysis of large scale matter structure are not very restrictive and hence combining these data with the datasets discussed above has little impact [32].

In conclusion, the different cosmological observables reviewed above favor ranges of N_{eff} in precise agreement with the expectation from the ΛCDM model for the SM neutrinos. This result makes the existence of an additional neutrino-like particle very unlikely.

---

[3] This number includes additional information measured in galaxy redshift surveys to break some of the degeneracies between parameters constrained by the CMB.

[4] This number includes in addition to the results on light element abundances also information obtained from the polarization of the CMB.

3.2.3 Constraints based on free-streaming

So far the analysis only required the neutrino-like particles to be relativistic until recombination. However, as mentioned above, neutrinos are furthermore a special case, because they decouple early on and subsequently become free-streaming. As discussed above, this implies that the corresponding energy-momentum tensor locally receives contributions of anisotropic stress. This is a distinct feature, which is not shared by other relativistic but interacting species, like photons. It implies that unlike in the case of a perfect fluid, perturbations in the neutrino density are damped inversely proportional to time. Furthermore, since neutrinos move at the speed of light by the time of decoupling, perturbations in the neutrino density propagate much further than perturbations in the plasma, which are transferred through acoustic oscillations moving at the speed of sound. Lastly, adding anisotropic stress to the energy-momentum tensor as a source of gravity quite generally leads to a richer structure of metric perturbations compared to the energy-momentum tensor corresponding to a perfect fluid. All three phenomena have via gravitational interaction a small but measurable effect also on the other particles [37], which can in particular be observed in the CMB spectrum. Measurements by Planck [39] indeed find for the parameter c^2_{vis}, which quantifies anisotropic stress, a value of 0.327 ± 0.037. This value is well in agreement with the prediction of $1/3$ for SM neutrinos in the ΛCDM model. In the case of interacting neutrino-like particles the value of is expected to be zero, $c^2_{\text{vis}} = 0$.

3.2.4 Constraints based on the sum of masses

SM neutrinos are furthermore required to have a small mass due to highly significant evidence for non-zero mass-squared differences from oscillation experiments, as reported in chapter 2. The effect of a non-zero mass can also be constrained by cosmological probes as summarized in this section.

For neutrino-like, and hence free-streaming particles, probes on large scale structure (LSS) formation provide strong constraints on the mass. This is because these particles virtually do not see potential wells smaller than their free-streaming scale, which roughly corresponds to the distance traveled during a Hubble time scale $t_H = (a/\dot{a})$. Therefore, they do not contribute to potential wells smaller than this scale. Hence, LSSs at scales smaller than the free-streaming length lack the contribution due to massive neutrino-like particles. The heavier the neutrino-like particle is compared to the total matter structure, the larger the deficit. On the other hand, free-streaming particles fall into wells larger than their free-streaming length. However, their contribution to these large structures is very small. A second effect is due to the impact massive, free-streaming particles have on the balance between the gravitational forces driving structure formation and the expansion parametrized by H. This is because massive neutrino-like particles contribute to the total background density which determines H in terms of eq. (3.6), but they do not contribute to density fluctuations, because they are free-streaming. In combination, these effects result in a suppression of small structures below the free-streaming length, which are imprinted in the angular matter power spectra measured today [32].

However, this transformation of the matter power spectrum would impact other parameters which would result in drastic modifications of the CMB spectrum. By the same line of argument employed in section 3.2.2, these unreasonable effects on the well-measured CMB spectrum can be avoided by varying simultaneously degenerate parameters. The corresponding parameter in this case is the Hubble rate H. Varying H suppresses, however, the structures at high scales. Therefore, the effect of a combined analysis of the mass of the neutrino-like particle and H is an almost uniform suppression of LSSs at all scales [32].

Neutrino-like particles also contribute to the late background evolution, because due to its mass it eventually becomes nonrelativistic at late times in the history of the universe. Therefore, the CMB spectrum itself is also sensitive to the mass of the neutrino-like particle due to the late integrated Sachs-Wolfe (ISW) effect. This effect is caused by changes in the gravitational potential along the line of travel of a CMB photon. On the one hand, photons experience an effective change of frequency when traversing a potential well which changes meanwhile. This is because the initial blueshift from falling in is not compensated by the redshift from climbing out. On the other hand, when a potential perturbation decays, the space-time smoothens and hence a photon moving in the space-time suffers a blueshift [40].

Lastly, the suppression of structures generate weak lensing effects, which impact the measurement of the CMB spectrum. In particular the reduction of structures at large scales caused by varying H in combination with the mass of the neutrino-like particle decreases weak lensing effects on the CMB spectrum [32].

So far, the discussion neglected the case of multiple neutrino-like particles each having a different mass. In principal different masses would imply different free-streaming scales for each of the neutrino-like particles. However, for small differences in the masses, this effect is small. The other effects leaving imprints on cosmological probes only depend on the total mass of all neutrino-like particles, which is comprehensible from the discussion above. Therefore, cosmological probes in the main provide an upper bound to the total mass of neutrino-like particles with little sensitivity to the individual masses.

The latest Planck results constrain the sum of neutrino-like particles to [5] $\sum m_\nu <$

---

[5] c.f. footnote 3.

0.13 eV[38]. This is compatible with bounds coming from measuring the matter power spectrum, which are, however, much more difficult to interpret [38].

If the three SM neutrinos were indeed the only neutrino-like particles in the early universe, their minimum masses would be constrained by the mass-squared differences measured in oscillation experiments. Assuming that the lowest mass eigenstate was exactly zero, the two massive mass eigenstate would be $\sqrt{2.56 \times 10^{-3}\,\mathrm{eV}^2} \approx 0.051\,\mathrm{eV}$ and $\sqrt{3.73 \times 10^{-5}\,\mathrm{eV}^2} \approx 0.009\,\mathrm{eV}$, using the best-fit values for the mass-squared differences given in table 2.1. In NH, the sum of the neutrino masses would hence be $\sum m_\nu \approx 0.06\,\mathrm{eV}$, whereas in IH it would be $\sum m_\nu \approx 0.1\,\mathrm{eV}$. Thus, current cosmological data are once again in agreement with the prediction from the ΛDCM model. By contrary, the parameter space for an additional neutrino-like particle is very narrow, in particular assuming IH.

4 Analysis of neutrino oscillations in a $3+1$ framework

4.1 Introduction of the $3+1$ framework: motivation and theoretical background

From the discussion in chapter 2, the three-flavor oscillation paradigm emerges as a largely consistent framework, in which most of current data can be interpreted compellingly. On the other hand, a number of apparently *independent* anomalies continue to impugn this paradigm. A desirable goal is therefore to find a new model that excels the three-flavor model by matching also the datasets which seem anomalous in the standard approach, while still fitting equally well the majority of data which seem to be in agreement with the three-flavor model. One model that has been tipped for quite a while as promising candidate is the $3+1$ model, c.f. for instance [41]. This model is a rather straightforward generalization of the three-flavor oscillation model, where in addition to the three SM neutrinos a fourth neutrino takes part in the oscillations. The idea is then that the $3+1$ framework is required to fit all the data including the anomalies, just like the two-flavor limit fits a subset of the data well, but to fit all the data – excepting the anomalies – the three-flavor framework is required.

However, the number of neutrinos subject to the weak interaction and lighter than the Z boson has been determined in the SLC and LEP experiments to be three. Hence, the fourth, light neutrino has to be a singlet under the weak interaction, thus the name "3 + 1", referring to the three SM model plus the fourth singlet – or "sterile" – neutrino. But as has been discussed in section 2.2, supplementing the SM Lagrangian by a term for the neutrino mass by analogy to the other fermions necessarily calls for at least one "sterile" right-handed field. The charge-conjugated sterile left-handed field naturally mixes with the active neutrinos. As has been argued in section 2.2, the mass scale for such sterile neutrinos is not related to the mass scale of the other fields in the SM. There are no definite theoretical arguments requiring sterile neutrinos to be of small masses around $\mathcal{O}(1\,\mathrm{eV})$. In particular, the seesaw-mechanism would favor the sterile fields to be heavy. However, there is no fundamental obstacle that prevents the SM from containing a sterile neutrino that is light enough such that a flavor eigenstate produced in some neutrino source is a coherent superposition of four mass eigenstates.

While it is reassuring to note that the implementation of sterile neutrinos could be achieved straightforwardly, the exact theoretical model is not required to study the phenomenology of neutrino oscillations in the $3+1$ framework. In particular, as has been noted in section 2.3, possible Majorana phases do not alter the phenomenology of oscillations. Therefore, the only additional parameters needed to describe oscillations in the $3+1$ framework are the third mass-squared difference Δm_{41} and the parameters describing the mixing between the sterile state and mass eigenstates. The leptonic mixing matrix in the $3+1$ framework is of dimension 4×4. Including the new entries, it can be parametrized by

$$U^{3+1} \;=\; O_{34}(\theta_{34})\, V_{24}(\theta_{24}, \delta_{24})\, O_{14}(\theta_{14})\, O_{23}(\theta_{23})\, V_{13}(\theta_{13}, \delta_{13})\, V_{12}(\theta_{12}, \delta_{12}), \tag{4.1}$$

where, as in eq. (2.6), $O_{ij}(\theta_{ij})$ denotes a real rotation matrix corresponding to a rotation in the (ij)-plane parametrized by the rotation angle θ_{ij}, and V_{ij} denotes a complex rotation matrix parametrized by the angle θ_{ij} and a phase δ_{ij}. This parametrization of the mixing matrix will be used without further notification whenever it is explicitly needed in what follows. Because the derivation of the vacuum oscillation formulas eqs. (2.27), (2.29) and (2.31) given in section 2.3 never relies on the number of neutrino states, but only on the fact that a mass eigenstate can be written as a coherent superposition of flavor eigenstates, the corresponding oscillation probabilities in the $3+1$ framework are readily obtained by inserting the respective elements of the mixing matrix eq. (4.1) into the standard oscillation formulas eqs. (2.27), (2.29) and (2.31).

Since the mixing matrix in eq. (4.1) features two additional phases and three additional angles, one might expect a clear improvement of the fit to global oscillation data. This should be especially true for a subset of experiments, whose parameters allow for the SBL approximation, which holds for $\Delta m^2_{ij} L/4E \ll 1$ and $\Delta m^2_{4i} \approx \Delta m^2_{41}$, with $i, j \in \{1, 2, 3\}$, $j < i$. Using this approximation, the oscillation probability depends only on the column $U^{3+1}_{\alpha 4}$, thus not on the well-measured entries of $U^{3\times 3}$:

$$\begin{aligned} P^{\text{SBL}}_{\overset{(-)}{\alpha}\overset{(-)}{\alpha}} &= 1 - 4|U_{\alpha 4}|^2 (1 - |U_{\alpha 4}|^2) \sin^2\left(\frac{\Delta m^2_{41} L}{4E}\right) \\ P^{\text{SBL}}_{\overset{(-)}{\alpha}\overset{(-)}{\beta}} &= 4|U_{\alpha 4}|^2 |U_{\beta 4}|^2 \sin^2\left(\frac{\Delta m^2_{41} L}{4E}\right) \qquad (\alpha \neq \beta). \end{aligned} \tag{4.2}$$

However, it is extremely challenging to fit the data reasonably well, even when restricting the dataset solely to the subset of experiments which the above SBL approximation applies to. The reason for that is that the SBL approximation is legitimate to experiments that call for rather pronounced mixing with the fourth mass eigenstate, as well as to experiments which exclude such a strong mixing. The picture becomes more complicated when considering the full dataset and going beyond the SBL approximation in eq. (4.2). For instance at long baseline (LBL), oscillations involving the mass-squared differences Δm^2_{4i} average out, resulting in a constant, overall reduction of the flux, which in some experiments is degenerate with uncertainties. Furthermore, at least two effects beyond the pure oscillation phenomenology constrain the $3+1$ scenario. The first is that for certain parameters, a MSW resonance should be detectable for neutrinos propagating through matter. The second is that the oscillation probability should not depend on the neutrino source. On the other hand, within certain individual channels, the "$\overset{(-)}{\nu}_e \to \overset{(-)}{\nu}_e$" or "$\overset{(-)}{\nu}_e$ disappearance" channel, the "$\overset{(-)}{\nu}_\mu \to \overset{(-)}{\nu}_\mu$" or "$\overset{(-)}{\nu}_\mu$ disappearance" channel and the "$\overset{(-)}{\nu}_\mu \to \overset{(-)}{\nu}_e$" or "$\overset{(-)}{\nu}_e$ appearance" channel, rather consistent fits are possible using the $3+1$ framework.

Due to this entanglement of inconsistent evidences it is necessary to evaluate all the available data carefully to allow for conclusions about the potential of the $3+1$ framework. In the following sections, such an evaluation of the global data is performed by reviewing the global fits in the individual channels as well as of all channels combined, based on the references [2] and [3]. The implementations of the analyses of the individual experimental results are in large part based on adaptions of `GLoBES` [42, 43]. `GLoBES` is a publicly available software package designed for the simulation of long baseline neutrino oscillation experiments. Details on the implementations of the respective analyses can be found in different publications, quoted in the captions of the tables 4.2, 4.4 and 4.5, which enlist the corresponding experiments. The analysis in the $3+1$ framework is preceded by a short review of the parameter goodness of fit (PG) test, a statistical measure specifically designed to quantify the amount of tension between subsets of the total dataset. This measure will prove essential in disentangling the various evidences from the different channels.

4.2 Interlude: parameter goodness of fit

The original motivation for the introduction of the PG method as a statistical test actually arose in the context of the analysis of neutrino data in the context of $3+1$ models. Therefore it is not surprising that the PG test continues up to date being an important statistical tool to this effect, albeit its practicality is not restricted to this specific application [44].

The PG test is potentially superior to classic statistical tests, most notably the widely used GOF test, in the context of global fits, when a large dataset comprising the data measured by various experiments is fitted with many parameters. The well-known cause for the weak performance of the GOF test can be inferred from the following typical scenario: within a global fit, usually any of the investigated parameters is only constrained by a small subset of the complete dataset. Conversely, the remaining fraction of the data points is not sensitive to this particular parameter, therefore these can be fitted rather well, regardless of the concrete value of that parameter. If this part of the dataset is large, possible stringent constrains from the small fraction of data points actually sensitive to the parameter in question can get "washed out" completely. On the other hand, as the authors of [44] argue, the PG is based on parameter estimation and consequently the problem of possible constraints on a parameter from a small subset of data being "diluted" by the overwhelming majority of many insensitive data points is evaded.

The PG test provides a statistical measure that allows to test for the *compatibility* of different datasets within the framework of a given theoretical model. This is achieved by dividing the total dataset in two statistically independent subsets A and B. A test statistic χ^2_{PG} then measures how well the datasets A and B, fitted independently, match a certain hypothesis compared to the combined fit to the united dataset $A \cup B$. Concretely, χ^2_{PG} is defined by

$$\chi^2_{\mathrm{PG}} \equiv \chi^2_{\mathrm{min,global}} - \chi^2_{\mathrm{min},A} - \chi^2_{\mathrm{min},B} = \Delta\chi^2_A + \Delta\chi^2_B, \tag{4.3}$$

where $\chi^2_{\mathrm{min,global}}$ is the minimum of the χ^2-function, obtained from the fit to the complete dataset $A \cup B$, and $\chi^2_{\mathrm{min},A}$ and $\chi^2_{\mathrm{min},B}$ are the corresponding minima of the fit to the datasets A and B, respectively. The $\Delta\chi^2_i$ introduced in the second equality are defined as the respective differences between the minimum of the χ^2 function χ^2_i, which corresponds to the subset $i \in \{A, B\}$, and the value of χ^2_i evaluated at the global best fit point (BFP),

$$\Delta\chi^2_i \equiv \chi^2_i(\mathrm{BFP}) - \chi^2_{\mathrm{min},i}, \tag{4.4}$$

which is obviously always greater or equal to zero, $\Delta\chi^2_i \geq 0$. It is shown in [44] that χ^2_{PG} itself follows a χ^2 distribution with N_{PG} degrees of freedom, where the number N_{PG} is given by

$$N_{\mathrm{PG}} \equiv P_A + P_B - P, \tag{4.5}$$

and P_A and P_B are the numbers of parameters constrained by the subset A and B, respectively, whereas P is the total number of parameters of the model with $P_A, P_B \leq P$. Accordingly, the respective p-value can be calculated in the usual way by

$$p = \int_{\chi^2_{\mathrm{PG}}}^{\infty} dx\, f_{\chi^2}(x; N_{\mathrm{PG}}), \tag{4.6}$$

where $f_{\chi^2}(x; N_{\mathrm{PG}})$ denotes the probability density function of the χ^2 distribution corresponding to χ^2_{PG}. Hence the PG test quantifies the compatibility of the two subsets A and B by the p-value given in eq. (4.6). A formal derivation of this statistical measure and more details are given in [44].

4.3 $\overset{(-)}{\nu}_e$ disappearance data

4.3.1 Reactor experiments

[1]Preceding the combined fit to the global data in the $\overset{(-)}{\nu}_e$ disappearance channel, this section is dedicated to the analysis of the data measured by *reactor experiments*. The common denominator of this subset of experiments is that nuclear reactors, utilizing nuclear fission, provide the source of antineutrinos detected in the respective experiments. These antineutrinos are produced as byproducts in the reactors, because every fission is usually followed by a chain of beta decays, each releasing one electron antineutrino. Since the chemical elements created as fission products and thus the starting point of these decay chains are not determined definitely but follow a distribution, the antineutrino flux produced in a reactor is actually the superposition of the antineutrino beta spectra from thousands of possible decay branches [45]. This flux can be detected experimentally through inverse beta decay (IBD), where either the total *rate* of antineutrinos is registered, or the number of antineutrinos per energy bin, that is, an energy *spectrum* is measured.

The reason for going the extra mile and analysing the reactor data separately is that on the one hand the global fit in the $\overset{(-)}{\nu}_e$ disappearance channel is largely dominated by the reactor data, in particular NEOS, DANSS and the latest data from Daya Bay[2]. On the other hand, the interpretation of the reactor data crucially relies on the *theoretical prediction* of the flux generated by the respective reactor, which is, however, a non-trivial phenomenon, as explained above. Recent re-calculations of these fluxes in 2011 [46, 45] have resulted in an increased prediction compared to earlier publications. Taking these new calculations as a basis, the data measured by the reactor experiments on average lie below their respective predicted values. This discrepancy is known by the name reactor antineutrino anomaly (RAA). In the context of the $3+1$ model, the RAA could be explained by oscillations of electron antineutrinos into sterile neutrinos. However, the validity of the flux predictions is challenged by two recent experimental results. First, very precise measurements of the energy spectra exhibit a feature in the data, often described as “bump” or “shoulder”, around $E_\nu \sim 5\,\mathrm{MeV}$ which cannot be explained within the available theoretical models of these spec-

---

[1] The results presented in the current section, section 4.3, are mainly based on [2] and to some extent on [3]. Significant parts of these results were contributed by Álvaro Hernández-Cabezudo and the author. In particular, all plots containing only reactor data, figs. 4.1 and 4.2 as well as the corresponding statistical parameters, were provided by Álvaro Hernández-Cabezudo. The combined fit to the global data in the $\overset{(-)}{\nu}_e$ disappearance channel resulting in fig. 4.3 and the corresponding statistical parameters were contributed by the author.

[2] For references to the individual experiments used in this section, c.f. table 4.2.

tra [47]. Second, the Daya Bay collaboration explored the time-dependence of the IBD yield σ_f, which is a measure of the antineutrino detections per fission. The rate of change in the IBD yield is reported to be different from the rate of change theoretically expected due to the time-dependence of the fuel composition. Furthermore, the deviation from the theoretical predictions is *different* for the individual fission isotopes [48]. The latter result in particular, independent of the significance of the RAA, questions also the sterile neutrino oscillation hypothesis as is explained below.

Obviously without addressing the issues concerning the correct prediction of the reactor antineutrino flux and spectrum raised above, a sensible answer to the question whether reactor data can be fitted within the $3 + 1$ framework is not possible. Therefore, this section reviews the strategy on how to treat the reactor data consistently, which was developed in [2] an followed in [3]. This strategy is the basis for the global fit in the $\overset{(-)}{\nu}_e$ disappearance channel, reported on in section 4.3.2.

Concerning the reactor spectra, according to the point of view taken in [2], the data suggest that the theoretical model might be insufficient. Therefore the strategy is to eliminate the dependence on the disputed theory prediction by comparing spectral data to measured spectra at a different baseline. In table 4.2 it is indicated in the comments column whenever spectral information is used and the respective reference spectrum is given. For Bugey-3, which consists of three detectors at different baselines, the strategy is to introduce a free nuisance parameter for each energy bin. These nuisance parameters are then correlated one by one between the three detectors (for details, c.f. [2]). However, a small dependence on predicted spectra remains, encoded in the energy integral needed to predict total rates and for averaging each energy bin over the resolution function.

For the reactor rates, in principal the same strategy could be employed, that is a free nuisance parameter could be used such that the normalization of the fluxes from the reactors are completely unconstrained. However, it is not obvious whether this approach is justified. On the one hand, as for example the authors of [47] stress, a distortion of the spectrum does not necessarily imply a wrong prediction of the rate. In particular, these two effects should a priori be treated as two separate phenomena. On the other hand, the evidence for a nonuniform discrepancy between the fluxes coming from different fuel components and the respective predictions, as provided by the Daya Bay collaboration, seems to point in the direction of an inadequacy of the theoretical model.

Hence within the context of the $3 + 1$ model two hypotheses need to be contrasted in order to decide upon a prescription which determines what the reactor data should be compared to. The first or “fixed fluxes” hypothesis, H_0, states that the current predictions of the fluxes are correct and the mismatch with data is due to oscillations into sterile neutrinos. The second or "free fluxes" hypothesis, H_1, states that the normalization of the reactor fluxes is not modeled adequately for one or more of the fuel components and the mismatch with data can be resolved by solely rescaling the fluxes. A third hypothesis, stating that the flux predictions are modeled insufficiently *and* oscillations into sterile neutrinos occur, is possible yet neglected for the moment.

If H_0 turns out to be more likely then H_1, the appropriate strategy would be to take the flux predictions at face value, thus use "fixed fluxes". By contrast, if H_1 is more probable, the appropriate strategy would be to implement "free fluxes" in form of unconstrained priors for the individual flux components. The different potential of H_1 and H_0 to describe the Daya Bay dataset can be quantified by a test statistic T, defined by

$$T = \chi^2_{\text{min}}(H_0) - \chi^2_{\text{min}}(H_1). \tag{4.7}$$

The respective χ^2 functions for H_0 and H_1 need to be constructed according to the experimental details of the Daya Bay flux measurement. The collaboration provides the data in eight bins labeled by $a \in \{1 \dots 8\}$. Each bin a is characterized by the composition of the reactor fuel in fractions F_i^a of the primary fission isotopes ^{235}U, ^{238}U, ^{241}Pu and ^{239}Pu, where $i \in \{235, 238, 239, 241\}$. The predicted IBD yield in each bin a is given by

$$\sigma^a_{\text{pred}} = \sum_i P^i_{\text{osc}} \xi_i F_i^a \sigma_i^{\text{HM}}. \tag{4.8}$$

Since the fractions F^a_{238} and F^a_{241} were measured to be relatively small compared to the other two fractions, the contributions of ^{238}U and ^{241}Pu can be considered subleading below. In eq. (4.8), σ_i^{HM} denotes the IBD yield expected according to the references [46, 45]. P^i_{osc} is the oscillation probability at the detector, averaged over energy. It has to be evaluated according to the hypothesis under consideration, that is it depends on the $3+1$ oscillation parameters for H_0 and on the standard oscillation parameters for H_1. The four ξ_i are nuisance parameters which tune the normalization. Each of these nuisance parameters is associated with a prior $\chi^2_{\text{flux}}(\xi_i)$. The value of each prior $\chi^2_{\text{flux}}(\xi_i)$ again depends on the hypothesis. In the case of the hypothesis H_0, the four $\chi^2_{\text{flux}}(\xi_i)$ encode the systematic uncertainties on the fluxes, provided in [46, 45]. In the case of H_1, ξ_{235} and ξ_{239} are allowed to vary freely, that is the respective priors are zero, $\chi^2_{\text{flux}}(\xi_{235}) = \chi^2_{\text{flux}}(\xi_{239}) = 0$. However, also in the case of H_1 a weak 1σ prior of 10%[3] relative to [46, 45] is imposed on the flux normalizations ξ_{238} and ξ_{241}, corresponding to the subleading isotopes, to avoid unphysical results.

---

[3] This number was chosen to match the analysis of the Daya Bay collaboration. In the global fits, these priors on the subleading isotopes are set to the more conservative value of 20%.

The χ^2 functions can then be specified by

$$\chi^2 = \sum_{a,b=1}^{8} (\sigma^a_{\text{obs}} - \sigma^a_{\text{pred}}) V^{-1}_{ab} (\sigma^b_{\text{obs}} - \sigma^b_{\text{pred}}) + \chi^2_{\text{flux}}(\xi_i), \tag{4.9}$$

where V_{ab} is a covariance matrix encoding statistical and correlated systematic errors. σ^a_{obs} is the observed IBD yield in the a-th F_{239} bin, and σ^a_{pred} is the respective prediction according to eq. (4.8). With this definition, the test statistic T defined in eq. (4.7) can be evaluated. The result is

$$T_{\text{obs}} = 6.3\,, \qquad p\text{-value} = 0.7\%\ (2.7\sigma)\,, \tag{4.10}$$

where the p-value is evaluated by Monte Carlo simulation [2]. This result implies that the hypothesis H_0 is rejected with respect to H_1 at 99.3% confidence level (CL), which is in qualitative agreement with the value of $T = 7.9$ reported in [48]. As has been argued in [2], the reason for the slightly different results is that in eq. (4.9), the uncertainties on the flux predictions are included as described above, whereas these are neglected in [48].

The result given in eq. (4.10) is plausible according to physical reasoning. Pursuant to H_0, the fluxes from the individual isotopes are fixed within the respective uncertainties to the corresponding predictions. Therefore, to minimize the χ^2-function eq. (4.9), the only term that can be fitted without constraints is the oscillation probability P^i_{osc} contributing to the predicted IBD yield σ^a_{pred} given in eq. (4.8). However, P^i_{osc} has only a weak dependence on the isotope i due to the slightly different antineutrino spectra for each isotope. In the region $\Delta m^2_{41} \gtrsim 0.05$ eV^2, oscillations can be considered to be averaged out completely and therefore being independent of the energy spectrum. Accordingly, P^i_{osc} becomes independent of the isotope i and acts just as a global normalization factor, $P^i_{\text{osc}} \approx 1 - \frac{1}{2}\sin^2 2\theta_{14} \equiv P^{\text{glob}}_{\text{osc}}$. By contrast, pursuant to H_1, the fluxes from the individual isotopes are allowed to vary without constraints within their respective physical range, while $P^i_{\text{osc}} \equiv P^{\text{SM}}_{\text{osc}}$ is a constant in this scenario. Comparing the impact of these two hypotheses on the fit to the data showing nonuniform deviations from the theoretically expected value σ^{HM}_i, it is obvious that a uniform normalization factor is not expected to give a fit as good as adapted normalization factors for each of the fluxes might do.

The result for T, given in eq. (4.10), seems to imply that considering only the Daya Bay flux measurement, H_0 is rejected with respect to H_1. However, within both hypotheses, the data can be fitted very well, with a GOF p-value of 73% and 18%, respectively, as can be seen from table 4.1. It is therefore in particular advantageous that due to its precise measurement, it is possible to extrapolate from the Daya Bay data the predicted IBD yield in terms of various fractions of fission isotopes in the reactor fuel also for different reactor experiments. Combining this information with the knowledge about the composition

Analysis	χ^2_{min}/DOF	GOF	$\sin^2 2\theta_{14}^{\mathrm{BFP}}$	$\Delta\chi^2$(no osc)
H_0: fixed fluxes + ν_s	$9.8/(8-1)$	18%	0.11	3.9
H_1: free fluxes (no ν_s)	$3.6/(8-2)$	73%		

Table 4.1: Fits to the Daya Bay flux measurements based on the hypotheses H_0 and H_1. For H_0, the fluxes from the individual isotopes are fixed within the respective uncertainties to the corresponding predictions [46, 45] and $\bar{\nu}_e$ can oscillate into sterile neutrinos ν_s. Here, it is assumed that $\Delta m^2_{41} \gtrsim 0.05$ eV^2 holds, such that oscillations are expected to average out. Hence, the fit is performed with a single free parameter in the form of the mixing parameter $\sin^2 2\theta_{14}$, and the number of DOFs is one. The result of the fit for this parameter is given at the BFP. For H_1, the fluxes from the leading isotopes are allowed to vary without constraints, but θ_{14} is set to zero. Hence, in this scenario the fit is performed with two free parameters in the form of the nuisance parameters ξ_{235} and ξ_{239}. The GOF p-values are calculated by Monte Carlo simulation. They can be reproduced qualitatively assuming that the respective χ^2-functions defined in eq. (4.9) follow a χ^2-distribution.
Table taken from [2] (wording slightly modified).

of the reactor fuel for the individual experiments, for each experiment the corresponding χ^2-function can be evaluated once for H_0 and once for H_1. This allows for a comparison between H_0 and H_1 beyond the Daya Bay data set. This comparison can be complemented by the spectral ratios measured in reactor experiments, which constrain the oscillation probability into sterile neutrinos at various baselines independent from the predicted rates. Using this information, the above evaluation of the test statistic T can be extended to the global reactor data. The respective experiments are given in the first block of table 4.2. The only difference between the dataset presented in [2] compared to the dataset presented in [3] is that instead of the data set shown in March 2017 [49], the recent preliminary results from the DANSS experiment presented in December 2017 [50] are used. The exposure times between the two DANSS data samples approximately increased by a factor of four. The numerical values for T calculated in the respective references are

$$T_{\mathrm{obs}} = 2.9 \text{ [2]} \qquad \text{(all reactors, 2017)} \tag{4.11}$$

$$T_{\mathrm{obs}} = -1.3 \text{ [3]} \qquad \text{(all reactors, 2018),} \tag{4.12}$$

where for the combined analysis within the “flux free” approach correlations among the different rate measurements have been taken into account, that is, the nuisance parameters ξ_i introduced in eq. (4.8) are fitted globally, and the corresponding priors $\chi^2_{\text{flux}}(\xi_i)$ are added only once to the global χ^2-function. Correlations between the analyses of the spectra are not taken into account, except between Daya Bay and NEOS, which are both evaluated with respect to the same near detector. This approach can be considered slightly overconservative.

The results given in eqs. (4.11) and (4.12) imply that the initial preference for H_1 over H_0 of the Daya Bay only analysis decreases in the light of global reactor data. In particular the negative value for T in eq. (4.12) even expresses a slight preference of H_0 over H_1. The reason for these results can be understood from the spectral data, especially from DANSS and NEOS, depicted in fig. 4.1. Each of these spectra features modest distortions – less pronounced for DANSS (a) than for NEOS (b) – which can be fitted better by an oscillating function than by a constant. This is illustrated by the sample fit functions plotted on top of each set of data points. Already by eye it can be estimated that for instance the dashed lines, which correspond to the respective BFP of the individual fit to each of the spectra within the $3 + 1$ framework, reproduce the spectral features quite well. The numerical evaluation gives a difference of $\Delta\chi^2 = 13.6$ in the χ^2-functions between the BFP in the $3 + 1$ framework and the BFP assuming no oscillations involving the sterile state for the combined datasets from DANSS and NEOS. This corresponds to a rejection of the no-oscillation hypothesis at the 3.3σ significance level, as can be seen in the first row of table 4.3.

In summary this careful evaluation of the two hypotheses H_0 and H_1 on the basis of the global reactor data shows that neither of them can be rejected definitively. Furthermore, still another valid option is to leave the priors on the individual fluxes free and additionally allow for oscillations into sterile neutrinos. The corresponding hypothesis was previously called H_2 and not tested explicitly. However, since H_1 has proved valid, this applies all the more to H_2, because H_1 can be considered to be just a special case of H_2. Given that result, the appropriate strategy according to [2] is to consider two scenarios whenever reactor rates are involved: on the one hand, this is the scenario underlying H_0, that is, the rate predictions are taken at face value within the quoted uncertainties, and oscillations are calculated within the $3+1$ framework. On the other hand, within the second scenario, the flux normalizations for the two main fission isotopes are treated as free parameters and additionally oscillations into sterile neutrinos are also allowed.

With this strategy the reactor data can finally be evaluated within the $3 + 1$ framework. The relevant parameters to fit the data can be inferred from the vacuum survival probability $P_{\bar{e}\bar{e}}$ in the $3+1$ framework. It is obvious from eq. (2.29) that $P_{\bar{e}\bar{e}}$ only depends on the squared entries $|U_{ei}|^2$ of the first row of the mixing matrix, and hence the angles θ_{12}, θ_{13} and θ_{14}. In the SBL approximation eq. (4.2), applicable to most of the reactor experiments, all mass-squared differences except Δm^2_{41} are effectively zero. This approximation is not justified for

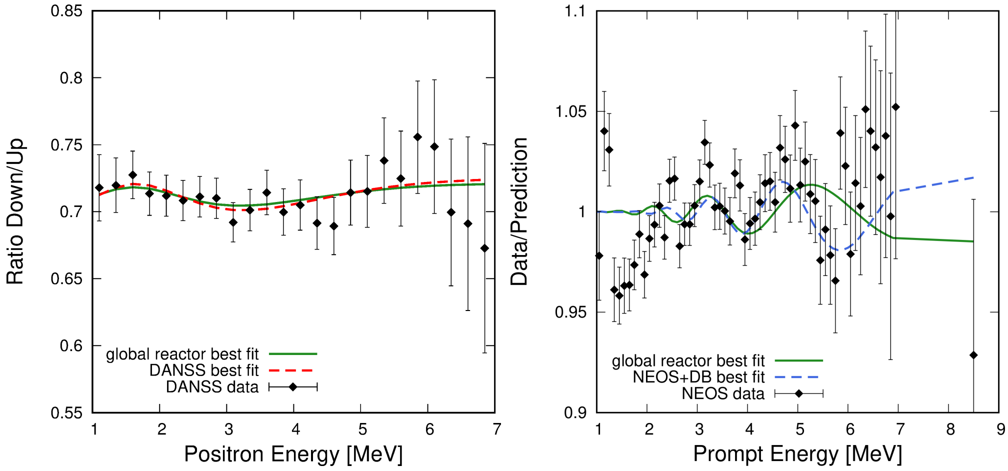

(a) (b)

Figure 4.1: Observed spectra for the DANSS (a) and NEOS (b) experiments compared to the predicted spectra at the individual best fit points (dashed) and the best fit point from a global analysis of all reactor data (solid). The left panel shows the ratio of the observed event rates at the two detector locations in DANSS (24 bins). The right panel shows the NEOS spectral data relative to the prediction extrapolated from the measured Day Bay spectrum (60 bins). The best fit points are $\Delta m^2_{41} = 1.32$ eV^2, $\sin^2\theta_{14} = 0.012$ for DANSS, $\Delta m^2_{41} = 1.78$ eV^2, $\sin^2\theta_{14} = 0.013$ for NEOS + Daya Bay, and $\Delta m^2_{41} = 1.29$ eV^2, $\sin^2\theta_{14} = 0.0089$ for the fit to all reactor data, assuming a free normalization for the neutrino fluxes from the four main fissible isotopes.
Figure and caption taken from [3].

LBL reactor experiments and KamLAND, which are instead sensitive to Δm^2_{31} and Δm^2_{21} respectively. Since on the other hand Δm^2_{21} and θ_{12} are not properly constrained by the reactor experiments alone but only in combination with solar data, they are fixed in the current fit to avoid unphysical values. Furthermore also Δm^2_{31} is fixed, thus the remaining parameters eventually used in the fit are θ_{13}, θ_{14} and Δm^2_{41}, and additionally the individual normalization parameters of the fluxes from ^{235}U and ^{239}Pu in the case of the “flux-free” scenario. Of course the oscillation probability is always calculated in terms of all relevant parameters, irrespective of whether these are free or fixed and at no point any (SBL-) approximation of the full oscillation probability is used. The result of the fit is shown in fig. 4.2 [3].

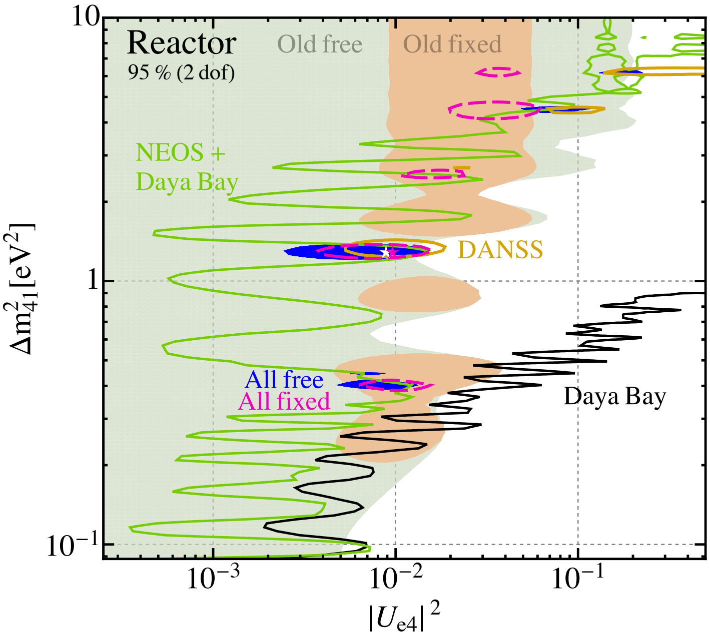

Figure 4.2: Allowed regions at 95% CL (2 DOF) from reactor data. The solid curves correspond to Daya Bay spectral data (black), NEOS + Daya Bay (green), and DANSS (orange); they are independent of assumptions on fluxes because they are only based on spectral ratios. The light-shaded areas labeled "old" correspond to all data from table 4.2 except Daya Bay, DANSS, NEOS, and they are shown for the flux-free analysis making no assumptions about flux normalization and spectra (light green), as well as for the flux-fixed analysis (light orange), assuming reactor flux predictions and their published uncertainties. The blue shaded regions correspond to all reactor data from table 4.2 for the flux-free analysis, whereas the dashed magenta contours indicate the global data for the flux fixed analysis. The white (pink) star indicates the best fit point $\Delta m^2_{41} = 1.29$ eV^2, $\sin^2\theta_{14} = 0.0089$ ($\Delta m^2_{41} = 1.29$ eV^2, $\sin^2\theta_{14} = 0.0096$) for free (fixed) reactor fluxes.
Figure and caption taken from [3].

In fig. 4.2, the shaded regions refer to the “old data”, predating the summer conferences 2016, once evaluated within the “flux-free” scenario, and once within the “flux-fixed” scenario. In the “flux-fixed” analysis, the RAA can be observed for the “old data”, that is at the 95% CL, sterile oscillations are preferred over no oscillations. In the “flux-free” analysis, this preference for sterile neutrinos disappears, however, the preferred parameter space in the “flux-fixed” scenario is consistent with the allowed parameter spaces in the “flux-free” scenario.

The recent spectral data from DANSS, NEOS and Daya Bay are shown as solid lines in fig. 4.2. The NEOS data are fitted together with the Daya Bay data, because the spectrum measured by NEOS is compared to spectra at the Daya Bay near detectors (NDs). While this combination of data leads to a closed region in the parameter space, the Daya Bay spectral data at the far detector compared to the same near detectors exclude the corresponding BFP below $\Delta m^2_{41} \simeq 0.1\,\mathrm{eV}^2$. The DANSS spectral data show a preference for the sterile neutrino oscillation hypothesis, while the Daya Bay spectral data as well as the combination of the NEOS and Daya Bay spectral data do not confirm this result. However, their limits exhibit pronounced, sinuous features, which can be traced back to the spectral features observed in fig. 4.1. These sinuous features are partly consistent with the regions preferred by DANSS. The DANSS BFP at $\Delta m^2_{41} = 1.78\,\mathrm{eV}^2$ is compatible with a local minimum $\Delta m^2_{41} = 1.3\,\mathrm{eV}^2$ in the combined NEOS and Daya Bay fit.

Finally fig. 4.2 shows that the parameter regions preferred by the “old data” using the “flux-fixed” approach are in mild tension with the preferred parameter regions of the recent spectral data from DANSS, NEOS and Daya Bay. Nevertheless, a combined fit to the global reactor data within the “flux-fixed” scenario increases the significance of the preference for sterile neutrino oscillations to 3.5σ compared to 3.3σ for the combined datasets of DANSS and NEOS quoted above, as can be seen from the third row in table 4.3. Using the “flux-free” approach, the significance decreases slightly to 2.9σ. The corresponding BFP is in good agreement with the DANSS data, as can be observed in fig. 4.1 (a). In this figure, the red, dashed line, representing the BFP found in the fit to the DANSS data only, is very close to the green, solid line representing the BFP of the combined fit to global reactor data. For the NEOS data shown in fig. 4.1 (b) the respective curves seem to differ significantly. However, the NEOS dataset is statistically dominated by the low energy part, where the two lines representing the different BFPs match actually rather well.

In conclusion, the result of the combined fit to the global reactor data is that oscillations into sterile neutrinos are preferred over no oscillations with a significance of $\sim 3\sigma$, independent from the assumption on the flux uncertainties. This indication for sterile neutrinos is driven by distortion in the various reactor spectra [3].

4.3.2 Global $\overset{(-)}{\nu}_e$ disappearance analysis

In this section, the detailed analysis of the global reactor data and the RAA reviewed in section 4.3.1 is put in the broader context of the global data in the $\overset{(-)}{\nu}_e$ disappearance channel. This is particularly interesting, because this dataset includes measurements that exhibit unresolved anomalies. In previous works, for example [51], it has been shown that these "gallium anomalies" can be fitted within the $3+1$ framework. These fits resulted in parameter spaces preferred by the reactor experiments and by the "gallium anomalies", which only partially overlap. However, the global data in the $\overset{(-)}{\nu}_e$ channel could be fitted rather consistently. This analysis has been repeated on the basis of recent reactor data in [2] and updated in [3] using the newest results from DANSS. After a short introduction of the non-reactor dataset going into these analyses, the results of the works cited above are reviewed in what follows.

A complete list of the experiments used in this section, including the references to the corresponding publications, is given in table 4.3. In this table, the experiments are grouped into blocks according to the respective neutrino source. Two experiments, SAGE and GALLEX, are enlisted twice. The reason for this is, that the calibration measurements of these experiments featured the "gallium anomalies" quoted above. Hence the calibration measurements and the measurements during the proper runtime of these experiments are treated separately.

The first block of table 4.3 is constituted by the reactor experiments already discussed in the previous section.

The second block of table 4.3 consists of solar neutrino experiments, which detect neutrinos produced in the sun. The results of these experiments can be impacted by two effects due to light sterile neutrinos. On the one hand, the mixing with sterile neutrinos would reduce the number of neutrinos measured on earth compared to what is theoretically expected within the Standard Solar Model. Hence, when measuring electron neutrinos, the mixing with sterile neutrinos would be detected as an overall flux reduction, proportional to U_{e4}. When measuring other neutrino flavors through NC interactions as for example in SNO, the impact on the normalization of the solar flux is affected also by other active-sterile mixing parameters, in particular θ_{24} and θ_{34}. On the other hand, also the MSW effect inside the sun, described in section 2.4 for SM neutrinos, receives corrections from the mixing with sterile neutrinos within the $3+1$ framework, c.f. [89]. This leads to a non-trivial dependence of the detection probability on all the six active-sterile mixing parameters in the $3+1$ framework, including the complex phases.

The third block of table 4.3 comprises experiments measuring electron neutrinos originating from the decay of intermediate particles, which are produced when a proton beam is directed onto a target. This production mechanism

Experiment	References	Data points	Comments	($\sum$ Data points)
Reactor experiments				(233)
ILL	[52]	1	rate	
Gösgen	[53]	3	rates	
Krasnoyarsk	[54, 55, 56]	4	rates	
Rovno	[57, 58]	5	rates	
Bugey-3	[59]	35	spectra at 3 distances with free bin-by-bin normalization	
Bugey-4	[60]	1	rate	
SRP	[61]	2	rates	
NEOS	[62, 63]	60	ratio of NEOS and Daya Bay spectra	
DANSS	[50]	24	ratios of spectra at two baselines (updated w.r.t. [2])	
Double Chooz	[64]	1	near detector rate	
RENO	[65, 66]	2	near detector rate	
Daya Bay spectrum	[67]	70	spectral ratios EH3/EH1 and EH2/EH1	
Daya Bay flux	[48]	8	individual fluxes for each isotope (EH1, EH2)	
KamLAND	[68]	17	very long-baseline reactor experiment ($L \gg 1\,\mathrm{km}$)	
Solar neutrino experiments				(325)
Chlorine	[69]	1	rate	
GALLEX/ GNO	[70]	2	rates	
SAGE	[71]	1	rate	
Super-Kamiokande	[72, 73, 74, 75]	165	Phases I–IV	
SNO	[76, 77, 78]	75	Phases 1–3 (CC and NC data)	
Borexino	[79, 80, 81]	81	Phases I and II	
ν_e scattering on carbon ($\nu_e + {}^{12}\mathrm{C} \to \mathrm{e}^- + {}^{12}\mathrm{N}$)				(32)
KARMEN	[82, 83, 84]	26		
LSND	[85, 84]	6		
Radioactive source experiments (gallium)				(4)
GALLEX	[86, 70]	2	ν_e from ^{51}Cr source	
SAGE	[87, 88]	2	ν_e from ^{51}Cr and ^{37}Ar sources	

Table 4.2: Experimental datasets included in the $\overset{(-)}{\nu}_e$ disappearance analysis. The total number of data points is 594. More details can be found in ref. [2]; the only update with respect to [2] is new data from DANSS [50].

Table and caption taken from [3] (wording for both slightly modified).

Note added by the author: technical details on the implementation of the respective experiments can be found in the appendix of [2] for Daya Bay, Neos and DANSS, and in the appendix of [51] for the remaining experiments.

of a neutrino source is described in more detail in section 4.4. Inside the detector, an electron neutrino can react with a carbon nucleus according to $\nu_e + {}^{12}\mathrm{C} \to \mathrm{e}^- + {}^{12}\mathrm{N}$. The detection signature comes from the decay of the very short-lived nitrogen atom back to carbon, ${}^{12}\mathrm{N} \to \nu_e + {}^{12}\mathrm{Ce}^+$, where both, the electron and the positron, are registered, allowing for a precise background rejection. Since these experiments are conducted at SBL where standard oscillations have not yet developed, they constrain the oscillation probability of electron neutrinos into sterile neutrinos.

Lastly, the fourth block contains the calibration measurements of SAGE and GALLEX, as mentioned above. These were performed twice for both experiments. In each round, a probe of a radioactive element – ^{37}Ar and ^{51}Cr in the case of SAGE, and both times ^{51}Cr in the case of GALLEX – was placed inside of the respective detector as a neutrino source providing a precisely known flux. The detector material in both cases is gallium. The detection principle exploits the radioactivity of the isotope ^{71}Ge: since ^{71}Ge is produced by electron neutrinos from the gallium inside the detector according to $\nu_e + {}^{71}\mathrm{Ga} \to \mathrm{e}^- + {}^{71}\mathrm{Ge}$, counting the decays of ^{71}Ge reveals the number of neutrinos interacting in the detector. In all four calibration runs a rate 10% to 20% less than theoretically expected was measured, a finding known by the name “gallium anomaly”. While it is established that transitions of the gallium atoms into two excited states of ^{71}Ge besides the ground state are possible, their impact has been up for debate. However, as the authors of [90] argue, even assuming no contribution at all from the disputed excited states of ^{71}Ge cannot compensate for the measured deficit. Independent of this argument, recent measurements of the Gamov-Teller strength entering the theoretical predictions have confirmed previous experimental results [90]. Within the 3 + 1 framework, the gallium anomaly can be explained by SBL oscillations of the electron neutrinos into sterile neutrinos within the respective detector volume.

Although the exploited source of neutrinos is different for each of the set of experiments subsumed above under the tags reactor, solar, scattering on carbon and radioactive source, uncertainties of the individual experiments within one category might not be independent from one another. For the global analyses performed in [2, 3], these correlations among the experiments within each category have been taken into account. Nevertheless, such correlations could in principle as well occur between experiments assigned to different categories. In particular, such correlations are obviously expected for the calibration runs of SAGE and GALLEX and their actual measurements of solar neutrinos. However, as reported in [2], the different spectra of the neutrinos measured during calibration and at runtime introduce different systematic errors. This is because the neutrinos detected at runtime induce mainly transition of ^{71}Ga to the ground state of ^{71}Ge, whereas the main source of uncertainty during the calibration runs is due to the transitions of ^{71}Ga into excited states. Therefore it was argued in [2] that correlations between experiments assigned to different categories within the $\overset{(-)}{\nu}_e$ disappearance channel can be neglected.

The result of the fit to these experiments is shown in fig. 4.3 and the corresponding statistical quantities are enlisted in table 4.3 [3]. The parameters which have been scanned in the fit are given in the first row of table 4.6. Compared to the set of parameters discussed above, which were used to fit the reactor data, the previously fixed parameters θ_{12}, Δm^2_{21} and Δm^2_{31} need to be added. This is because by including the results from the solar experiments the dataset becomes sufficiently sensitive to these additional parameters. The solar data are furthermore sensitive to θ_{24}, θ_{34} as well as to the complex phases as has been discussed above. However, the impact of the phases has been found to be marginal, therefore these are not counted as extra DOFs. On the other hand, θ_{13} is now fixed to reduce the complexity of the fit. This is justified because the uncertainties on θ_{13} are very small, and furthermore it has been shown in [51] that the determination of θ_{13} is not impacted by the existence of sterile neutrinos.

In fig. 4.3, the light and dark blue shaded areas refer to the parameter regions preferred by the reactor data in the "flux free" scenario at 95% and 99% CL, respectively. These regions are virtually congruent with the regions shown in fig. 4.2. Since the corresponding preferred parameter regions in the "flux-fixed" scenario are very similar at low Δm^2_{41} but shifted somewhat to lower values of the mixing parameter $|U_{e4}|$ for higher Δm^2_{41} as can be observed in fig. 4.2, the "flux free" scenario depicted in fig. 4.3 corresponds to the more conservative result in this case. The black, dashed lines correspond to the limits of the solar data on high values of the mixing parameter $|U_{e4}|$. Since for solar neutrinos to good approximation $\Delta m^2_{21} \times L/E$ is of order $\mathcal{O}(\Delta m^2_{21} \times L/E) \lesssim 1$, the oscillatory factors due to the other mass parameters $\Delta m^2_{i1} \approx \Delta m^2_{i2}$ can be safely assumed to average out, since $\Delta m^2_{i1} \times L/E \approx \Delta m^2_{i1}/m^2_{21} \to \infty$ for $i > 1$. Because of this approximation, the limit obtained from the solar data is independent of Δm^2_{41}. The main tension of the solar data with the sterile neutrino hypothesis is due to the fact that the mixing with the sterile neutrino would effectively reduce the solar neutrino flux. However, in particular the flux originating from the decay of ^{8}B in the sun is in very good agreement with theoretical calculations, which sets an upper bound on $|U_{e4}|$. This limit is complemented at high Δm^2_{41} by the limits of LSND and KARMEN, shown as brown, dot-dashed lines, which did not report any deviations from the standard oscillation scenario.

For comparison, also the limits from the atmospheric neutrino experiments SuperKamiokande (SK), IceCube (IC) and DeepCore (DC) are shown, although they are not included in the global fit to the $\overset{(-)}{\nu}_e$ disappearance data. Similar to the case of the solar data discussed above, the main impact of sterile neutrino on the low-energy atmospheric data from SK and DC is a constant reduction of the muon and electron neutrino survival probabilities [91]. In the analysis of these

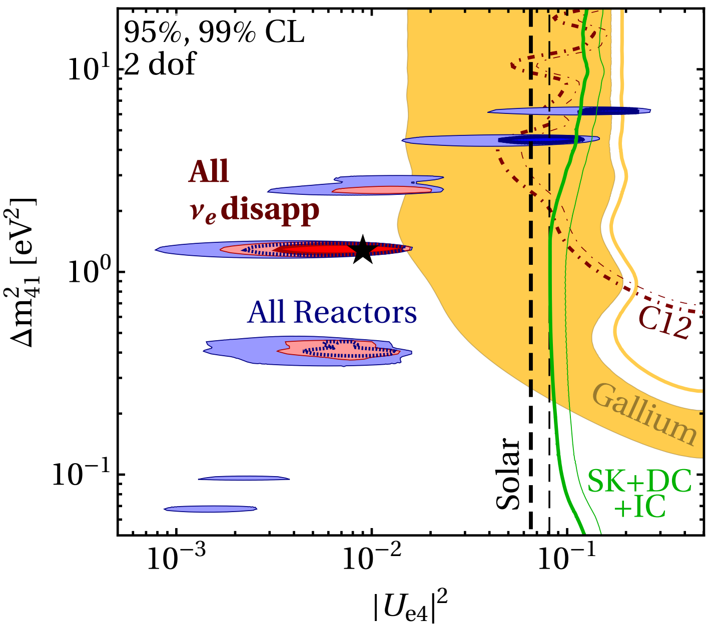

Figure 4.3: Constraints derived in the $\overset{(-)}{\nu}_e$ disappearance channel, projected onto the plane spanned by the mixing matrix element $|U_{e4}|^2$ and the mass squared difference Δm^2_{41}. The parameter space to the left of the thin lines and inside the light-shaded regions is allowed at 99% CL while the parameter space inside the dark-shaded regions and to the left of the thick lines is allowed at 95% CL. The reactor analysis, shown in blue, relies on the assumption of "flux-free" normalizations. For comparison the green curves indicate the limits on $|U_{e4}|^2$ obtained from the atmospheric neutrino experiments SK, IC and DC. These experiments are discussed in more detail in section 4.5. The red regions represent the constraints from all data combined, excepting the atmospheric experiments SK, IC and DC. The corresponding experiments are enlisted in table 4.2.
Figure taken from [3]

data, a correlated uncertainty on the normalization of the muon neutrino flux and the electron neutrino flux is imposed. However, from the high-energy data from IC, the reduction of the muon flux due to sterile neutrinos is independently strongly constrained, as will be discussed in section 4.5. Therefore the combination of these three experiments imposes a constraint on the mixing parameter $|U_{e4}|$ which is comparable to the constraint from the solar data (c.f. [3] for further details on the argument). By contrast to the scenario shown in fig. 4.3, all the limits discussed above would be fully consistent with the regions preferred by reactor data in the case of the “flux-fixed” analysis.

The parameter region shown in yellow is preferred at 95% CL by the data measured by the radioactive source experiments to resolve the “gallium anomaly”. At 99% CL, these data do not result in closed contours and are thus compatible with the no-oscillation hypothesis. The parameter regions preferred by the radioactive source data and by the reactor data, respectively, overlap only partly. A combined fit to these two datasets converges to the parameter region around $\Delta m_{41}^2 \sim 4.5\,\text{eV}^2$ allowed by both, which is, however, disfavored by the limits from solar data and the dataset obtained from LSND and KARMEN.

Finally the light and dark red shaded areas display the parameter regions preferred by the combined fit to the global data in the $\overset{(-)}{\nu}_e$ disappearance channel at 95% and 99% CL, respectively. Since the constraint on small mixing due to the dataset from the radioactive source experiments is rather weak, with zero mixing being allowed at 99% CL, the fit is dominated by the reactor data. Consequently, the region preferred by the global fit as well as the BFP are actually disjoint to the region preferred by the GALLEX and SAGE dataset. At the BFP, the PG test, reviewed in section 4.2, gives a p-value of $p_{\text{PG}} = 3.1\%$ for the comparison of data from the radioactive source experiments and the reactor experiments, which indicates a minor tension between these datasets. Nevertheless, the significance of the preference for oscillations of electron (anti)neutrinos into sterile neutrinos increases slightly compared to the reactor only fit in the previous section, as can be seen in the last column of table 4.3. In the “flux-fixed” scenario, this significance is as high as 3.8σ, for the more conservative “flux-free” scenario, it is still well above 3σ.

Analysis	Δm^2_{41}	$\lvert U^2_{e4}\rvert$	$\chi^2_{\text{min}}/\text{DOF}$	$\Delta\chi^2(\text{no-osc})$	significance
DANSS +NEOS	$1.3\,\text{eV}^2$	0.00964	$74.4/(84-2)$	13.6	3.3σ
Reactor fluxes floating freely					
all reactor	$1.3\,\text{eV}^2$	0.00887	$185.8/(233-5)$	11.5	2.9σ
$\overset{(-)}{\nu}_e$ disappearance	$1.3\,\text{eV}^2$	0.00901	$542.9/(594-8)$	13.4	3.2σ
Reactor fluxes fixed at predicted value ± quoted uncertainties					
all reactor	$1.3\,\text{eV}^2$	0.00964	$196.0/(233-3)$	15.5	3.5σ
$\overset{(-)}{\nu}_e$ disappearance	$1.3\,\text{eV}^2$	0.0102	$552.8/(594-6)$	17.5	3.8σ

Table 4.3: Best fit values and statistical parameters obtained in the $\overset{(-)}{\nu}_e$ disappearance channel, sorted by the datasets underlying the analysis. The global reactor dataset and the full $\overset{(-)}{\nu}_e$ disappearance dataset with the corresponding experiments enlisted in table 4.2, include rate measurements. Therefore, for these data, the fit is performed one time with fluxes fixed and one time with fluxes floating freely. In each of the fits, θ_{14} and Δm^2_{41} are free parameters. In addition, θ_{13} is a free parameter in the fits to the "all reactor" dataset, while in the analyses of the "$\overset{(-)}{\nu}_e$ disappearance" data, the parameters listed in the first row of table 4.6 are fitted, see text for explanations on the choice of parameters. Furthermore, as explained in section 4.3.1, in the "flux-free" approach, the normalization of the ^{235}U and ^{239}Pu fluxes are treated as free parameters, while a prior is imposed on these parameters in the "flux-fixed" approach. For each of the fits, the next-to-last column enlists the difference $\Delta\chi^2(\text{no-osc})$ between the χ^2 function at the respective BFP and the χ^2 function evaluated for no oscillations. The last column gives the significance at which the no-oscillation hypothesis is disfavoured for each dataset, assuming that $\Delta\chi^2(\text{no-osc})$ is distributed according to a χ^2 distribution with two degrees of freedom.

Table (slightly modified) taken from [3].

4.4 $\overset{(-)}{\nu}_e$ appearance data

[4]As stated above, the term "$\overset{(-)}{\nu}_e$ appearance channel" refers to the specific setting of neutrino experiments, where the initial particles are muon neutrinos or antineutrinos whereas the detector is sensitive to electron neutrinos or antineutrinos. Consequently this channel is in fact sensitive to the process $\overset{(-)}{\nu}_\mu \to \overset{(-)}{\nu}_e$ and hence the detection of the respective (anti)particle effectively measures the probability of a flavor change from muon to electron flavor. A potential deviation from the probability predicted in the standard three-flavor scenario can in the 3+1 framework be interpreted as an oscillation of the initial muon (anti)neutrino into a sterile neutrino which then oscillates into an electron (anti)neutrino. Consequently, the process $\overset{(-)}{\nu}_\mu \to \overset{(-)}{\nu}_e$ measured in the $\overset{(-)}{\nu}_e$ appearance channel is often parametrized by an effective muon-electron mixing parameter $\sin^2 2\theta_{\mu e}$ (c.f. eq. (4.13)).

The $\overset{(-)}{\nu}_e$ appearance channel adds an interesting aspect to the complex picture of neutrino oscillations. On the one hand, the first and since then long withstanding hint of oscillations beyond the standard three-flavor paradigm has been measured by LSND[5] using the $\overset{(-)}{\nu}_e$ appearance channel. This unresolved anomaly is complemented by the enigmatic data from the MiniBooNE experiment, reporting an excess in the low-energy bins, which is, however, not perfectly compatible with LSND [51]. While furthermore earlier results from MiniBooNE could not be fitted very compellingly within the $3+1$ framework, leading to a rather poor GOF, new results dating from 2018 can be fitted with a perfectly reasonable GOF of $\sim 20\%$. The combination of the LSND dataset and these recent results from MiniBooNE imply that the hypothesis of oscillations involving one sterile neutrino are preferred over the no-oscillation hypothesis at the 6.1σ CL [92][6]. On the other hand, other experiments, which – partly motivated by the LSND anomaly – probed similar ranges of $L/E \sim 1\,\mathrm{MeV/m}$, did not confirm the preference for oscillations involving sterile neutrinos. In this section, the global dataset in the $\overset{(-)}{\nu}_e$ appearance channel is evaluated in detail by reviewing the combined fit to these data in the $3+1$ framework performed in [3].

---

[4] The results presented in the current section, section 4.4, as well as sections 4.5 to 4.7, are mainly based on [3]. Significant parts of these results were contributed by the author. In particular, all plots shown in sections 4.4 to 4.7 as well as the corresponding statistical parameters and the PG analyses were provided by the author. This includes running the simulations of the underlying data on a high performance computing cluster. For descriptions of the individual analyses of the experimental results and acknowledgment of the respective authors, c.f. the references in the captions of tables 4.2, 4.4 and 4.5.

[5] For references to the individual experiments used in this section, c.f. table 4.4.

[6] Because this chapter is mainly based on [3], predating the newest publication of the MiniBooNE collaboration, the results presented here and especially in the global analysis section 4.7 still rely on the older data reported in [93, 94] if not stated otherwise.

Experiment	References	Data points	Comments
LSND	[95]	11	$\bar{\nu}_\mu$ from stopped pion source (DaR)
LSND	[95]	N/A	combined DaR and DiF data ($\overset{(-)}{\nu}_\mu \to \overset{(-)}{\nu}_e$)
MiniBooNE	[93, 94] ([92])	22	ν_μ and $\bar{\nu}_\mu$ from high-energy Fermilab beam
KARMEN	[96]	9	$\bar{\nu}_\mu$ from stopped pion source
NOMAD	[97]	1	ν_μ from high-energy CERN beam
E776	[98]	24	ν_μ and $\bar{\nu}_\mu$ from high-energy Brookhaven beam
ICARUS	[99, 100]	1	ν_μ from high-energy CERN beam
OPERA	[101]	1	ν_μ from high-energy CERN beam

Table 4.4: Experimental datasets included in the $\overset{(-)}{\nu}_e$ appearance analysis. As explained in more detail in the text, the LSND data consist of the two subsets called DiF data and DaR data. For the analysis of the full LSND dataset, a χ^2 table provided by the collaboration is used. This χ^2 table cannot be associated with a number of data points. When using LSND DaR data only, the total number of data points in the $\overset{(-)}{\nu}_e$ appearance is 69. Technical details on the implementation of the respective experiments listed above, except for OPERA, can be found in [51], and references therein.
Table (wording/ order of columns slightly modified) taken from [3].

The experiments used in this analysis are enlisted in table 4.4, where also references to the original publications of the respective collaborations are given. The individual experiments share the basic principle of a proton beam which is directed onto a target, such that the energetic beam protons interact with the target material. In this process, secondary particles, essentially mesons and (anti)muons are created as parent material. In the subsequent decay of these particles muon (anti)neutrinos are produced.

In the case of LSND and KARMEN, the intended parent particles were positive muons, which decay into muon antineutrinos and hence provided the experiments with the desired antineutrino source. The electron neutrinos which are produced in the same decay were used in the LSND experiment to explore neutrino oscillations in the $\overset{(-)}{\nu}_e$ disappearance channel, as has been described in section 4.3.2. The parent muons themselves were produced from the decay of positive pions. The major fraction of both parent particles, the positive pions and the positive muons, came to a halt in the beam stop and decayed subsequently. Since the decay spectra of both parent particles are well-known and the kinematics of the decay are particularly simple because the process occurs at rest, the resulting spectrum of the muon antineutrinos can be predicted quite accurately. This dataset, corresponding to the channel $\bar{\nu}_\mu \to \bar{\nu}_e$, is known under the name of “decay at rest (DaR) data”. However, the LSND collaboration has also exploited the flux of muon neutrinos from negative pions. These cannot decay at rest, because they get absorbed by the nuclei in the target material as soon as they are slow enough. However, a small fraction of these negative pions decays into muon neutrinos while still in flight. Using this process, the LSND detector can also record data in the channel $\nu_\mu \to \nu_e$, known under the name “decay in flight (DiF) data”. Since the uncertainties are higher in this channel, the bounds are less stringent. The global fit [3] reviewed below takes two different approaches to the LSND results: whenever a dataset is tagged “DaR” a full implementation of the LSND measurement of the DaR data is used and analyzed within the full 3+1 framework. Conversely, whenever a dataset is tagged “DiF”, the respective χ^2 values are extracted from a table kindly provided by the LSND collaboration. This table corresponds to an analysis of the combined DaR and DiF datasets, using however a two-flavor framework. Therefore, in order to utilize the information extracted from this table, the full oscillation probability in the $3+1$ framework is reduced to an effective two flavor oscillation formula in this case.

The MiniBooNE experiment measures also both, the $\bar{\nu}_\mu \to \bar{\nu}_e$ and $\nu_\mu \to \nu_e$ channel. Its detector cannot distinguish $\bar{\nu}_e$ from ν_e on an event-by-event basis. The sensitivity to the respective channels is instead achieved by filtering the beam of secondary mesons by a magnetic horn with variable polarity such that either a beam of positive mesons decaying predominantly to muon neutrinos or a beam of negative mesons decaying predominantly to muon antineutrinos is selected. The high energy of the parent particles in combination with a rather short length of the decay pipe suppresses the (anti)neutrino flux from the decay of muons relative to the flux from the decay of mesons due to the longer lifetime of muons.

Similarly, the older E776 experiment was operated in $\nu_\mu \to \nu_e$ mode as well as in $\bar{\nu}_\mu \to \bar{\nu}_e$ mode, which could be selected by adapting the polarity of a magnetic horn filtering the parent mesons. Since the experiment exhibited a rather large intrinsic background of $\overset{(-)}{\nu}_e$ due to contamination of the neutrino beam, for a consistent interpretation within the $3+1$ framework also potential oscillations of that background with sterile neutrinos need to be accounted for, as explained in [51]. To disentangle the effect of potential background oscillations $\overset{(-)}{\nu}_e \to \overset{(-)}{\nu}_e$ from oscillations in the signal channel $\overset{(-)}{\nu}_\mu \to \overset{(-)}{\nu}_e$, a reasonable strategy is to analyze the E776 data in combination with a different dataset, which provides for an independent constraint on $\overset{(-)}{\nu}_e \to \overset{(-)}{\nu}_e$ oscillations. In the analysis performed in [3], which this section is based on, the results of E776 have hence been combined with the data from solar experiments discussed in the previous section. This external constraint is redundant when the global data in the $\overset{(-)}{\nu}_\mu \to \overset{(-)}{\nu}_e$ channel are analyzed simultaneously, because the combination of these results provides enough constraints on background oscillations by itself.

The experiments NOMAD, ICARUS and OPERA all utilized a high-energy proton beam produced by the Super Proton Synchrotron (SPS) at CERN. In all cases, the beam of secondary particles was filtered for positive charge. The remaining mesons subsequently decayed in a decay pipe producing a fairly pure muon neutrino beam. While the NOMAD detector was located several hundred meters away from the neutrino source, the ICARUS and OPERA experiments reside in the Gran Sasso Laboratory, which is situated underground near L'Aquila, Italy, $\sim 730\,\text{km}$ from the source at CERN.

For most of the experiments described above, the SBL approximation introduced in eq. (4.2) is legitimate, which depends on the product of the mixing parameters $4|U_{\alpha 4}|^2|U_{\beta 4}|^2$, where $\alpha, \beta = e, \mu$ for the $\overset{(-)}{\nu}_e$ appearance data. It is useful to absorb the product of the two matrix elements into a single parameter as follows

$$\sin^2 2\theta_{\mu e} \equiv 4|U_{e4}|^2|U_{\mu 4}|^2, \tag{4.13}$$

because with this definition the probability for the process $\overset{(-)}{\nu}_\mu \to \overset{(-)}{\nu}_e$ can be written as

$$P^{\text{SBL}}_{\overset{(-)}{\mu}\overset{(-)}{e}} = \sin^2 2\theta_{\mu e} \sin^2\left(\frac{\Delta m^2_{41} L}{4E}\right). \tag{4.14}$$

This expression is formally equivalent to a two-flavor picture, where the two flavor eigenstates are transformed to the respective mass eigenstates by the two-dimensional mixing matrix $U(\theta_{\mu e})$, which depends solely on the mixing angle $\theta_{\mu e}$. The respective mass eigenstates in this two-flavor picture are split by the mass-squared difference Δm^2_{41}. However, of course taking into account the global data, which are widely consistent with the three-flavor picture, it is obvious that there are no two flavor eigenstates which would correspond to the states resulting from the transformation of the mass eigenstates with the two-dimensional transformation matrix $U(\theta_{\mu e})$. In particular, the effective mixing parameter given in eq. (4.13) should not be mistaken for a measure of the composition of for instance the mass eigenstate m_1 in terms of the electron and muon flavor states.

For the ICARUS and OPERA experiments, the SBL approximation eq. (4.2) discussed above is not applicable, because the baseline is so long that also oscillations due to the standard mixing are important. In particular, these experiments are sensitive to Δm^2_{31} and θ_{13} as well as the complex phase δ_{13}. However, in the combined fit to global data in the $\overset{(-)}{\nu}_e$ appearance channel, Δm^2_{31} and θ_{13} are kept fixed, since their effect might be partly degenerate with the effect of oscillations in the presence of sterile neutrinos which cannot be resolved within that dataset. The complex phase is scanned, but its impact on the fit was found to be of minor importance, hence it is not counted as additional DOF. The remaining parameters of the fit are therefore Δm^2_{41} as well as U_{e4} and $U_{\mu 4}$. However, as per eqs. (2.27) and (2.29) the oscillation probability only depends on the product $U^*_{e4}U_{\mu 4}$ or $U_{e4}U^*_{\mu 4}$ of these mixing parameters. Since furthermore the experiments in the $\overset{(-)}{\nu}_e$ appearance channel are to very good approximation insensitive to the complex phase δ_{24}, the two sole remaining parameters are thus Δm^2_{41} and $|U_{e4}U_{\mu 4}|$, as stated in table 4.6. The latter parameter can be converted to the effective mixing parameter defined in eq. (4.13) without loss of generality. Since the parametrization in terms of $\sin^2 2\theta_{\mu e}$ is very common in the literature, this convention is followed in the discussion of the $\overset{(-)}{\nu}_e$ appearance dataset below. The fit was performed with only the two parameters discussed above left free, while the relevant phases were scanned but not counted as DOFs due to their minor contribution. Note however, that the effective two-flavor probability given in eq. (4.14) was not explicitly employed, except for the LSND "DiF" dataset, as discussed above. Instead, the remaining oscillation parameters were fixed to their respective BFPs, and the oscillation probability was always calculated on the basis of all parameters.

The results of the combined fit to the global data in the $\overset{(-)}{\nu}_e$ appearance channel is depicted in fig. 4.4. The first two plots (a) and (b) in fig. 4.4, taken from [3], are based on the dataset predating the new results from the MiniBooNE collaboration on the $\nu_\mu \to \nu_e$ channel, published in May 2018. For reference, in

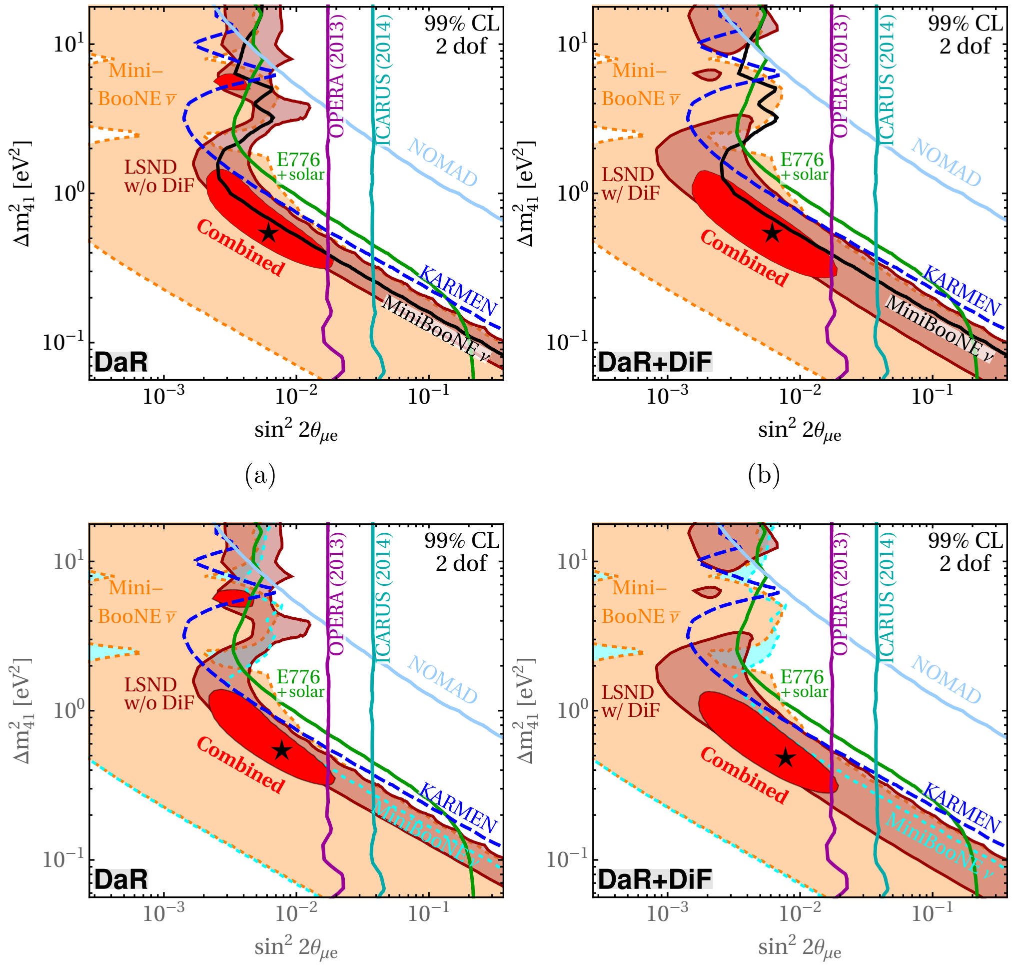

(a) (b)

(c) (d)

Figure 4.4: Constraints derived in the $\overset{(-)}{\nu}_e$ appearance channel, projected onto the plane spanned by the effective mixing angle $\sin^2 2\theta_{\mu e}$, defined in eq. (4.13) and the mass squared difference Δm^2_{41}. As explained in the text, the LSND data consist of two separate datasets called “DaR” and “DiF” data. The plots on the left are obtained from a dataset including only the DaR subset of the LSND data. The plots on the right are obtained from the complete $\overset{(-)}{\nu}_e$ appearance data, including both, the LSND DiF as well as DaR data. The first row, panels (a) and (b), are based on the MiniBooNE data on ν_e appearance published in 2012. The corresponding constraint at 99% CL is shown by a black line. The second row, panels (c) and (d), are based on the new data on ν_e appearance, released by the MiniBooNE collaboration in 2018. The corresponding allowed parameter space at 99% CL is represented by the light cyan region. Differences with regard to the official results presented in [92] are due to new Monte Carlo predictions and covariance matrices, which have not been provided by the collaboration yet. Instead, the MiniBooNE results shown in the panel (c) and (d) are based on the rescaled Monte Carlo predictions and covariance matrices released in 2012. Panels (a) and (b) taken from [3].

fig. 4.4 (c) and (d) the analysis including the new MiniBooNE data is shown. The plots in the left column are exploiting an implementation of the LSND DaR dataset, while the plots in the right column rely on tabulated χ^2 values corresponding to a combined analysis of the DaR and DiF data, as has been explained earlier in this section. The corresponding statistical parameters are given in the first two rows of table 4.7. As has been described in [3], for the DiF dataset the number of data points cannot be specified. Consequently it is not possible to associate a GOF to any fit involving the DiF analysis. As can be seen from table 4.7, for the fit including the DaR analysis the GOF, being $\sim 3\%$, is rather poor. This is on the one hand due to the spectrum measured by E776, which cannot be fitted well in the $3+1$ framework. On the other hand, the MiniBooNE dataset contributes to the low GOF value, because, as explained earlier, it exhibits a pronounced excess in the first few low-energy bins in both, the $\nu_\mu \to \nu_e$ channel and the $\bar{\nu}_\mu \to \bar{\nu}_e$ channel. However, each of these spectra cannot be fitted very compellingly in the $3+1$ framework. Furthermore, the two spectra differ from one another in the low energy bins. This feature cannot be explained within the $3+1$ framework, because it does not allow for CP violation at SBL. This can be seen from the SBL limit given in eq. (4.2) and holding to very good approximation for MiniBooNE, which does not contain any phases that could be fitted to CP violating data.

Despite the low GOF, the data in the $\overset{(-)}{\nu}_e$ appearance channel allow for a fairly consistent interpretation in the $3+1$ framework as can be observed from fig. 4.4. The colored lines show the regions disfavored by KARMEN, NOMAD, OPERA and ICARUS at 99% CL. The green line represents the limit from the combined fit to E776 and solar data, which are included to constrain background oscillations, as explained above. For the MiniBooNE dataset dating from 2012, which the analysis [3] is based on, the results in the $\nu_\mu \to \nu_e$ mode also do not lead to a preference for oscillations involving sterile neutrinos, because the corresponding spectrum cannot be fitted well enough based on an oscillatory pattern. By contrast, the newly published results dating from 2018 feature a less pronounced excess in the low energy bins, such that the spectrum is more compatible with oscillations in the $3+1$ framework. This leads also to a closed region favored by the MiniBooNE neutrino appearance data, shown in light cyan in fig. 4.4 (c) and (d). This parameter region is widely consistent with the region preferred by the MiniBooNE antineutrino data.

The limit by ICARUS shown in dark cyan and the somewhat stronger limit by OPERA shown in purple are almost independent from the mass squared difference Δm^2_{14} because to good approximation oscillations corresponding to this parameter are averaged out due to the very long baseline of these experiments. Nevertheless, these data were analyzed assuming two DOFs in order to allow for comparability with the remaining datasets. As has been noted in [3], the resulting limits deviate slightly from the ones presented in the respective original publications given in table 4.4, because in contrast to the original analyses, for the limits shown in fig. 4.4, oscillations of the background have been accounted for.

At high values of Δm^2_{14}, the strongest limit is provided by KARMEN, represented by a dark blue, dashed line. While the contour of KARMEN resembles that of LSND, KARMEN is compatible with zero mixing at 99% CL and hence could not confirm the strong preference of LSND for oscillations involving sterile neutrinos.

The orange shaded area is the parameter region preferred by the MiniBooNE antineutrino appearance data. This region is largely consistent with the region preferred by the LSND data.

The parameter region preferred by LSND is colored in brown. The impact of including the DiF data compared to the DaR only analysis on the favored region, shown in fig. 4.4 (a)/(c) and (b)/(d), respectively, is relatively small. In the main, the preferred parameter space broadens when including the DiF data, except for a small region around $\gtrsim 2\,\mathrm{eV}$. Most notably, the DiF datasets are compatible with slightly smaller mixing especially for $\Delta m^2_{14} \sim 1\,\mathrm{eV}$. In both cases the LSND datasets dominate the analysis of the $\overset{(-)}{\nu}_e$ appearance channel, disfavoring the no-oscillation hypothesis by $\Delta\chi^2 = 44$ based on the DaR data and still by $\Delta\chi^2 = 29$ including the DiF data [3].

Finally the result of the combined fit to the global data in the $\overset{(-)}{\nu}_e$ appearance channel is represented by the red shaded areas in fig. 4.4. The respective BFPs are marked by a black star. The size, position and shape of the preferred parameter region as well as the position of the BFPs are relatively independent from the inclusion of the LSND DiF data. Furthermore the impact of the new MiniBooNE neutrino appearance data is small. The reason is that the upper bound on the mixing parameter $\sin^2 2\theta_{\mu e}$ is dominated by MiniBooNE, especially the neutrino appearance data. However, this bound is not changed noticeably by the newly published results. The lower limit on $\sin^2 2\theta_{\mu e}$ is dominated by the respective LSND data. But the combined datasets favor rather low ranges of $\Delta m^2_{14} \lesssim 1\,\mathrm{eV}$ where the impact of the inclusion of the LSND DiF data is small. The respective preference for oscillations involving sterile neutrinos increases to $\chi^2 = 46$ and $\chi^2 = 35$ when adding the DaR only data or the combined DaR and DiF data, respectively, to the global dataset, in the case of the old MiniBooNE data [3]. This is because the MiniBooNE antineutrino data support the hint of LSND in favor of oscillations with sterile neutrinos, yet the fit is dominated by LSND.

4.5 $\overset{(-)}{\nu}_\mu$ disappearance data

[7]The data measured in the $\overset{(-)}{\nu}_\mu$ disappearance channel do not feature any significant anomaly that would call for an explanation beyond the three flavor paradigm. Instead, the great consistency of the results in this channel with the standard oscillation theory allows to set strong limits on the parameters in the $3+1$ framework. This section provides a detailed review of the limits obtained from the global data in the $\overset{(-)}{\nu}_\mu$ disappearance channel as well as the result of the combined fit, again based on [3]. The experimental data contributing to this analysis including the respective references to the original publications are given in table 4.5.

Out of these experiments, Super-Kamiokande, DeepCore and IceCube measure atmospheric neutrinos. These are for the most part muon (anti)neutrinos which are produced naturally in the atmosphere from cosmic radiation. Therefore the measurement comprises the whole solid angle. The two experiments Super-Kamiokande and DeepCore, which is a subdetector of IceCube, both measure low energy atmospheric neutrinos. The dataset of neutrinos measured in these experiments can be divided into two subsets, tagged “down-going” and “up-going”. The events measured in the “down-going” dataset correspond to neutrinos which were produced in the atmosphere above the horizon and traveled downwards to the respective experiment. For this dataset, the survival probability for muon (anti)neutrinos can be approximated by

$$P^{\mathrm{D}}_{\overset{(-)}{\mu}\overset{(-)}{\mu}} = \left(1-|U_{\mu4}|^2\right)^2 + |U_{\mu4}|^4, \tag{4.15}$$

which follows from the SBL approximation eq. (4.2) in the limit $\Delta m^2_{14}L/4E \gg 1$, such that oscillations are averaged out. By contrast the events measured in the “up-going” dataset correspond to neutrinos which were produced in the atmosphere beneath the horizon and traveled upwards through the body of the earth to the respective experiment. Therefore these neutrinos travel long distances, such that the SBL approximation eq. (4.2) or eq. (4.15) do not hold. Furthermore, the up-going neutrinos encounter finite temperatures and densities (FTDs) along their trajectory through the body of the earth. As explained in section 2.4, coherent forward scattering off background particles at FTD results in an effective potential V_{eff} which modifies the dispersion relation. However, a change in the dispersion relation of one state relative to another state impacts the interference between these states and hence the oscillation probability changes. As discussed in section 2.4, this scenario is fulfilled for the SM neutrinos traversing ordinary matter, because of an additional contribution to V_{eff} for electron neutrinos due to CC-mediated scattering off electrons. The contribution to V_{eff}

---

[7] c.f. footnote 4.

Experiment	References	Data points	Comments
IceCube	[102, 103, 104]	189	MSW resonance in high-energy atmospheric $\bar{\nu}_\mu$
CDHS	[105]	15	accelerator ν_μ
MiniBooNE	[106, 107, 108]	15 + 42	accelerator ν_μ and $\bar{\nu}_\mu$ (+SciBooNE data)
Super-Kamiokande	[109, 110]	70	low-energy atmospheric neutrinos
DeepCore	[111, 112]	64	low-energy atmospheric neutrinos
NOνA	[113]	1	accelerator ν_μ, NC data
MINOS/MINOS+	[114]	108	accelerator ν_μ, CC & NC event spectra

Table 4.5: Experimental data sets included in the $\overset{(-)}{\nu}_\mu$ disappearance analysis. The total number of data points in this channel is 504.
Table and caption taken from [3] (order of columns and wording of table/caption slightly modified).
Note added by the author: technical details on the implementation of the CDHS and MiniBooNE can be found in the appendix of [2]. Furthermore, in the same place, the formalism applied in the analysis of the atmospheric experiments Super-Kamiokande and DeepCore is explained. The appendix of [3] contains technical details on the implementation of the IceCube experiment used to produce the results in section 4.5, as well as details on an independent technical approach used to cross-check these results.

due to scattering off nuclei as well as NC-mediated scattering off electrons introduces a collective offset in the dispersion relation of all the SM neutrinos. This contribution, given by [3]

$$V_{\text{eff}}^s \sim 1.9 \times 10^{-14}\,\text{eV} \times [\rho_\oplus/(\text{g/cm}^3)], \tag{4.16}$$

with $\rho_\oplus$ the mass density of the earth, results in an unobservable phase in the standard scenario. However, sterile neutrinos do not interact and hence for them V_{eff}^s is zero. Thus in the 3 + 1 framework, the contribution given in eq. (4.16) leads to a relative shift in the dispersion relation of the active neutrinos compared to the sterile neutrino. Consequently by analogy with the standard MSW effect discussed in section 2.4, an additional matter effect due to V_{eff}^s modifies the oscillation probability compared to the vacuum case. Inserting V_{eff}^s

in the dispersion relation eq. (2.48) such that $b \sim 1.9 \times 10^{-14}\,\mathrm{eV} \times [\rho_{\oplus}/(\mathrm{g/cm}^3)]$, it becomes obvious that for sterile neutrinos with masses $m_s \sim 1\,\mathrm{eV}$ the matter effect is negligible for the average energies $E_\nu \sim \mathcal{O}(10 - 100\,\mathrm{GeV})$ measured in the low-energy atmospheric experiments Super-Kamiokande and DeepCore. Using this approximation in combination with the limit $\Delta m^2_{41} \to \infty$ [91], in [115] the lower bound

$$P^{\mathrm{U}}_{\overset{(-)}{\mu}\overset{(-)}{\mu}} \geq |U_{\mu 4}|^4 \tag{4.17}$$

was derived for the survival probability of up-going muon (anti)neutrinos. The evaluation of the ratio between up-going and down-going atmospheric neutrinos effectively probes the ratio between the probabilities eq. (4.15) and eq. (4.17). The precise measurement of this ratio thus tightly constrains $|U_{\mu 4}|$.

IceCube is sensitive to atmospheric neutrinos of high energies $E_\nu \sim \mathcal{O}(0.5 - 50\,\mathrm{TeV})$. For these energies, the term $m^2_4/2E$ is of the same order as V^s_{eff} in the dispersion relation and hence a significant impact on the oscillation probability is expected, as has been noted in [116]. To assess qualitatively the matter effect due to V^s_{eff}, the approximation $m^2_i \to 0$ with $i \in \{1, 2, 3\}$ can be employed, which is legitimate for $L/2E \simeq \mathcal{O}(1)$ which holds for the very long baselines and high energies at IceCube. The survival probability in matter in the $3 + 1$ framework, by analogy with eq. (2.59) is

$$\begin{aligned} P_{\overset{(-)}{\mu}\overset{(-)}{\mu}}(L) =& \left| \exp\left[-i \left(U \mathrm{diag}\left(0, 0, 0, \frac{m^2_4}{2E}\right) U^\dagger \pm \mathrm{diag}(V^e_{\mathrm{eff}}, 0, 0, V^s_{\mathrm{eff}}) \right) L \right]_{\mu,\mu} \right|^2 \\ =& \left| \exp\left[-i \left(\left(\frac{m^2_4}{2E}\right) \mathbf{U}\mathbf{U}^T \pm \mathrm{diag}(V^e_{\mathrm{eff}}, 0, 0, V^s_{\mathrm{eff}}) \right) L \right]_{\mu,\mu} \right|^2 , \end{aligned} \tag{4.18}$$

with the definition $\mathbf{U}^T \equiv (U_{e4}, U_{\mu 4}, U_{\tau 4}, U_{s4})$ [117]. Approximating furthermore the mixing parameter $U_{e4} \ll 1$ by zero renders the matrix in the exponent of eq. (4.18) block diagonal, such that for calculating $P_{\overset{(-)}{\mu}\overset{(-)}{\mu}}$ only the 3×3 submatrix $((m^2_4/2E)\mathbf{U}^{(3)}\mathbf{U}^{(3)\,T} \pm \mathrm{diag}(0, 0, V^s_{\mathrm{eff}}))$ with $\mathbf{U}^{(3)T} \equiv (U_{\mu 4}, U_{\tau 4}, U_{s4})$ is relevant. As derived in [117], the strongest bound on $U_{\mu 4}$ can be established by setting $\theta_{\tau 4}$ to zero. In that particular case, the survival probability in matter is given by the effective two-flavor probability

$$P^{2\nu}_{\overset{(-)}{\mu}\overset{(-)}{\mu}} = 1 - \sin^2(2\theta_{\mathrm{eff}}) \sin^2\left(\frac{\Delta m^2_{\mathrm{eff}} L}{4E}\right), \tag{4.19}$$

with $\Delta m^2_{\mathrm{eff}}$ defined by analogy with eq. (2.63) and using $\Delta m^2 = \Delta m^2_{41}$ and $V_{\mathrm{eff}} = V^s_{\mathrm{eff}}$ as well as $\sin^2(2\theta_{\mathrm{eff}})$ defined by analogy with eq. (2.60), using $\sin^2(2\theta_0) = \sin^2(2\theta_{24})$. Considering in particular the expression eq. (2.60), which determines the amplitude in the limit where the two-flavor approximation eq. (4.19) holds, it follows that the disappearance probability in a certain range of energy can get enhanced for negative V^s_{eff}, which applies for antineutrinos, assuming $\Delta m^2_{41} > 0$. In principle the opposite case, $\Delta m^2_{41} < 0$, would also be possible, and it would not alter the vacuum oscillation phenomenology discussed previously. However that mass ordering, implying more heavy neutrino states, is in strong tension with data from cosmology, which set an upper bound on the sum of the neutrino masses. Therefore in this work only the possibility $\Delta m^2_{41} > 0$ is considered. In the case of neutrinos traversing matter at FTD, V^s_{eff} is positive and hence the disappearance amplitude is reduced for neutrinos.

For antineutrinos crossing the inner mantle of the earth, assuming parameter values $\Delta m^2_{41} \sim 1\,\text{eV}^2$ and $\sin^2 2\theta_{14} \sim 0.04$, roughly compatible with the $\overset{(-)}{\nu}_e$ disappearance and $\overset{(-)}{\nu}_e$ appearance channels discussed above, the resonance condition eq. (2.64) implies that the disappearance probability is maximal for neutrinos with energies around the resonance energy $E_{\text{res}} \simeq 5.3\,\text{TeV} \times (5\text{g/cm}^2/\rho_\oplus)$ $(\Delta m^2_{41}/1\,\text{eV}^2)$ [3]. This energy is well within the sensitive region of the IceCube detector. However, the detector cannot distinguish between neutrino and antineutrino events. Furthermore the detection cross section is about three times higher for neutrinos than for antineutrinos. Therefore the effect of the resonant enhancement of the disappearance probability of the antineutrinos is washed out by a large background of neutrinos. The width of the resonance, which can be estimated at [3]

$$\Delta E_{\text{res}} \simeq \frac{\Delta m^2_{41} \sin^2 2\theta_{24}}{2V^s_{\text{eff}}}, \tag{4.20}$$

is narrow for small values of $\sin^2 2\theta_{24}$. This means that only antineutrinos from a minor fraction of the atmospheric spectrum feature a resonantly enhanced disappearance probability, such that the impact on the event rate further decreases. Due to the form of the resonance given in eq. (4.20), the IceCube detector is furthermore sensitive only to a limited range of values for Δm^2_{41}. This is because for larger values of Δm^2_{41}, the resonance moves to high energies, for which the flux of atmospheric neutrinos is low, thus the impact of the resonance decreases significantly. For small values of Δm^2_{41}, the resonance width becomes very narrow, and the effect on the event rate again reduces. For even lower values of Δm^2_{41}, the resonance energy shifts below the threshold of the detector. These considerations further point to the importance of the detector systematics, as for example the potential to detect narrow dips in the neutrino flux depends crucially on the detector. In the appendix of [3] details are given on the implementation[8] of the IceCube results used in the analysis below, including the modeling of systematics.

---

[8] The implementation of the IceCube analysis underlying the results presented in this thesis

As mentioned above, the discussion so far was restricted to the case $U_{\tau 4} = 0$. When accounting for the possibility $U_{\tau 4} > 0$, the survival probability by analogy with eq. (2.59) takes the form

$$P_{\overset{(-)}{\mu}\overset{(-)}{\mu}}(L) = \sum_{i,k} |U_{\mathrm{eff},\mu i}|^2 |U_{\mathrm{eff},\mu k}|^2 \exp\left[\frac{-i\Delta m^2_{\mathrm{eff},ik} L}{2E}\right], \tag{4.21}$$

where the effective mixing matrix now depends on the two parameters θ_{24} and θ_{34}, as well as the complex phase δ_{24}. Furthermore, the probability given in eq. (4.21) now depends on two independent effective mass-squared parameters, given by [117]

$$m^2_{\mathrm{eff},1/2} = \frac{\Delta m^2_{41}}{2}\left(1 + \frac{2EV^s_{\mathrm{eff}}}{\Delta m^2_{41}} \pm \sqrt{\left(1 + \frac{2EV^s_{\mathrm{eff}}}{\Delta m^2_{41}}\right)^2 - 4\left(U^2_{\tau 4} + U^2_{\mu 4}\right)\frac{2EV^s_{\mathrm{eff}}}{\Delta m^2_{41}}}\right). \tag{4.22}$$

Hence the survival probability eq. (4.21) in the case of $U_{\tau 4} > 0$ is a superposition of the oscillations due to the modes corresponding to the effective mass parameters given in eq. (4.22). As shown explicitly in [117], the effect of $U_{\tau 4} > 0$ compared to the two-flavor probability eq. (4.19) is on the one hand that the resonance peak is reduced, and hence the potential signature is weakened. Yet on the other hand, the width of the resonance enlarges and the reduction of the survival probability due to the tails of the resonance becomes significant. The authors of [117] argue that the latter effect dominates, and hence the bound on $U_{\mu 4}$ is the stronger the smaller $U_{\tau 4}$ is. It is furthermore shown in [117] that the impact of the complex phase δ_{24} on the detection probability is correlated with $U_{\tau 4}$, but subleading with respect to its effect. As in the case of $U_{\tau 4}$, the bound on $U_{\mu 4}$ is the stronger the smaller the complex phase is.

For the sake of clarity in the above discussion of the atmospheric experiments the approximation $\Delta m^2_{4i} L/2E \gg \Delta m^2_{ji} L/2E \approx 0$ was made. Likewise, the fraction of electron (anti)neutrinos in the atmospheric flux was neglected. In that limit, the atmospheric experiments are sensitive to $U_{\mu 4}$ and Δm^2_{41}, as well as to $U_{\tau 4}$ and δ_{24} in the case of IceCube, due to matter effects. However, these approximations are not always justified. For example for neutrinos originating from near the horizon, the baseline is long enough such that oscillations due to $\Delta m^2_{31} \approx \Delta m^2_{32}$ are significant. Therefore atmospheric experiments are in addition sensitive to these mass-squared differences as well as to θ_{23}. Furthermore, taking into account an additional mass-squared parameter another com-

---

was provided by the author. Ivan Martinez-Soler contributed a second, independent implementation used to cross-check and validate the author's implementation. In particular, the comparison of both implementations allows to assess the impact of different approaches to the systematics of the IceCube experiment.

plex phase emerges in the expression for the survival probability in matter. In addition, the electron (anti)neutrinos in the atmospheric flux potentially contribute to the signal in the muon (anti)neutrino channel through oscillations $P_{e\mu}/P_{\bar{e}\bar{\mu}}$ as well as through misidentified detections of electron (anti)neutrinos. This effect is not very important for IceCube, since the atmospheric electron (anti)neutrino flux is very low at the high energies measured at IceCube. Moreover, oscillations into muon (anti)neutrinos are suppressed due to matter effects [117]. However, the electron (anti)neutrino flux does impact the results of Super-Kamiokande and DeepCore. In the analysis of the ratio between down-going and up-going (anti)neutrinos, the lower bound on up-going (anti)neutrinos, eq. (4.17), still holds, while for the down-going (anti)neutrinos, the events correlated with the electron (anti)neutrino flux need to be accounted for [115]. Therefore the low-energy atmospheric experiments are in particular also sensitive to U_{e4}.

The remaining experiments in table 4.5, CDHS, MiniBooNE, NOνA and MINOS/MINOS+, utilize a $\overset{(-)}{\nu}_\mu$ source originating from the decay of mesons. The technology used to produce these mesons from a high-energy proton beam is also used by several experiments investigating the $\overset{(-)}{\nu}_e$ appearance channel and has been explained in greater detail in section 4.4 where these experiments are introduced. In particular the MiniBooNE collaboration measured both channels, the $\overset{(-)}{\nu}_\mu \to \overset{(-)}{\nu}_e$ as well as the $\overset{(-)}{\nu}_\mu \to \overset{(-)}{\nu}_\mu$ channel, within a single experimental setup, using the same (anti)neutrino source and detector. The primary detection principal is based on charged-current quasi-elastic (CCQE) scattering, producing a charged (anti)lepton of the same flavor as the (anti)neutrino. Since the flavor of the charged (anti)leptons is correlated with a characteristic signature in the photomultiplier tubes (PMTs) of the MiniBooNE detector, the experiment is sensitive to both channels independently. For the data taken within the $\overset{(-)}{\nu}_\mu \to \overset{(-)}{\nu}_\mu$ channel relevant for this section, two analyses have been performed by the MiniBooNE collaboration. First, the spectrum recorded by the MiniBooNE detector was tested for deviation of the *shape* expected from the standard three flavor theory [106, 108]. In the second approach, the results of MiniBooNE were combined with the results of the SciBooNE experiment, which was originally build to measure the cross sections of neutrino interactions with carbon and iron nuclei. Since SciBooNE was located upstream in the same neutrino beam as MiniBooNE, the sensitivity of their combination is comparable to an experiment consisting of a designated near and far detector. In particular, the joined SciBooNE and MiniBooNE dataset allowed for a combined *rate and shape* analysis [107].

The CDHS experiment consisted of two detectors exposed to a low-energy muon neutrino beam. Both detectors were located close to the neutrino source, such that the SBL limit of the oscillation probability, eq. (4.2), holds to very good approximation. Thus from the fit to the ratio between the spectra measured at the two detectors limits on the ν_μ disappearance probability in the presence of a sterile neutrino can be derived.

The two experiments MINOS and MINOS+ share the same setup consisting of a ND and a far detector (FD) at a distance of 735 km. The beam supplying the experiments with muon neutrinos is called Neutrinos at the Main Injector (NuMI) beam. It is produced at the site of Fermilab. In the MINOS configuration, the NuMI beam was peaked at $\sim 2\,\mathrm{GeV}$, which is close to the value of $\sim 1.6\,\mathrm{GeV}$ corresponding to the maximum disappearance probability in the three-flavor oscillation framework. By contrast, in the MINOS+ configuration the NuMI beam was peaked at $\sim 7\,\mathrm{GeV}$. Hence MINOS+ was tuned to be more sensitive to spectral distortions that might be caused by phenomena beyond the three-flavor oscillation paradigm [114]. In the detectors of MINOS/MINOS+, muon neutrinos can be identified by CC interactions. In addition, due to a distinct signature, a separate sample of NC events can be recorded in the detectors. These NC events correspond to interactions of active neutrinos of any flavor. Therefore this dataset probes effectively the probability that a muon neutrino does not convert into a sterile neutrino, in addition to the $\nu_\mu \to \nu_\mu$ probability probed by the CC dataset. The potential signature of oscillations involving a sterile neutrino depend on the value of Δm^2_{41}. In the range of low $\Delta m^2_{41} \sim 10^{-3} - 10^{-1}\,\mathrm{eV}^2$, oscillatory features are expected in the spectrum measured by the FD, while the baseline to the ND is too short for oscillations to develop due to this small mass-squared difference. For slightly higher ranges of $0.1\,\mathrm{eV}^2 \lesssim \Delta m^2_{41} \lesssim 1\,\mathrm{eV}^2$, oscillations at LBLs average out thus resulting in an overall flux reduction at the FD, while still no effect would be expected at the ND. Still at higher ranges of $1\,\mathrm{eV}^2 \lesssim \Delta m^2_{41} \lesssim 100\,\mathrm{eV}^2$, the oscillatory features are now expected in the spectrum measured by the ND in addition to the reduced flux expected at the FD. Lastly, at very high ranges of $100\,\mathrm{eV}^2 \lesssim m^2_{41}$, oscillations due to this mass-squared difference are expected to average out at both baselines, leading to an overall flux reduction at the ND as well as the FD. In particular the last scenario cannot be explored by the usual approach of analyzing the ratio between the spectrum measured at the FD and the spectrum measured at the ND. This is because in this “Far-over-Near ratio” the overall flux reduction at both detectors would just cancel out. In order to capture the full range of the possible oscillations signatures discussed above, in [114] the MINOS/MINOS+ collaboration therefore provides a two-detector fit. The results discussed here are based on an implementation of the MINOS/MINOS+ analysis, following closely the approach presented in [114]. However, these results have been questioned in [118]. Yet as argued in [3], within the range of $\Delta m^2_{41} \lesssim 100\,\mathrm{eV}^2$ relevant here, the limit obtained from the MINOS/MINOS+ analysis is robust irrespective whether there is indeed a problem with the flux normalization or not. For details, c.f. [3], especially footnote (4).

The NOνA experiment consists of a ND and a FD at a distance of 810 km.

Both detectors are located in the same beamline as MINOS/MINOS+, however each detector is displaced by 14.6 mrad with respect to the beam axis. Therefore the energy distribution of the neutrinos is very narrow compared to the energy distribution in the center of the beam. While this design is very useful for background reduction, in the context of probing oscillation in the $3+1$ framework a narrow energy distribution implies that only a small range of the mass parameter $0.05\,\text{eV}^2 \lesssim \Delta m^2_{41} \lesssim 0.5\,\text{eV}^2$ is accessible. As in the case of MINOS/MINOS+ separate datasets are taken, which correspond to CC and NC events, respectively. For the analysis in the $\overset{(-)}{\nu}_\mu$ disappearance channel presented in this section, the results published by the NOνA collaboration in [113], based on a rate only evaluation of the NC data sample, were implemented.

The beam experiments presented above are differently sensitive to the parameters in the $3+1$ framework. For the SBL experiments MiniBooNE and CDHS the two-flavor limit in eq. (4.2) holds to good approximation, therefore in the main these experiments are only sensitive to the two parameters Δm^2_{41} and $|U_{\mu 4}|$. The LBL beam experiments MINOS/MINOS+ and NOνA are in addition sensitive to oscillations due the smaller mass-squared parameter Δm^2_{31} and to the mixing parameter θ_{23}. Since the NuMI beamline crosses the crust of the earth, the survival probability is impacted by matter effects. Therefore similar to IceCube, the LBL beam experiments are also sensitive to $U_{\tau 4}$, U_{e4} and the complex phases. In table 4.6, the parameters fitted in the following analysis of the global data in the $\overset{(-)}{\nu}_\mu$ disappearance channel are enlisted. The complex phases discussed above were also scanned in this analysis, however, as in the other channels, their impact was found to be of minor significance. Hence they are not counted as DOFs and consequently do not appear in table 4.6. All other parameters relevant for calculating the muon (anti)neutrino probability in the $3+1$ framework are fixed to their respective best fit values in what follows.

The result of the combined fit to the data recorded by the experiments discussed above is presented in fig. 4.5. The corresponding statistical parameters are given in the third row of table 4.7. The values quoted in table 4.7 were obtained from a full fit to the set of parameters given in table 4.6 supplemented by the complex phases. For the contours shown in fig. 4.5 U_{e4} is set to zero, in order to disentangle the impact of U_{e4} from the impact of $U_{\mu 4}$.

The vast accordance of the data in the $\overset{(-)}{\nu}_\mu$ disappearance channel with the predictions of the standard three-flavor model allows to set strong bounds on the parameters of the $3+1$ model. In fig. 4.5, these limits are shown in the plane spanned by the mixing parameter $|U_{\mu 4}|^2$ and the mass-squared parameter Δm^2_{41} [3]. Almost independent of Δm^2_{41}, a tight upper limit of $|U_{\mu 4}|^2 \lesssim 10^{-2}$ is established at 99%CL, represented by a black line in fig. 4.5. At high values of Δm^2_{41}, this limit is dominated by the results of the fit to the MiniBooNE $\overset{(-)}{\nu}_\mu$ disappearance and CDHS data, depicted by a dashed, dark green and solid light

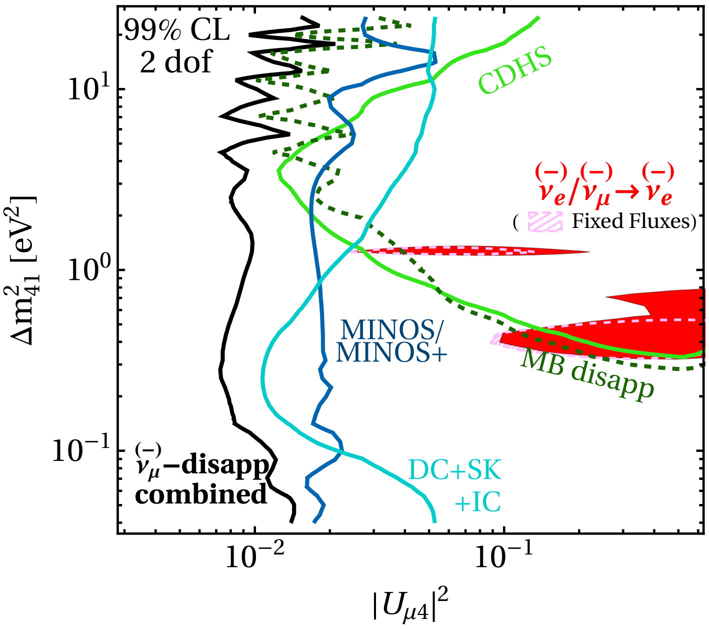

Figure 4.5: Constraints derived in the $\overset{(-)}{\nu}_\mu$ disappearance channel, projected onto the plane spanned by the mixing matrix element $|U_{\mu 4}|^2$ and the mass squared difference Δm^2_{41}. The black line shows the constraint from all datasets in the $\overset{(-)}{\nu}_\mu$ disappearance channel combined, with the corresponding experiments enlisted in table 4.5. Colored lines depict the constraint from subsets of this dataset. The limit from NOνA alone is not yet compatible and hence not shown separately in the plot. The NOνA data are, however, taken into account in the fit to the combined data in the $\overset{(-)}{\nu}_\mu$ disappearance channel. In the fit to the atmospheric neutrino data, represented by the cyan line, the parameters θ_{12}, θ_{13} and θ_{14} were kept fixed, while all other parameters, including phases, were scanned. See text for details on the choice of parameters and their relevance for counting DOFs. For comparison, the parameter regions favored by $\overset{(-)}{\nu}_e$ disappearance and $\overset{(-)}{\nu}_e$ appearance data including LSND DaR as well as DiF data are also shown. The red shaded regions represent these parameter spaces using the "flux-free" approach, while the pink-hatched regions represent these parameter spaces obtained in the "flux-fixed" approach.
Figure taken from [3].

green line, respectively. At lower values of Δm^2_{41}, the bound due to the atmospheric experiments dominates, represented by a cyan line. The limit on $|U_{\mu 4}|^2$ is especially strong at mass-squared values in the range $10^{-1}\,\mathrm{eV}^2 \lesssim \Delta m^2_{41} \lesssim 1\,\mathrm{eV}^2$. This is because that range of Δm^2_{41} corresponds to the parameter region where the IceCube detector would measure a resonantly enhanced antineutrino disappearance as explained above. The absence of this signature reported by the IceCube collaboration thus enforces a particularly tight upper limit on $|U_{\mu 4}|^2$. As described above, the strongest bound on $|U_{\mu 4}|^2$ is expected for $\theta_{34} = 0$. However, $U_{\tau 4}$ is already restricted by the atmospheric dataset itself [3], so that such an additional constrain is not necessary here. As discussed above, the sensitivity of IceCube rapidly decreases for higher or lower values of Δm^2_{41}. Therefore in these parameter regions, the limit from the atmospheric dataset is dominated by the low-energy experiments Super-Kamiokande and DeepCore. As expected from the discussion of these experiments above, the limit is to good approximation independent from Δm^2_{41}. The dark blue line shows the strong limit from MINOS/MINOS+, which is rather uniform across the range of the analyzed Δm^2_{41}. The result from NOνA is not competitive with the other limits yet due to low statistics and large systematics, therefore it does not appear in fig. 4.5. The NOνA data are, however, included in the global dataset resulting in the bound on $|U_{\mu 4}|^2$ shown in black. The numbers quoted in table 4.7 also refer to the analysis of the complete dataset, including the results from NOνA. The significance of the results from NOνA are expected to improve as its runtime increases.

For comparison, in red the result of a fit to the dataset consisting of the combination of all data outside the $\overset{(-)}{\nu}_\mu$ disappearance channel is shown. This dataset hence includes the anomalous results reported in the $\overset{(-)}{\nu}_e$ disappearance channel as well as the $\overset{(-)}{\nu}_e$ appearance channel. These anomalous measurements cause a preference of the fit to that combined dataset for the 3+1 framework over the standard three flavor framework. However, the corresponding parameter space is clearly excluded by the tight limits obtained from the analysis of the $\overset{(-)}{\nu}_\mu$ disappearance channel. The incompatibilities between the results obtained in the three different channels is discussed in detail in section 4.7, where also a combined analysis of the complete global data is presented.

4.6 Constraints on $|U_{\tau 4}|$

[9]In the previous sections, constrains on various parameters of the $3 + 1$ framework were reviewed. In particular constrains on the entries of the mixing matrix given in eq. (4.1) are possible, because these parameters are correlated with the

---

[9] c.f. footnote 4.

amplitude of potential oscillations in the $3+1$ framework. However, in vacuum, the amplitude of the oscillation probability, given in eqs. (2.27) and (2.29) only depends on the entries of the mixing matrix corresponding to the flavor of the initial neutrino and the detected neutrino, respectively. Thus within the $\overset{(-)}{\nu}_\mu$ and $\overset{(-)}{\nu}_e$ disappearance channels limits were set on U_{e4} and $U_{\mu 4}$ respectively, while within the $\overset{(-)}{\nu}_e$ appearance channel bounds on both matrix elements simultaneously were derived. However, $U_{\tau 4}$ cannot be constrained in the same way. On the one hand, no source of tau neutrinos exists[10], therefore for tau neutrino neither the survival probability nor the oscillation into a different flavor can be measured. On the other hand, tau neutrino appearance is highly challenging to measure. This is because the corresponding signature, the production of a tau particle in a CC interaction, has a very high energy threshold, due to the large mass of the tau. Hence, while tau neutrinos have been measured [119], the low statistics do not allow for constraining $U_{\tau 4}$.

Nevertheless, limits on $|U_{\tau 4}|$ can be derived indirectly. On the one hand, NC interactions are equally sensitive to all active neutrino flavors although it is not possible to determine the flavor of the detected neutrino on an event-by-event basis. Thus using NC data, only a combination of $|U_{\tau 4}|$ and the remaining mixing parameters can be constrained. NC events are measured in the solar neutrino experiment SNO, as described in section 4.3.2, as well as in the beam neutrino experiments MINOS/MINOS+ and NOνA as described in section 4.5. On the other hand, oscillation probabilities gain sensitivity to $|U_{\tau 4}|$ due to matter effects as explained in section 4.5. Therefore, the data from the atmospheric experiments IceCube, DeepCore and Super-Kamiokande can be additionally used to constrain $|U_{\tau 4}|$. However, as both methods are indirect measurements, the bounds on $|U_{\tau 4}|$ are in particular entangled with the other active-sterile mixing parameters U_{e4} and $U_{\mu 4}$. Therefore, $|U_{\tau 4}|$ is far less constrained than the other parameters, for which bounds can be derived directly in the $\overset{(-)}{\nu}_\mu$ and $\overset{(-)}{\nu}_e$ disappearance channel, respectively.

The result of the analysis of the NC data as well as the data sensitive to matter effects is shown in fig. 4.6 [3]. Each plot depicts the constrains on the parameter space spanned by $|U_{\mu 4}|^2$ and $|U_{\tau 4}|^2$ for a fixed value of the mass-squared parameter Δm^2_{41}, given in the legends in the left corner of the plots. Parameters which the respective experiments are not sensitive to were fixed to their best fit value. By contrast, all parameters which the respective experiments are sensitive to were scanned and marginalized over. A detailed discussion on the counting of relevant parameters can be found in the description of the experiments in section 4.3.2 for the solar data and section 4.5 for the remaining datasets. The contours in each plot are drawn with respect to the local minimum correspond-

---

[10] In the atmosphere and also in beam experiments, tau neutrinos are produced, however, their contribution to the total flux is negligible.

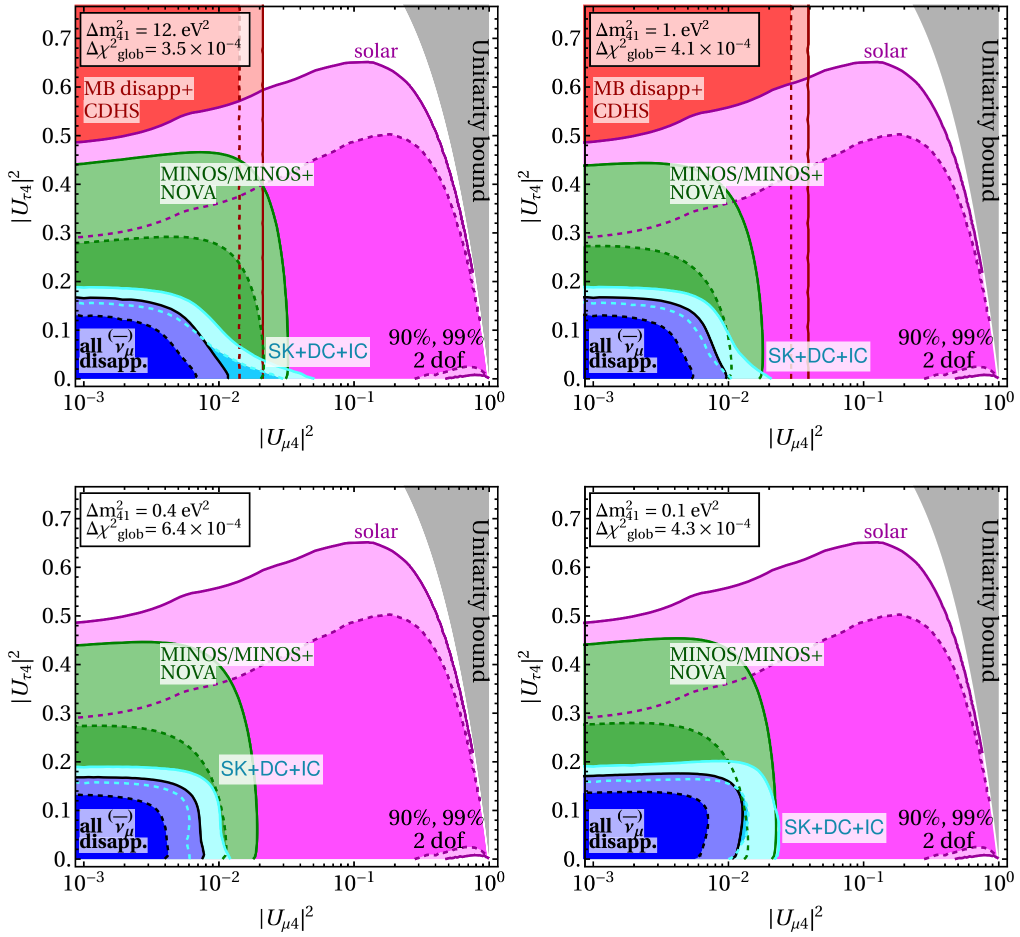

Figure 4.6: Constraints on the mixing of sterile neutrinos with muon and tau neutrinos, parameterized by the corresponding elements $|U_{\mu4}|$ and $|U_{\tau4}|$ of the leptonic mixing matrix. In each panel, Δm^2_{41} has been fixed to a different value, while Δm^2_{31}, θ_{23}, θ_{12} and θ_{14}, as well as complex phases have been profiled out in those experiments where they have a significant impact. Exclusion contours are drawn relative to the minimum χ^2 in each panel; the difference to the global minimum χ^2 is indicated in each plot. Grayed out areas show the parameter region incompatible with the unitarity of the leptonic mixing matrix.

Figure and caption taken from [3].

ing to the respective fixed value of Δm_{41}^2. For every plot, the difference of each local minimum to the global minimum is given in the respective legend of the plot. However, this difference is small for all the values of Δm_{41}^2 explored in fig. 4.6, because all individual BFP are close to zero mixing, and thus almost do not depend on Δm_{41}^2.

Contours are shown at 90% CL in dark shades and at 99% CL in lighter shades. The gray band covers the area excluded by the unitarity constrain $|U_{\tau 4}|^2 + |U_{\mu 4}|^2 \leq 1$. Solar data provide the weakest bound on $|U_{\tau 4}|^2$ for all four values of Δm_{41}^2 explored. By contrast, the strongest bound on $|U_{\tau 4}|^2$ is set by the atmospheric dataset. The limit from the LBL beam experiments MINOS/MINOS+ and NOνA on $|U_{\tau 4}|^2$ is somewhat weaker than that from the atmospheric experiments for all four panels in fig. 4.6. However, the respective limits on $|U_{\mu 4}|^2$ are slightly stronger, except in the last plot for the smallest value of $\Delta m_{41}^2 = 0.1\,\text{eV}^2$, which is near the resonance region of IceCube, as explained in section 4.5. The SBL beam experiments CDHS and MiniBooNE are not sensitive to $|U_{\tau 4}|^2$, since for these experiments to very good approximation eq. (4.2) holds, which only depends on $|U_{\mu 4}|^2$. Nevertheless, the results from these experiments could potentially add valuable information, since they provide the strongest limit on $|U_{\mu 4}|^2$ for high $\Delta m_{41}^2 \gtrsim 1\,\text{eV}^2$, as discussed in section 4.5. These limits are shown in red in the first two panels of fig. 4.6. However, since the preferred parameter spaces of the other experiments measuring $\overset{(-)}{\nu}_\mu$ disappearance are rather flat in $|U_{\tau 4}|^2$, the impact of the SBL beam experiments on the combined limit is rather low. The result of this combined fit is represented by the blue shaded area, which features no strong dependence on Δm_{41}^2. Indeed, marginalizing over the mass-squared parameter sets the limit

$$|U_{\tau 4}|^2 < 0.13\,(0.17) \quad \text{at} \quad 90\%\,(99\%)\,\text{CL}. \tag{4.23}$$

on $|U_{\tau 4}|^2$.

4.7 Global fit in the $3+1$ framework

[11]In the previous sections of this chapter, the various neutrino oscillation experiments were categorized by channel. The datasets in each channel were analyzed separately. In each channel, the data can be fitted rather consistently within the $3+1$ framework, which can be seen for example from the relatively high GOF values given in table 4.7. An exception is the relatively low value for the $\overset{(-)}{\nu}_e$ appearance channel, which can be understood from the arguments given in section 4.4. However, the individual channels are not independent from one another. While according to eqs. (2.27) and (2.29) the vacuum disappearance

---

[11] c.f. footnote 4.

probability $P_{\alpha\alpha}/P_{\bar{\alpha}\bar{\alpha}}$ in a specific channel indeed depends only on the entries $U_{\alpha i}$ with $i \in \{1, 2, 3, 4\}$, matter effects introduce a dependence on further elements of the mixing matrix, as discussed in general in section 2.4 and for the specific case of IceCube in section 4.5. Furthermore, the datasets labeled "$\overset{(-)}{\nu}_e$ disappearance" and "$\overset{(-)}{\nu}_\mu$ disappearance" above, actually each contain in addition to the respective $\overset{(-)}{\nu}_\alpha \to \overset{(-)}{\nu}_\alpha$ data also NC data, measuring $\overset{(-)}{\nu}_\alpha \to \overset{(-)}{\nu}_i$ with $i \in \{1, 2, 3\}$. This implies that the datasets assigned to the individual channels are to some extent sensitive to more mixing parameters than the respective vacuum oscillation probabilities imply. This is the reason why atmospheric data can constrain U_{e4} as discussed in section 4.3.2, or why constrains on $U_{\tau 4}$ are possible as discussed in section 4.6.

More importantly, the vacuum appearance probability $P_{\alpha\beta}/P_{\bar{\alpha}\bar{\beta}}$ depends on two rows $U_{\alpha i}$ and $U_{\beta i}$ of the mixing matrix simultaneously. This implies a strong interdependency between the results from the $\overset{(-)}{\nu}_\alpha$ and $\overset{(-)}{\nu}_\beta$ disappearance channels on the one hand and the results from the $\overset{(-)}{\nu}_\alpha \to \overset{(-)}{\nu}_\beta$ appearance channel on the other hand. In the limit where the SBL approximation eq. (4.2) holds, and thus the respective probabilities depend solely on $U_{\alpha 4}$ and $U_{\beta 4}$, the correlation between the channels becomes particularly evident. Therefore, LSND and MiniBooNE $\overset{(-)}{\nu}_e$ appearance data are especially critical. On the one hand they are SBL experiments and hence the corresponding oscillation probability to good approximation depends only on the product $|U_{\alpha 4}||U_{\beta 4}|$. On the other hand they feature anomalous results which exhibit a preference for this product in the effective mixing parameter $\sin^2 2\theta_{\mu e} \equiv 4|U_{\alpha 4}|^2|U_{\beta 4}|^2 > 0$ defined in eq. (4.13) to be non-zero. As discussed in section 4.3.2, the data in the $\overset{(-)}{\nu}_e$ disappearance channel prefer a small, yet non-zero value for $|U_{e4}|$, given in table 4.7. But for all datasets to be compatible in the 3 + 1 framework, also $|U_{\mu 4}|$ would need to be non-zero and not too small, such that the product $4|U_{\alpha 4}|^2|U_{\beta 4}|^2$ would be in accordance with the parameter region preferred by LSND and MiniBooNE. However, no evidence of $|U_{\mu 4}|$ being greater than zero was found in the analysis of the $\overset{(-)}{\nu}_\mu$ disappearance channel in section 4.5 and hence the value of $|U_{\mu 4}|$ is constrained to be very low. From these conflicting results emerges a strong and long withstanding tension within the global data in the 3 + 1 framework [120]. This tension could already be observed in fig. 4.5 where the strong exclusion limits from the experiments measuring the $\overset{(-)}{\nu}_\mu$ disappearance channel were confronted with the parameter region preferred by the combined results from the $\overset{(-)}{\nu}_e$ disappearance and $\overset{(-)}{\nu}_e$ appearance channel. Here, based on [3], a detailed analysis of the global data in the full 3 + 1 framework is presented, taking into account all the experiments discussed previously and summarized in tables 4.2, 4.4 and 4.5.

The result of the global analysis is given in table 4.7, which summarizes the

Data set	Reference	Data points	Relevant parameters
$\overset{(-)}{\nu}_e$ disappearance	Table 4.2	594	Δm^2_{31}, Δm^2_{41}, θ_{12}, θ_{14}, θ_{24}, θ_{34}
$\overset{(-)}{\nu}_\mu \to \overset{(-)}{\nu}_e$ appearance (w/o LSND DiF)	Table 4.4	69	Δm^2_{41}, $\lvert U_{e4}U_{\mu 4}\rvert$
$\overset{(-)}{\nu}_\mu$ disappearance	Table 4.5	504	Δm^2_{31}, Δm^2_{41}, θ_{23}, θ_{14}, θ_{24}, θ_{34}
Total number of data points:		1167	

Table 4.6: Number of degrees of freedom and parameters relevant to the counting of degrees of freedom for each data set. More details on the individual experiments are given in the corresponding tables. The number of degrees of freedom for the LSND decay-in-flight analysis is not available. Thus, in the sum of degrees of freedom for appearance and all datasets, the LSND decay-at-rest number is used.
Table and caption (slightly modified) taken from [3].
Note added by the author: In most fits, additional parameters were used, which were not counted as DOFs. Explanations on the choice of parameters and a detailed discussion on the impact of additional parameters is given in the respective sections 4.3.2, 4.4 and 4.5.

results in the individual channels discussed previously as well as the result of the combined fit. The global analysis was performed for fixed as well as for free reactor fluxes, for the reasons discussed in sections 4.3.1 and 4.3.2. Furthermore the two approaches on the LSND data discussed in section 4.4, tagged DiF and DaR, were used.

In table 4.7, for reference the GOF values are included. These are calculated on the basis of the counting of parameters provided in table 4.6. In addition to the parameters enlisted there, the flux normalization in the IceCube implementation as well as the normalization priors of the reactor fluxes from the two main fission isotopes in the “flux free” approach were counted as DOFs. However, the GOF values might not be a very reliable measure for the reasons explained in section 4.2. Therefore, in addition a PG analysis was performed, which serves as a basis for the following discussion. The corresponding test statistic χ^2_{PG} was evaluated for a comparison between the $\overset{(-)}{\nu}_e$ appearance dataset and the dataset containing all disappearance data, that is the $\overset{(-)}{\nu}_\mu$ disappearance channel and the $\overset{(-)}{\nu}_e$ disappearance channel combined:

$$\chi^2_{\text{PG}} = \Delta\chi^2_{\text{app}} + \Delta\chi^2_{\text{disapp}}. \tag{4.24}$$

Analysis	Δm_{41}^2 [eV^2]	$\lvert U_{e4}\rvert$	$\lvert U_{\mu 4}\rvert$	$\chi^2_{\rm min}$/DOF	GOF	$\chi^2_{\rm PG}$	PG
appearance (DaR)	0.573	$4\lvert U_{e4}\rvert^2\lvert U_{\mu 4}\rvert^2$ $= 6.97 \times 10^{-3}$		89.8/67	3.3%		
appearance (DiF)	0.559	$4\lvert U_{e4}\rvert^2\lvert U_{\mu 4}\rvert^2$ $= 6.31 \times 10^{-3}$		79.1/–			
$\overset{(-)}{\nu}_\mu$ disapp	2×10^{-3}	0.12	0.039	468.9/497	81%		
Reactor fluxes fixed at predicted value ± quoted uncertainties							
$\overset{(-)}{\nu}_e$ disapp	1.3	0.1	–	552.8/588	85%		
Global (DiF)	6.03	0.2	0.1	1127/–		25.7	2.6×10^{-6}
Global (DaR)	5.99	0.21	0.12	1141/1159	64%	28.9	5.3×10^{-7}
Reactor fluxes floating freely							
$\overset{(-)}{\nu}_e$ disapp	1.3	0.095	–	542.9/586	90%		
Global (DiF)	6.1	0.20	0.10	1121/–		29.6	3.7×10^{-7}
Global (DaR)	6.0	0.22	0.11	1134/1157	68%	32.1	1.1×10^{-7}

Table 4.7: Best fit values and statistical parameters obtained for the full, global dataset and various subsets. For each dataset, the χ^2 per DOF at the BFP as well as the corresponding GOF values are enlisted. The respective DOFs can be calculated counting the numbers of data points and the parameters fitted in the analyses of the individual datasets. These numbers are summarized in table 4.6. Furthermore, for the global fit, the results of the parameter PG test [44], reviewed in section 4.2, is indicated. As explained in section 4.4, the labels "DaR" and "DiF" refer to the respective subsets of data underlying the LSND analysis. As noted previously, the number of DOFs for the LSND DiF data is not available. Therefore, the corresponding GOF values are not listed for fits including this dataset.
Table taken from [3].

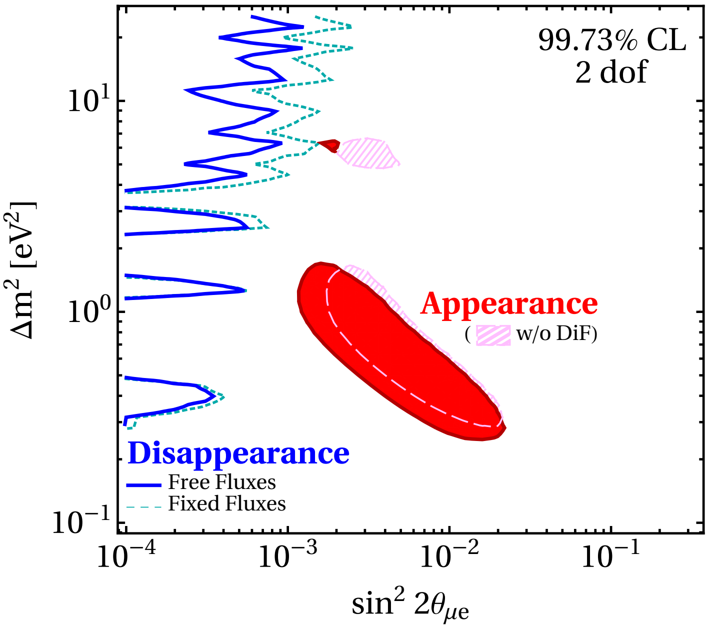

Figure 4.7: Appearance versus disappearance results in the plane spanned by the effective mixing angle $\sin^2 2\theta_{\mu e} \equiv 4|U_{e4}U_{\mu 4}|^2$ and the mass squared difference Δm^2_{41}. The blue curves show limits from the disappearance data sets using free reactor fluxes (solid) or fixed reactor fluxes (dashed), while the shaded contours are based on the appearance data sets using LSND DaR+DiF (red) and LSND DaR (pink hatched). All contours are at 99.73% CL for 2 DOF.
Figure and caption (wording slightly modified) taken from [3].

The particular choice used in eq. (4.24) is arbitrary. However, if the data were consistent in the $3+1$ framework, the PG test for any subdivision of the data should yield a reasonable p-value. Now the particular choice in eq. (4.24) results in very low PG values $\leq 10^{-5}$ as listed in table 4.7, which is enough to proof that the data actually exhibit a strong tension. Nevertheless, as a cross-check, in [3] the PG value was also evaluated for a different choice of subdividing the data into $\overset{(-)}{\nu}_\mu$ disappearance versus the combination of $\overset{(-)}{\nu}_e$ disappearance and $\overset{(-)}{\nu}_\mu$ appearance. The result was found to be slightly better, but still very small, thus supporting the results quoted in table 4.7.

Figure 4.7 constitutes the graphical counterpart of the PG analysis given in table 4.7. The global data is divided in the same two subsets "appearance" and "disappearance" used also in eq. (4.24) for the PG test. The result of the separate fit to the two datasets is projected on the plane spanned by Δm^2_{41} and the effective mixing parameter $\sin^2 2\theta_{\mu e}$, where again the flux-free and the flux-fixed scenario and the inclusion and exclusion of DaR data is considered. The resulting contours shown in fig. 4.7 reveal that at 99.73% CL, the parameter spaces preferred by the two subsets of data are in essence mutually exclusive.

Furthermore, it can be observed in fig. 4.7 that the distance between the contours corresponding to the appearance dataset and disappearance dataset, respectively, are smallest for the combination of including DiF data in the appearance data set and using the flux-fixed approach for the analysis of the disappearance data. This is because relatively large $|U_{e4}|$ values at high Δm^2_{41} are in conflict with the results from atmospheric data in the case of the flux-free scenario as can be seen in fig. 4.3, but not for the flux-fixed scenario. However, this combination of relatively large $|U_{e4}|$ and high Δm^2_{41} is preferred by both, the flux-free as well as by the flux-fixed scenario, as can be noted in fig. 4.2. Hence, on the one hand the disappearance dataset allows for slightly higher values of $|U_{e4}|$ at high Δm^2_{41} in the flux-fixed case. On the other hand, as fig. 4.4 reveals, the LSND analysis including DiF data results in a broadening of the preferred parameter space towards somewhat smaller values of the effective mixing parameter $\sin^2 2\theta_{\mu e}$ in the same range of relative high Δm^2_{41}. These observations are supported by the PG values given in table 4.7. However, even in the least constraining scenario, the appearance dataset and disappearance dataset are incompatible within the $3+1$ framework at the 4.7σ level [3].

While this result impressively demonstrates that the $3+1$ framework fails to explain the global neutrino oscillation data consistently, it is still worthwhile investigating the robustness of this prediction. As has been noted above, the results in the $\overset{(-)}{\nu}_e$ appearance channel at SBL, given in table 4.4, are especially critical. Therefore, if the results reported by one or more of these experiments proved erroneous, the conclusion about the $3+1$ framework might change. Thus, in conclusion of the global analysis, reviewing the approach in [3], the impact of various datasets is examined by excluding these one after another from the fit. The various scenarios taken into account are enlisted in table 4.8. Again the PG value, calculated for the subdivision of the respective data into appearance and disappearance datasets, is used as a basis for the discussion below. Furthermore, this analysis is restricted to the least constraining scenario represented by the flux-free approach for the reactor data and the inclusion of the DiF data for LSND.

The first block of table 4.8 lists the resulting values of the relevant statistical parameters when one of the datasets considered anomalous is removed. Out of these results, the only significant improvement of the PG value is achieved when LSND is removed. The remaining tension corresponding to a PG value of 1.6×10^{-3} is mainly driven by the anomalous MiniBooNE $\overset{(-)}{\nu}_e$ appearance results. Comparing this to the very low PG value, when by contrast MiniBooNE

Analysis	$\chi^2_{\text{min,global}}$	$\chi^2_{\text{min,app}}$	$\Delta\chi^2_{\text{app}}$	$\chi^2_{\text{min,disapp}}$	$\Delta\chi^2_{\text{disapp}}$	χ^2_{PG}/DOF	PG
Global	1120.9	79.1	11.9	1012.2	17.7	29.6/2	3.71×10^{-7}
Removing anomalous data sets							
w/o							
LSND	1099.2	86.8	12.8	1012.2	0.1	12.9/2	1.6×10^{-3}
MiniBooNE	1012.2	40.7	8.3	947.2	16.1	24.4/2	5.2×10^{-6}
reactors	925.1	79.1	12.2	833.8	8.1	20.3/2	3.8×10^{-5}
gallium	1116.0	79.1	13.8	1003.1	20.1	33.9/2	4.4×10^{-8}
Removing constraints							
w/o							
IceCube	920.8	79.1	11.9	812.4	17.5	29.4/2	4.2×10^{-7}
MINOS/ MINOS+	1052.1	79.1	15.6	948.6	8.94	24.5/2	4.7×10^{-6}
MiniBooNE disap.	1054.9	79.1	14.7	947.2	13.9	28.7/2	6.0×10^{-7}
CDHS	1104.8	79.1	11.9	997.5	16.3	28.2/2	7.5×10^{-7}
Removing classes of data							
$\overset{(-)}{\nu}_e$ disapp. vs $\overset{(-)}{\nu}_e$ app.	628.6	79.1	0.8	542.9	5.8	6.6/2	3.6×10^{-2}
$\overset{(-)}{\nu}_\mu$ disapp. vs $\overset{(-)}{\nu}_e$ app.	564.7	79.1	12.0	468.9	4.7	16.7/2	2.3×10^{-4}
$\overset{(-)}{\nu}_\mu$ disapp. + solar vs $\overset{(-)}{\nu}_e$ app.	884.4	79.1	13.9	781.7	9.7	23.6/2	7.4×10^{-6}

Table 4.8: Results of the PG test described in section 4.2, applied to appearance and disappearance data taken from various subsets of the global data. The first row presents the results from the global fit to the full dataset. The rows below indicate the results obtained in fits leaving out various datasets from both, individual experiments, as well as combinations of experiments. All datasets were analyzed using the “flux-free” approach introduced in section 4.3.1. The number of DOFs is not listed in this table, because all analyses but the one listed second include LSND DiF data, for which the number of data points is not available as explained in section 4.4. The columns 2–8 enlist the parameters $\chi^2_{\text{min,global}}$, $\chi^2_{\text{min,app}}$ and $\chi^2_{\text{min,disapp}}$, corresponding to the χ^2 function at the respective BFPs in the fit to all data, the appearance only data and the disappearance only data. Furthermore, the columns headed “$\Delta\chi^2_{\text{app}}$” and “$\Delta\chi^2_{\text{disapp}}$” indicate the difference between the χ^2 function evaluated at the global BFP and the respective BFPs obtained in a fit to the appearance and disappearance data only. Finally, the last two columns list the χ^2 per DOF resulting from the PG test computed according to eq. (4.3)), and the resulting p-value given by eq. (4.6).
Table taken from [2] (wording slightly modified).

is removed, allows to conclude that the tension between the appearance and disappearance data is driven by LSND rather than by the excess in the low energy bins reported by MiniBooNE. The PG value improves only slightly when leaving out reactor data, rendering the question of the cause of the reactor anomaly discussed in detail in section 4.3.1 less important within the $3+1$ framework. When the gallium data are removed, the PG value declines by almost a factor of ten. This can be understood from the analysis of the $\overset{(-)}{\nu}_e$ disappearance data depicted in fig. 4.3. While the reactor data prefer somewhat lower values of U_{e4}, the gallium data drive the preferred parameter space towards somewhat higher values of U_{e4}, and thus in the direction preferred by the appearance data, given that $U_{\mu 4}$ is very small. Thus, leaving out this pull towards higher U_{e4}, the tension between disappearance and appearance data increases and consequently the PG value declines.

The second block of table 4.8 lists the resulting values of the relevant statistical parameters when one of the datasets contributing to the strong bound on $U_{\mu 4}$ is removed. None of the these scenarios improves the PG value significantly, in accordance with fig. 4.5 which shows that the bound on $U_{\mu 4}$ does in essence not depend on a single experiment in the relevant parameter space. Only leaving out MINOS/MINOS+, which provides a rather constant strong limit across the parameter space, a slight improvement is observed.

Lastly the third block of table 4.8 lists the resulting values of the relevant statistical parameters when a whole set of experiments is removed. As discussed previously, the results from the datasets corresponding to the disappearance channels are relatively independent, because essentially separate rows of the mixing matrix are probed in each of these channels. The interdependency of the constraints on the parameters comes about through the appearance channels, which are sensitive to a combination of parameters from different rows of the mixing matrix. Therefore, a significant improvement of the PG value is expected when for example the set of parameters corresponding to a specific channel is removed. This can indeed be observed when the data from the experiments measuring the $\overset{(-)}{\nu}_\mu$ disappearance channel are neglected. On the other hand, leaving aside the data from the experiments measuring the $\overset{(-)}{\nu}_e$ disappearance channel improves the PG value only slightly. This is because some of the experiments in the $\overset{(-)}{\nu}_\mu$ disappearance channel still provide considerable constraints on U_{e4} due to matter effects and the evaluation of NC events, as discussed above. In particular, the combination of the data of the $\overset{(-)}{\nu}_\mu$ disappearance channel with solar data already causes incompatibilities in the data on a level comparable to the tension in the full dataset.

From the review presented in this chapter follows that a consistent interpretation of the global neutrino oscillation data the $3+1$ framework is excluded. In particular, it is not possible that all anomalies are due to oscillations within the $3+1$ framework, given that most of the results from the remaining experiments prove correct. If there was a reason to discard all results in the $\overset{(-)}{\nu}_\mu$ disappearance channel, the $3+1$ framework could be considered a viable option to explain the remaining data. However, at present there is no indication that any experiment should be excluded, let alone a whole set of experiments. The above conclusion is very robust and rather independent from the impact of any particular single dataset. An exception is LSND, which is the main cause of the preference for high values of the effective mixing parameter $\sin^2 2\theta_{\mu e}$ in the $\overset{(-)}{\nu}_e$ appearance channel, incompatible with the results from the remaining experiments. By contrast the conclusion does in particular not depend on the reactor experiments and the corresponding arguable flux predictions. A potential scenario rendering oscillations in the $3+1$ framework viable again would be if the anomalies observed by LSND and MiniBooNE in the $\overset{(-)}{\nu}_e$ appearance channel were resolved in terms of a different explanation. Then the remaining experiments including in particular the anomalous results from the reactor and radioactive source experiments in the $\overset{(-)}{\nu}_e$ disappearance channel could be fitted consistently in the $3+1$ framework, as can be seen for example in fig. 4.3. As argued in [3], these conclusions are expected to hold qualitatively for more complicated models including a higher number of sterile neutrinos.

Finally the validity of the conclusions drawn in this chapter are strongly correlated with the interpretation of cosmological data. As discussed in section 3.2, these data constrain in particular the number of neutrino-like species and their total mass. The bounds on these characteristic parameters are in very good agreement with the predictions for SM neutrinos in the ΛCDM model. However, in the $3+1$ model the prediction of the number of neutrino species and the sum of neutrino masses significantly differs from the SM prediction. This implies that the various constraints discussed in section 3.2 strongly disfavor the $3+1$ model, completely independent from the tensions discussed here. However, as described above, the $3+1$ framework remains a possible scenario to explain at least a subset of the oscillation data. Therefore, the next chapter discusses possible scenarios which might relax or refute the constrains from cosmology.

5 Sterile neutrinos with secret interactions

5.1 Basic principal

[1]The previous chapter introduced the $3 + 1$ framework as a well-motivated, minimal extension of the SM. In particular, this model features a light, sterile neutrino taking part in neutrino flavor oscillations parametrized by a mixing parameter of the order $\sim \mathcal{O}(0.1)$. However, including the $3 + 1$ framework in the thermal history of the early universe results in the production of thermally distributed sterile neutrinos due to the oscillations of SM neutrinos. Therefore this scenario implies the existence of a fourth neutrino-like species in the early universe. But as discussed in section 3.2.2, various cosmological probes strongly disfavor an additional neutrino-like particle. Furthermore, also the sum of the masses of neutrino-like particles is tightly bound by cosmological observables. In particular, even a single neutrino-like particle species with a mass of $\sim 1\,\mathrm{eV}$, as preferred by the anomalous oscillation experiments, is already in strong tension with the bounds from cosmology reviewed in section 3.2.4.

Irrespective of the tensions discussed in chapter 4, these bounds from cosmological data conflict with the hints for sterile neutrinos measured by earthbound oscillation experiments. Yet, very importantly, this statement depends on the assumption that the mixing angles stay constant over the thermal evolution of the universe. Recalling the discussion of matter effects in section 2.4, it becomes clear that this condition does not need to be fulfilled. Whenever there is an effective potential affecting one flavor but not a second, the mixing angle between the two flavors is changed compared to the vacuum mixing angle due to the Mikheyev-Smirnov-Wolfenstein (MSW) effect. In particular, if this effective potential was temperature-dependent, the mixing angle between active and sterile flavors could be very small at high temperatures. If the initial abundance of sterile neutrinos is negligible, they would not be produced in the early universe, assuming that they are produced predominantly by oscillations or interactions proportional to the mixing angle. Consequently sterile neutrinos

---

[1] The results presented in this chapter, chapter 5, are based on [4]. The author contributed to this publication by deriving numerically the temperature interval used in the multi-flavor evolution described in section 5.2. Furthermore, in figs. 5.2 and 5.5, the author graphically processed parts of the results.

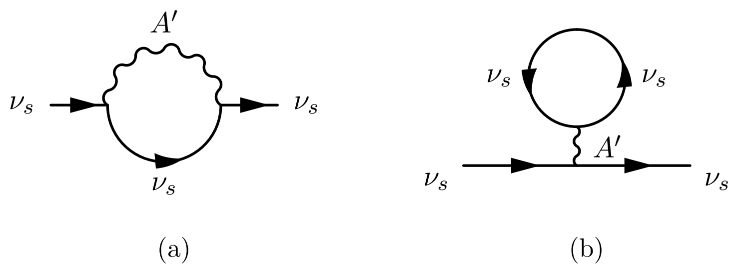

Figure 5.1: Diagrams contributing to the self-energy of a sterile neutrino coupled to a new, heavy gauge boson A': bubble diagram (a) and tadpole diagram (b).

would be absent in the early universe and thus they could not leave any imprint on cosmological probes. On the other hand at low temperatures, the mixing angle could be larger, as it is required to explain the short baseline anomalies through active-sterile neutrino oscillations.

Indeed, such a temperature-dependent effective potential, proportional to the term given in eq. (2.43), exists due to the active neutrino self-interaction and interactions with background fermions as discussed in section 2.4. However, inserting this term for b in the dispersion relation eq. (2.48) reveals that it is already negligible when the temperature is still very high, $T \sim 10\,\mathrm{GeV}$. Therefore this SM potential cannot suppress oscillations efficiently enough, resulting in the bounds discussed in section 3.2. It seems therefore a logical step to mirror this mechanism in the sterile sector. In the basic scenario, by analogy to the active sector, an interaction between sterile neutrinos is mediated by a new $U(1)'$ gauge boson A' with a mass $M \lesssim 1\,\mathrm{MeV}$ [121]. For obvious reasons, A' is often dubbed "dark photon", the interaction is called "secret interaction" and can be expressed by the following interaction term [4]

$$\mathcal{L}_{\text{int}} = e_s \bar{\nu}_s \gamma^\mu P_L \nu_s A'_\mu, \tag{5.1}$$

where e_s is the $U(1)'$ coupling constant. P_L denotes the projection operator onto left-chiral fermion states, which can be expressed as $P_L = \frac{1}{2}(1-\gamma^5)$. Following the approach of [4], the mass of the gauge boson A' is introduced ad hoc, without specifying how the $U(1)$ symmetry gets broken and neglecting any potential additional DOFs associated with this breaking.

The secret interaction term eq. (5.1) gives rise to two types of processes: scattering between two sterile neutrinos mediated by the secret interaction, similar to Bhabha and Møller in the SM, as well as scattering between a sterile neutrino and a dark photon A' similar to Compton scattering in the SM. Considering a background of sterile neutrinos and dark photons of finite temperatures and densities (FTDs), by analogy to the discussion in section 2.4, these scattering processes due to the new interaction, given in eq. (5.1), induce corrections to the sterile neutrino self-energy Σ. These corrections can be calculated in the real-time formalism in thermal field theory, as mentioned in section 2.4. The corresponding diagrams depicted in fig. 5.1 are very similar to the diagrams presented in the discussion of the SM MSW effect in section 2.4. As derived there, due to the corrections to Σ at FTD, the expansion of the dispersion relation in the ultrarelativistic limit exhibits a shift in the energy of the respective particle compared to the vacuum case. This shift corresponds to the effective potential V_{eff}. It is related to Σ by eq. (2.56), where $b = -V_{\text{eff}}$. Similar calculation as in the SM case result in an analytical expression for V_{eff} in two limiting cases:

$$V_{\text{eff}} \simeq \begin{cases} -\dfrac{7\pi^2 e_s^2 E T_s^4}{45 M^4} & \text{for } T_s \ll M \\ +\dfrac{e_s^2 T_s^2}{8E} & \text{for } T_s \gg M \end{cases}, \tag{5.2}$$

where T_s is the common temperature of the sterile neutrino and the gauge boson A' and E is the energy of the sterile neutrino. Of course numerically, V_{eff} can be determined for all ranges of T_s and E. The low temperature limit in eq. (5.2) is exactly of the same form as the term quoted in eq. (2.43) for electron neutrinos scattering off a background of electrons, which motivated the introduction of the secret interaction eq. (5.1). However unlike the SM term, which is suppressed by the fourth power of the SM gauge boson mass $m_W^4 \simeq (80\,\text{GeV})^4$, in the case of the secret interaction the suppression goes only with the fourth power of the secret gauge boson mass $M \ll m_W$. Therefore the effective potential due to the secret interaction is significant at lower temperature potentially beyond SM neutrino decoupling and BBN, when the SM effective potential is already negligible. In the high temperature limit, the low-energy expansion eq. (2.38) is not valid anymore. Instead, the structure of V_{eff} corresponds to the massless limit of quantum electrodynamics (QED) [22]. In fig. 5.2, the absolute value of V_{eff} is plotted for two different combinations of the mass M of A' and the secret fine structure constant $\alpha_s \equiv e_s^2/(4\pi)$. From both, the analytical expressions in the limit of high and low T_s as well as the numerical evaluation of V_{eff} presented graphically in fig. 5.2, can be seen that the absolute value of effective potential is large for large values of T_s. On the other hand it approaches zero for temperatures near zero, which applies for neutrino oscillation experiments on earth.

From the discussion in section 4.7 followed the conclusion that one conceivable scenario is that the anomalies in the $\overset{(-)}{\nu}_e$ appearance channel are due to some unknown origin different from oscillations involving sterile neutrinos. By contrary, the remaining results could be explained in the $3+1$ framework. In particular, the anomalies in the $\overset{(-)}{\nu}_e$ disappearance channel could be accounted for by oscillations into sterile neutrinos. In that case, in the limit $\Delta m_{4i}^2 \gg \Delta m_{ji}^2 \to 0$ with

$i, j \in \{1, 2, 3\}$ the only relevant mixing parameter would be U_{e4}. This scenario is effectively described by a $1 + 1$ system consisting of one sterile neutrino ν_s mixing with one active neutrino ν_a. Then for the oscillation probability in matter, given by eq. (2.59), a two-flavor approximation is legitimate with the two-flavor mixing angle in matter being given by eq. (2.60) with $\theta_0 = \theta_{14}$. Clearly this angle becomes very small for large absolute values of V_{eff} and hence at high temperatures. Qualitatively, the effect does not change even when the sterile neutrino mixes with more than one active neutrino [4].

In this picture, sterile neutrinos might originate at very high temperatures $T \gg$ TeV, possibly due to some new interaction in the context of a grand unified theory (GUT). The corresponding abundance of sterile neutrinos at these high temperatures gives rise to high values of V_{eff}, which efficiently shuts off any interaction with SM neutrinos. Subsequently, the sterile neutrinos decouple at still very high temperatures $T \gg$ TeV. Hence, they are not affected by multiple reheating processes occurring in the beginning of the thermal history of the universe due to the annihilation of various particle species, as described in section 3.1. Therefore, the sterile neutrino temperature T_s after some time is significantly lower than the temperature T of the thermal bath. The exact ratio between T and T_s depends on the physics at very high temperatures, which is not explored here. Instead, the ratio $T_{\text{ini},s}/T_{\text{ini}}$ at an arbitrary reference temperature $T_{\text{ini}} = 1\,\text{TeV}$ is treated as an initial condition. In [4], the two different initial conditions $T_{\text{ini},s}/T_{\text{ini}} = 0.3$ and $T_{\text{ini},s}/T_{\text{ini}} = 1$ were considered.

Thus, with a small abundance of sterile neutrinos produced in the early universe which decouple at very early times, the thermal history proceeds very similar to the case of the ΛCDM described in section 3.1. Only at later times, when V_{eff} finally vanishes, oscillations between active and sterile neutrinos emerge. Although neutrinos have long decoupled at that time, N_{eff} then decreases slightly, because sterile neutrinos are nonrelativistic at temperature $T \sim 1\,\text{eV}$. Likewise, the sum of the neutrino masses increases. Nevertheless, taking only oscillations with mixing parameter $\mathcal{O}(0.1)$ into account, the effect is expected to be small and still compatible with the bounds from cosmology. As explained below, this simple picture, taking into account only oscillations, is not sufficient.

Already at this stage, however, a critical feature of the V_{eff} becomes apparent from the expressions given in eq. (5.2): the different sign of the two limiting cases describing V_{eff} in the low and high temperature limit implies that V_{eff} is exactly zero at one point even for a non-zero temperature $T \sim M$. Since the suppression of oscillations is only effective as long as

$$|V_{\text{eff}}| > \frac{\Delta m^2}{2E} \tag{5.3}$$

holds, this suppression is potentially interrupted, if V_{eff} crosses zero at high temperatures. This could result in a production of sterile neutrinos efficient enough to conflict with bounds from cosmology. Taking into account this critical feature as well as further effects which challenge the secret interaction scenario results in very tight constraints, as discussed in the following section.

5.2 Constraints on sterile neutrinos with secret interactions

The above discussion of the basic principal of the secret interaction scenario neglected a small but very important detail. As described above, as soon as the condition in eq. (5.3) ceases to hold, the mixing between active and sterile neutrinos is no longer suppressed. Consequently, neutrinos start oscillating, as stated above. But furthermore, also scattering events increase the sterile neutrino abundance as soon as the mixing parameter is no longer reduced due to the MSW effect. This can be understood from the interaction Lagrangian eq. (5.1) in the mass basis,

$$\mathcal{L}_{\text{int}} = \sum_{ij} e_s \bar{\nu}_i U_{si} \gamma^\mu P_L U^*_{sj} \nu_j A'_\mu, \tag{5.4}$$

which gives rise to the following processes in the $1+1$ framework,

$$\bar{\nu}_4 + \nu_1 \to \bar{\nu}_4 + \nu_4 \qquad \text{diagram (a)\&(b) in fig. 5.3} \tag{5.5}$$

$$\nu_4 + \nu_1 \to \nu_4 + \nu_4 \qquad \text{diagram (c)\&(d) in fig. 5.3,} \tag{5.6}$$

with the corresponding Feynman diagrams depicted in fig. 5.3. In addition, the respective CP-conjugate processes contribute equally. As long as the mixing parameter U_{s1} is small due to the MSW effect, the corresponding scattering processes eqs. (5.5) and (5.6) are suppressed. When V_{eff} approaches zero and the condition eq. (5.3) is no longer fulfilled, these processes become efficient. If this happens while SM scattering processes are not yet frozen-out, in addition to the processes described in eqs. (5.5) and (5.6), similar processes due to $W^\pm$ and Z induced scattering need to be accounted for. Furthermore, the scattering processes due to the secret interaction can encounter a resonance. If the energy of the neutrinos is high enough, the intermediate A' is produced on shell. This results in a resonance in the s-channel. In the t-channel, assuming A' to be relatively light, scattering is enhanced in the forward direction. Due to these two effects, the impact of incoherent scattering can be significant, although according to the discussion in section 2.4, coherent forward scattering was expected to dominate.

In combination with oscillations, the scattering processes described above lead to an effective production due to the Dodelson-Widrow mechanism [122], as noted for instance in [123]. This mechanism works as follows: active neutrinos

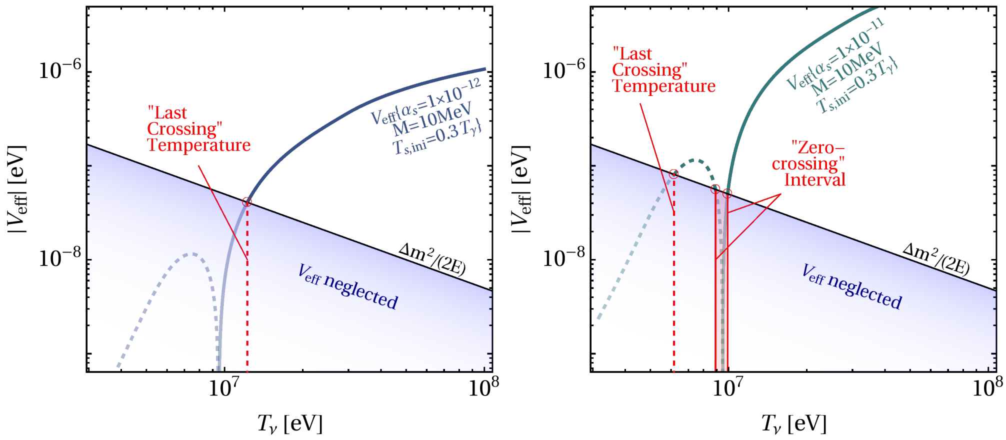

(a) (b)

Figure 5.2: Absolute value of the effective potential $V_{\rm eff}$ as a function of the (active) neutrino temperature T_ν, for two different choices of the mediator mass M and the secret fine structure constant $\alpha_s \equiv e_s^2/(4\pi)$. Positive (negative) values of $V_{\rm eff}$ are indicated by solid (dashed) lines. The vacuum oscillation frequency $\Delta m^2/(2E)$ is displayed as a black line. The temperatures at which $|V_{\rm eff}|$ and the vacuum oscillation frequency intersect are highlighted in red. The temperature of the last (left-most) intersection is denoted as "last crossing" temperature. For some choices of M and α_s, intersections between $|V_{\rm eff}|$ and $\Delta m^2/(2E)$ also occur around the temperature where $V_{\rm eff}$ changes sign, as can be observed in the right panel. In this case, the short time interval in which $|V_{\rm eff}| < \Delta m^2/(2E)$ is denoted "zero-crossing" interval. In the multi-flavor simulations, the sterile neutrino production is assumed to be zero when $|V_{\rm eff}| > \Delta m^2/(2E)$, and $V_{\rm eff}$ is set to zero, $V_{\rm eff} = 0$, whenever $|V_{\rm eff}| > \Delta m^2/(2E)$.
Figure and caption (slightly modified) taken from [4]

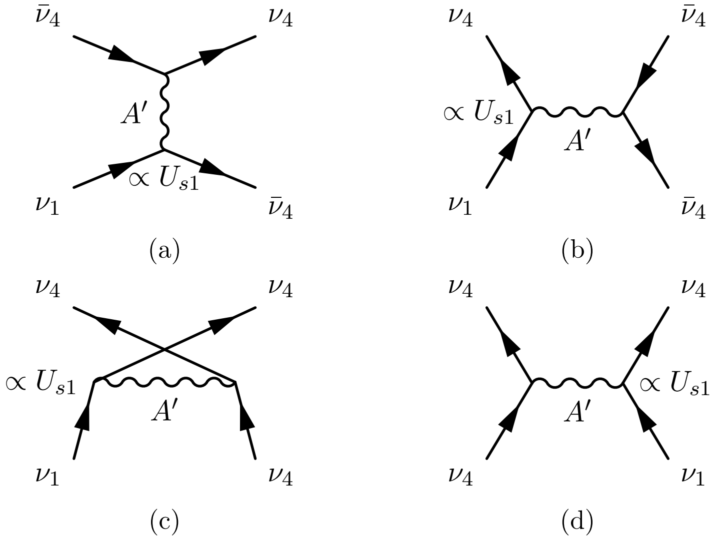

Figure 5.3: Scattering diagrams due to the secret interaction term given in eq. (5.1). Equivalent diagrams exist for the CP-conjugate processes. For illustration purposes, the dependence of the depicted processes on the mixing parameter U_{s1} is indicated. For high temperatures, $U_{s1} \to 0$, and hence the above scattering processes are suppressed. For low temperatures, $T \to 0$, $U_{s1} \sim 0.1$ in accordance with the RAAs and gallium anomalies discussed in section 4.7.

start oscillating and thus at some distance have to be considered as superpositions of flavor-eigenstates. Whenever a scattering event occurs, it virtually acts as a quantum-measurement, which projects the interacting neutrinos on flavor eigenstates with a probability according to the respective mixing parameter. In this manner, scattering produces an increasing abundance of sterile neutrinos. As long as this abundance is smaller than the abundance of active neutrinos, the back-reaction is less likely. This process continues until active and sterile neutrinos are in thermal equilibrium. By contrary, if the scattering rate is very high compared to the oscillation frequency, the Dodelson-Widrow mechanism does not work and sterile neutrino production is suppressed by the quantum Zeno effect. This effect occurs when a neutrino has no time to evolve into a superpositions of flavor-eigenstates by the time a quantum-measurement occurs in form of a scattering event, because its scattering length L^{scat} is short compared to the oscillation length L^{osc}. In this case, the neutrino remains a pure flavor-eigenstate and the measurement does not produce a projection on a different flavor.

Thus, if the neutrino temperature T_ν is below the quantum Zeno regime but above the temperature at which the scattering rate falls below the Hubble rate and becomes inefficient, sterile neutrinos *recouple* with the active neutrinos and thermal equilibrium is established between the two species. The authors of [124] showed that recoupling necessarily occurs at some temperature. This recoupling leads to conflicts between the basic sterile interactions scenario drafted in section 5.1 and constraints from cosmology, presented in section 3.2. Following [4], these constraints are reviewed below.

In detail, the constraints depend on the temperature at which the recoupling happens. If recoupling occurs before SM neutrinos freeze out from the thermal bath at a temperature $T \sim$ MeV, sterile neutrinos represent an additional relativistic DOF. This implies an increase of N_{eff} by approximately one unit, which is severely disfavored by cosmological probes as discussed in section 3.2.2. Furthermore, the sum of the neutrino masses in that case would be increased by the mass of the sterile neutrino, $m_4 \sim 1\,\text{eV}$, which is in tension with the bounds discussed in section 3.2.4. If recoupling between sterile and active neutrinos occurs after the active neutrinos have already decoupled from the other species, N_{eff} cannot change anymore, since the neutrinos constitute an isolated system. However, also in this case sterile neutrinos would be tightly constrained by the upper limit set by cosmological probes on the sum of neutrino masses. Nevertheless, as explained in section 3.2.4, the bounds on sum of the masses of neutrino-like particles depend in parts on its free-streaming length. If the secret interaction were so strong that sterile neutrinos could not free stream during structure formation, these bounds could be weakened. But since the secret interaction also affects active neutrinos due to mixing, this would imply that also the free-streaming length of active neutrinos would reduce. However, this is again in conflict with the results from cosmology presented in section 3.2.3 [125]. Lastly, as mentioned above, the transition between the two regimes where the high temperature limit and the low temperature limit of V_{eff} hold can occur at high temperatures. This implies that in addition to the production by the Dodelson-Widrow mechanism, a high abundance of sterile neutrinos could arise due to oscillations during the temperature interval near the zero crossing of V_{eff}.

The various constraints discussed above are caused by distinct cosmological probes and are hence qualitatively different. While it is arguable less important why the basic secret interaction scenario is disfavored at each parameter point, this information is potentially decisive when constructing extensions of the basic model. Based on the analysis presented in [4], the constraints on the secret interaction scenario are investigated using two different approaches below.

In the first approach, the recoupling temperature T_{rec} is determined directly by calculating the temperature corresponding to the scattering rate at which the production of sterile neutrino becomes efficient. According to the condition given in eq. (3.15), the minimal condition for a particle to be in thermal equilibrium is that its scattering rate is higher than the Hubble rate. Assuming quasi-instantaneous recoupling, T_{rec} can then be calculated as the temperature where

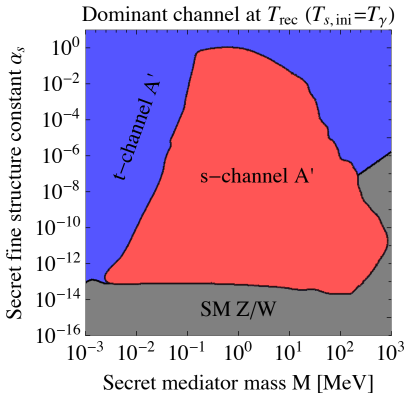

Figure 5.4: Dominant scattering channel for collisional ν_s production at T_{rec} as a function of M and α_s. Here, $m_s = 1$ eV, and $T_{\text{s,ini}} = T_\gamma$. The mixing angle suppression is common to all processes.
Figure and caption (slightly modified) taken from [4].

the scattering rate Γ_s becomes equal to the Hubble rate, [4]

$$H \overset{!}{=} \Gamma_s = c_{QZ}\left[\langle\sigma v\rangle_{ee\to 14}\,\frac{n_e^2}{n_\nu} + \langle\sigma v\rangle_{e1\to e4}\,n_e + \langle\sigma v\rangle_{11\to 14}\,n_\nu + \langle\sigma v\rangle_{14\to 44}\,n_s\right]. \tag{5.7}$$

In the above expression for Γ_s, the terms in angle brackets denote thermally averaged cross sections, where the subscripts $11 \to 14$ and $14 \to 44$ refer to the scattering processes described in eqs. (5.5) and (5.6), respectively. The subscripts $ee \to 14$ and $e1 \to e4$ refer to the corresponding SM scattering off electrons[2]. In fig. 5.4, the respective scattering process dominant at the time of recoupling is shown in the plane spanned by the secret fine structure constant α_s and the mediator mass M. As can be seen for example from eq. (5.4) for scattering mediated by A', the corresponding cross sections depend on the active-sterile mixing, and hence V_{eff}. In the currently discussed approach based on eq. (5.7), the absolute value of the effective potential, $|V_{\text{eff}}|$, is approximated by stitching together the absolute values of the two limiting cases given in eq. (5.2). Furthermore, in eq. (5.7), n_e, n_ν and n_s denote the electron, active and sterile neutrino number densities, which are normalized such that each term in eq. (5.7) gives the sterile neutrino production rate per active neutrino. Lastly, the prefactor c_{QZ} represents the function [4]

$$c_{QZ} = \frac{(L^{\text{scat}}/L^{\text{osc}})^2}{1 + (L^{\text{scat}}/L^{\text{osc}})^2}, \tag{5.8}$$

---

[2] For analytical expressions for all relevant cross sections, c.f. the appendix of [4].

which determines the suppression due to the quantum Zeno effect discussed above.

However, the approach presented above relies on several approximation. Therefore it is complemented by a second approach which numerically simulates the flavor evolution in a $2+1$ model, in which the sterile neutrino mixes with two active neutrinos. Determining T_{dec} in this approach would in principal require the simulation of the flavor evolution throughout the history of the universe. Yet, such a full simulation would be numerically highly challenging. Nevertheless, even without a full simulation, investigating the flavor evolution probes features of the decoupling process which cannot be assessed by the approach discussed above. In detail, these features are the precise dynamics of recoupling including the effect of oscillations, a full calculation of V_{eff} including the effect of a possible zero-crossing at high temperatures, a more accurate treatment of the quantum Zeno effect and lastly a more general $2+1$ framework, instead of the $1+1$ model adapted above.

The basic object in the flavor evolution approach is the density matrix $(\rho)_{\alpha\beta}$, or $(\bar{\rho})_{\alpha\beta}$ for antineutrinos [126], where $\alpha, \beta \in \{e, \mu, s\}$ in the case under consideration. The diagonal entries $\rho_{\alpha\alpha}$ $(\bar{\rho}_{\alpha\alpha})$ in the density matrix are the number densities of the (anti)neutrino species α, while the off-diagonal entries $\overset{(-)}{\rho}_{\alpha\beta}$ encode the mixing between the species α and β. The evolution of the density matrix $\overset{(-)}{\rho}$ is governed by the equation[3]

$$i\frac{\mathrm{d}\overset{(-)}{\rho}}{\mathrm{d}t} = [\Omega, \overset{(-)}{\rho}] + C[\overset{(-)}{\rho}], \tag{5.9}$$

where the t denotes the comoving observer's proper time. Ω corresponds to the Hamiltonian in flavor-space. Hence the first term encodes the flavor oscillations. The matrix C describes collisions due to interactions with the thermal background. In detail, C is given by

$$C[\overset{(-)}{\rho}] = C_{\mathrm{SM}}[\overset{(-)}{\rho}] + C_{A'}[\overset{(-)}{\rho}], \tag{5.10}$$

where C_{SM} corresponds to SM scattering processes and $C_{A'}$ to the scattering processes due to the secret interaction, given in eqs. (5.5) and (5.6).

As stated above, a full simulation of the flavor evolution is numerically highly challenging. Therefore, following [4], the evolution of $\overset{(-)}{\rho}$ is presented in the particular regime where V_{eff} becomes small compared to $\Delta m^2/2E$, such that eq. (5.3) does not hold anymore and hence active-sterile conversions are no longer suppressed. This is exactly the regime in which the multi-flavor evolution approach can provide details not accessible by the approach discussed above.

There are potentially two cases where the condition eq. (5.3) ceases to hold. On the one hand, as can be seen from the low temperature limit given in

---

[3] See [4] and references therein for details on the evolution equation.

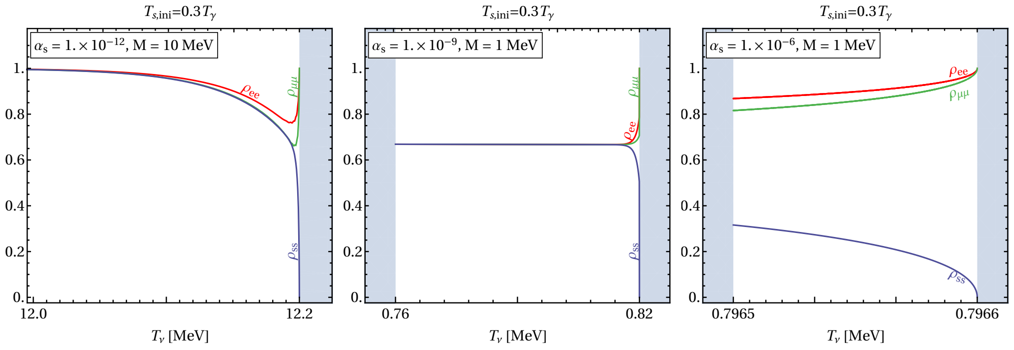

(a) (b) (c)

Figure 5.5: Evolution of the neutrino density matrix as a function of the (SM) neutrino temperature. The panels show the temperature dependence of the ν_e abundance (ρ_{ee}), the ν_μ abundance ($\rho_{\mu\mu}$), and the ν_s abundance (ρ_{ss}) in the 2+1 scenario for three different parameter points as indicated in the plots. The gray bands delimit the temperature ranges in which the system is evolved numerically. Panel (a) corresponds to evolution beyond the last crossing temperature, panels (b) and (c) correspond to evolution within the zero-crossing interval. Figure and caption (slightly modified) taken from [4].

eq. (5.2), $V_{\rm eff}$ approaches zero as the temperature approaches zero, while the term $m/2E \propto m/2T$ increases for low temperatures. Therefore, $V_{\rm eff}$ inevitably drops below $m/2E$ at low temperatures. The respective temperature at which this happens is denoted by "last crossing" temperature below. On the other hand, as mentioned above, $V_{\rm eff}$ changes sign at some temperature $T_s \sim M$, and hence necessarily crosses zero. If this zero crossing occurs at a higher temperatures than the last crossing temperature, $|V_{\rm eff}| \leq m/2E$ holds in a short interval, called "zero crossing" interval below. The two scenarios are illustrated in fig. 5.2: in both panels, the last crossing temperature is marked by a dashed, red line. In addition, in fig. 5.2 (b) the zero crossing occurs at a higher temperature than the last crossing temperature. The corresponding zero crossing interval is marked by two solid, red lines. Adopting the simplifying assumption from [4], the effect of $V_{\rm eff}$ is considered so strong that no sterile neutrinos are produced as long as eq. (5.3) holds, while $V_{\rm eff}$ is considered negligible as soon as eq. (5.3) ceases to hold.

Three representative results of the flavor evolution are shown in fig. 5.5, with the corresponding parameter values given in the legend in the respective plot. In each panel, the state of the system as a function of the active neutrino temperature T_ν is represented in terms of the number densities of each neutrino species i, given by the diagonal entries of ρ. The evolution of ρ in terms of t, given in eq. (5.9), was mapped on the corresponding temperature $T_\nu(t)$. The temperature ranges in which eq. (5.3) holds, and hence active-sterile conversions are prevented, are masked by a light gray layer. The first plot, fig. 5.5 (a) depicts the evolution of the number densities near the last crossing temperature, while the other two panels show the evolution of the number densities within the zero crossing interval. For the specific parameter values chosen in fig. 5.5 (a), the last crossing happens already at a high temperature $T_\nu \simeq 12\,\mathrm{MeV}$, and hence before the active neutrinos decouple from the thermal bath. Clearly, very rapidly flavor equilibrium is reached in this case, that is, all number densities converge to the same value. Since the active neutrinos are still coupled to the thermal bath, any active neutrino that converts into a sterile neutrino gets replaced because the active neutrino density is fixed by the thermal equilibrium. The situation is different in fig. 5.5 (b), where the evolution is shown at a temperature $T_\nu \simeq 0.8\,\mathrm{MeV}$, and hence after the decoupling of active neutrinos from the thermal bath. While also in this plot the flavor equilibrium is reached quasi-instantaneously, active neutrinos cannot be replenished anymore, and hence the number density in each active species decreases by one third, while the number density of the sterile neutrinos only increases to two thirds. Lastly, in fig. 5.5 (c), the evolution of the ρ_{ii} is shown for a value of the secret fine structure constant α_s, which is three orders of magnitude higher than in the previous panel fig. 5.5 (b). For this rather strong secret interaction, no flavor equilibrium is reached within the zero crossing interval depicted in fig. 5.5 (c) due to the quantum Zeno effect discussed above.

Irrespective of whether the active neutrinos are decoupled from the thermal bath at the corresponding temperature, the simulations presented in [4] prove that flavor equlibrium is always reached below the last crossing temperature. Regarding the zero crossing intervals, for a few cases the interval is either so short or the quantum Zeno effect is so strong, that flavor equilibrium is prevented. However, at most of the parameter points full flavor equilibrium is reached within the zero crossing interval. Hence, the recoupling temperatures calculated according to the first approach described above are potentially too low, because in that approach the zero crossing interval can not be accounted for. Therefore in [4], at each parameter point the recoupling temperature was compared to the result from the flavor evolution. If flavor equilibrium had been found due to the zero crossing of V_{eff} at a higher temperature than T_{rec} calculated in the first approach, that T_{rec} would have been corrected. However, no such case was found in [4]. Hence, although at almost all points of the parameter space effective production of sterile neutrinos occurs within the zero crossing interval, this effect is negligible when determining the recoupling temperature.

The result of the analysis drawing mainly on the first of the two approaches discussed above is presented in fig. 5.6. The three panels correspond to three

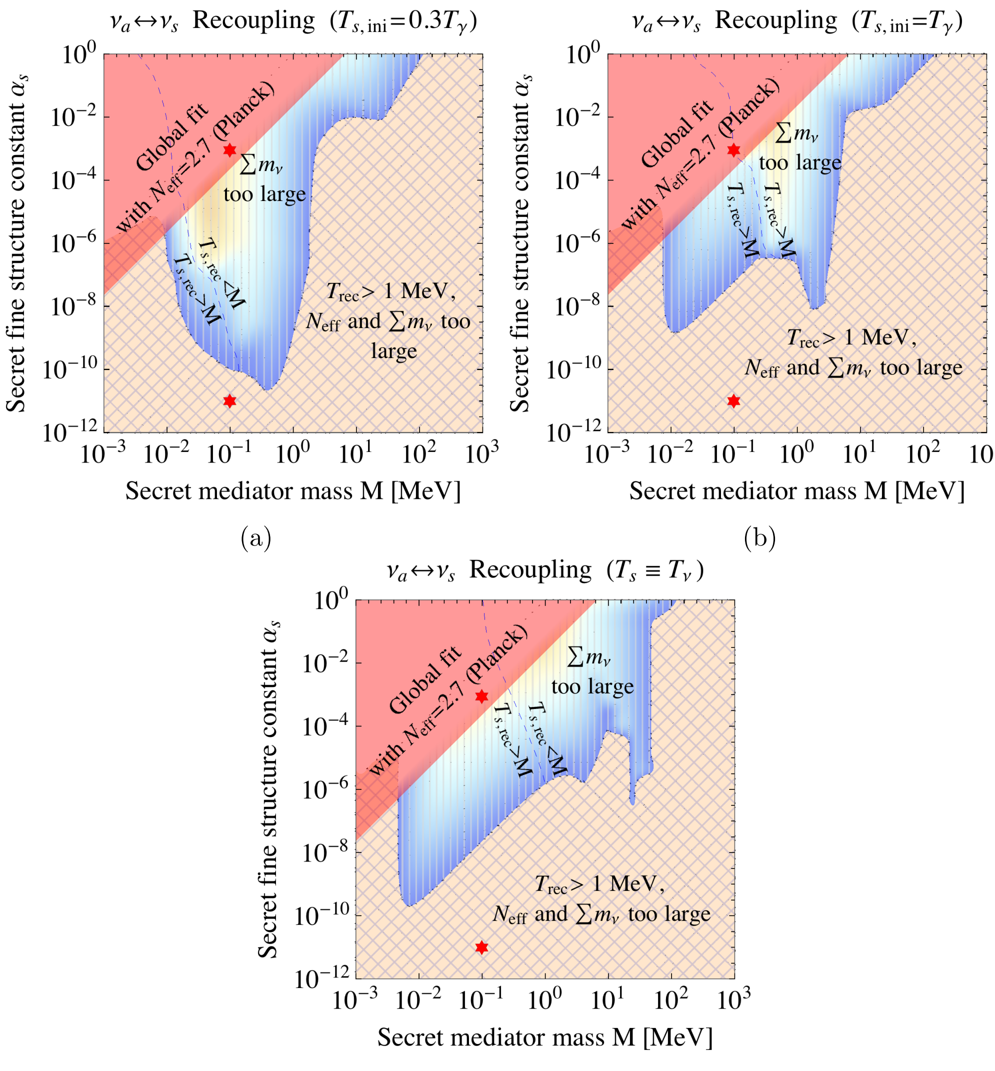

(a)

(b)

(c)

Figure 5.6: Parameter space spanned by he secret gauge boson mass M and the secret fine structure constant α_s, characterizing the secret interactions model defined in eq. (5.1). The panels present three different assumptions on the ratio of the sterile and active sector temperatures, which quantifies the initial conditions at very high temperatures. In this figure, the sterile neutrino mass is set to $m_s = 1\,\text{eV}$, and the vacuum mixing angle is set to $\theta_0 = 0.1$. The cross-hatched, brown region is ruled out because these parameters lead to recoupling at $T_\gamma > 1$ MeV, and hence before the active neutrinos decouple from the SM plasma. Therefore, also the sterile neutrinos thermalize with the SM plasma and need to be counted as an additional species of neutrino-like particles, conflicting the constraints on N_{eff}. Furthermore, in this case the assumption $m_s = 1\,\text{eV}$ for sterile neutrinos challenges the constraint on the sum of masses for neutrino-like particles. The vertically striped, blue and orange region is ruled out for the same reason, although here the constraints on N_{eff} do not apply, because recoupling occurs at $T_\gamma < 1$ MeV, and hence after the SM neutrinos have decoupled from the plasma [127]. The color gradient in this parameter region encodes the recoupling temperature ranging from 0.05 MeV shown in dark blue to 1 MeV shown in orange. In all of this parameter region, sterile neutrinos are still compatible with the bounds on the sum of neutrinos masses, if their mass is small enough, obeying $m_s \lesssim 0.2$ eV. The red shaded region at the top left of the plots is, according to the findings of [125], in conflict with constraints from CMB data on active neutrino free-streaming. Combining all results rules out the complete parameter space, because at no point recoupling can be evaded. This applies in particular for the two parameter points marked by red stars, although these were considered as favorable benchmark points in a previous publication [128] Figure taken from [4]

different initial conditions for the sterile neutrino temperature. The third possibility, denoted by $T_s \equiv T_\nu$, refers to the situation that the sterile neutrino temperature stays identical to the active neutrino temperature during the thermal history of the universe. This can be considered as a conservative limiting case. In all three panels, the mass of the sterile neutrino is assumed to be 1 eV, and the mixing angle is taken to be $\theta_0 = 0.1$. As already mentioned above, all the parameter points of the basic scenario are disfavored. However, the results presented in fig. 5.6(a) - (c) go beyond this simple statement to the extend that the cosmological measure conflicting with the basic scenario is determined at each parameter point in the plane spanned by α_s and M. The blue-yellow, vertically hatched regions in fig. 5.6 correspond to the parameter points at which mixing is efficiently suppressed until after active neutrino decoupling. In that case, N_{eff} is hardly affected by the presence of sterile neutrinos, however, the bounds on the sum of neutrino-like particles, including the sterile neutrino, strongly disfavor this region. The cross-hatched regions correspond to the parameter points at which recoupling occurs before active neutrinos decouple from the thermal bath. In that case, in addition to the constraints due to the bound on the combined mass of neutrino-like particles, N_{eff} is in strong tension with cosmological probes. Finally the red-shaded regions correspond to regions which are in tension with constraints on free-streaming according to a global fit performed in [125][4]. Comparing these results with fig. 5.4 reveals that much of the parameter space is actually excluded because of A'-mediated s-channel scattering, which can be resonantly enhanced, or A'-mediated t-channel scattering, which can be enhanced in the forward direction for low M, as discussed above.

The results presented in fig. 5.6 where cross-checked by the flavor-evolution approach. In particular, the flavor evolution proved the quasi-instantaneous recoupling limit, supplemented by the phenomenological formula eq. (5.8) to account for the quantum Zeno, effect to be a legitimate approximation. Lastly, no qualitative difference between the $1 + 1$ and the $2 + 1$ framework were found. Hence in conclusion, the sensitivity of the parameter space to the constraints from different cosmological observables presented in fig. 5.6 is robust with regard to the detailed method.

5.3 Extended scenarios with secret interactions

As described in the above section, the basic secret interaction scenario introduced in section 5.1 is excluded for all parameters explored in fig. 5.6. However,

---

[4] This global fit was performed for a value of 2.7 for N_{eff}, while N_{eff} is not expected to differ too much from 3 in the case at hand, because recoupling of the sterile neutrinos happens after the SM neutrinos have decoupled from the plasma. In the more recent publication [129], the respective limit is tightened by approximately a factor of two compared to the limit shown in fig. 5.6

there are many conceivable extensions of the basic scenario which are possibly less constrained. The following section briefly reviews several of these extended scenarios, which are discussed in greater detail in [4].

Since the bounds from cosmological probes apply to sterile neutrinos only once they are produced after recoupling with the active species, a straightforward scenario exempt from these bounds is one where the recoupling is prevented. This can be achieved by the mechanism of inverse symmetry breaking [130, 131, 132], where symmetries are intact at *low* temperatures while they get broken at *high* temperatures due to thermal corrections. If this mechanism is applied to the gauge boson corresponding to a Dirac-type mass term for sterile neutrinos, a high vev for the boson leads to a high mass for the sterile neutrino at high temperatures. If the sterile neutrino mass is high enough, this prevents their production possibly until after the rates of the processes that led to recoupling in the basic scenario have frozen out. At low temperatures, the thermal corrections to the gauge boson potential vanish, and hence the sterile neutrino looses its high mass due to the vev of the gauge boson field. Therefore at low temperatures, as for example during the oscillation experiments on earth, the phenomenology is the one discussed in chapter 4 for a light sterile neutrino. A toy model for such a scenario is explicitly constructed in [4], for a secret interaction mediated by a scalar mediator instead of the vector boson A' considered in the basic scenario above. This new secret interaction term then also serves as a Dirac-type mass term as long as the symmetry is broken at high temperatures. However, it was shown there that this particular toy model requires rather peculiar values for the respective model parameters. Nevertheless the calculations in [4] serve as a proof of principal that inverse symmetry breaking can indeed provide a model involving eV-scale sterile neutrinos which is compatible with constraints from cosmology.

A complementary idea to extend the basic scenario is to actually allow recoupling and hence the production of sterile neutrinos, but to evade constraints from cosmology due to additional processes occurring subsequently. As can be seen from fig. 5.6, there exists a considerable part of the parameter space which is compatible with the bounds on N_{eff} because recoupling happens after the active neutrinos have decoupled from the thermal bath. In particular, the vertically hatched region in fig. 5.6 conflict solely bounds on the sum of neutrino-like particles. However, as discussed in section 3.2, these bounds are to a large extend due to cosmological probes on structure formation. In detail, the evolution of LSS depends on the energy density in the respective states corresponding to a specific mass. If the energy density of the sterile neutrinos is very small, accordingly their impact on structure formation is small. A scenario encoding this possibility comprises several additional sterile neutrino states, all charged under the new gauge group $U(1)'$ and mixing with the active neutrinos. At recoupling, the energy is shared evenly between all neutrinos, and hence the energy density corresponding to each individual species is smaller. In particular it was shown in [4] that the energy density for each state after recoupling is $3\rho_{\mathrm{SM}}/(4+n)$, with n the number of additional sterile neutrinos and ρ_{SM} the energy density of the three active neutrinos before recoupling. Accordingly, assuming these additional sterile neutrinos to be quasi-massless, the bounds on the sum of the masses of the neutrino-like particles would be weakened by the factor $3/(4+n)$

Furthermore, an idea similar to the one outlined above can be evoked to reconcile secret interactions with the red shaded region in fig. 5.6. This region is disfavored by constraints on how much neutrino free-streaming may be reduced due to self-interaction. However, these bounds apply, as discussed in section 3.2.3, to any neutrino-like particle species. Therefore in models corresponding to this region of the parameter space, a second, very light sterile neutrino species or the secret gauge boson A' itself, if it is light enough, could partially thermalize before the heavier sterile neutrinos recouple. These additional light particles would then free-stream to some extent, and hence make up for the loss of free-streaming due to strong secret interaction.

Finally, an interesting extension of the basic scenario is the possibility of sterile neutrino decay, which is also motivated in the context of the anomalies in oscillation experiments [133]. If the decay was fast enough and the final particles were nearly massless, constraints on sterile neutrinos due to the bound on the sum of neutrino-like particles coming from probes on structure formation would not apply. An obvious candidate for such a decay process would be a three-body decay of the sterile neutrino of mass $\sim 1\,\mathrm{eV}$ associated with the oscillation experiment anomalies into a lighter sterile neutrino ν_s' via $\nu_s \to 2\nu_s' + \bar{\nu}_s'$ or $\nu_s \to \nu_s' + \gamma$. However, these processes, mediated by the secret gauge boson A' cannot provide for sufficiently high decay rates. Nevertheless, replacing the secret interaction term eq. (5.1) by the interaction term $y\phi(\bar{\nu}_s\gamma_5\nu_s')$, with coupling $y \gtrsim 10^{-13}$ and the pseudo-Goldstone boson ϕ, constitutes a viable model, where the lifetime of the eV-scale sterile neutrino is shorter than the time elapsed until recombination. Hence in such a scenario, bounds from the CMB or LSS formation on both, N_{eff} and the sum of masses of neutrino-like particles to not apply to the eV-scale neutrino, which has virtually decayed away by the time these probes are established.

In summary, the basic secret scenario described in section 5.1 can indeed suppress the production of sterile neutrinos in the early universe possibly until after the decoupling of the SM neutrinos, such that N_{eff} cannot change anymore. However, as discussed in section 5.2, even in that case the secret interactions lead to recoupling of the sterile neutrinos, mainly due to resonant s-channel and collinearly enhanced t-channel processes. This means that subsequent processes, in particular structure formation, are affected by the presence of the sterile neutrinos. This is, however, disfavored by cosmological probes, either because the sum of neutrino-like particles would be to high, or because the free-streaming bounds would be violated. The various cosmological constraints disfavor the complete parameter space, as can be observed in fig. 5.6. Nevertheless, although being less puristic, several possible extensions of the basic scenario have the potential of reconciling light sterile neutrinos with the bounds from cosmological probes. Therefore, from the perspective of cosmology the $3 + 1$ model discussed in chapter 4 cannot be considered to be excluded definitively. Moreover, some of these possible extensions of the secret interaction scenario might even provide auspicious models for decreasing the tensions observed within the oscillation data in the $3 + 1$ model.

This aspect is put into broader context in the next chapter, which provides a concluding discussion of the main results of this work, presented in the last chapter, chapter 4, and the current chapter, chapter 5.

6 Summary and conclusions

This work started out with the claim that neutrinos are very interesting objects to study, both theoretically and experimentally. As discussed in the introduction, open theoretical problems and unresolved experimental anomalies designate neutrinos as promising starting point in the search for new physics. Motivated especially by recent, rather ambiguous experimental reports, the investigations presented in this work align with that quest for new physics with neutrinos. In the following sections, the results of these investigations are summed up to arrive at the conclusions of this thesis.

Neutrinos are the only elementary particles for which the phenomenon of oscillations has been observed. The standard theory of neutrino oscillations, discussed in section 2.3 is in very good agreement with experimental results, as reported in section 2.5. Nevertheless, several apparently independent anomalies in different oscillation channels challenge the standard paradigm. In any case, however, the observed neutrino oscillations imply that the differences between the masses of at least three neutrino species have to be non-zero. Hence, at least two neutrinos are known to have mass. However, the SM provides no mechanism which would endow neutrinos with a mass. The development of a theoretical framework explaining neutrino masses is hence an important problem of theoretical physics. Section 2.2 presents a rather straightforward and minimalist model, which provides, however, the interesting possibility of neutrino oscillations involving, a fourth, sterile species. This model is called $3 + 1$ framework. It provides a theoretically well-motivated, straightforward extension of the SM which can account for oscillation phenomenology beyond the standard three flavor paradigm.

The question if the 3+1 framework is a viable model beyond the SM, consistent with all data, including the anomalies quoted above, is a central part of this thesis. Based on the publications [3] and [2], chapter 4 provides a detailed analysis of neutrino oscillation data in the $3 + 1$ framework.

At first, this analysis is confined to the data from reactor experiments. This is because the result of that subset of experiments can rather plausibly be attributed to a misprediction of the reactor antineutrino flux, as described in section 4.3.1. The explanation in terms of the $3 + 1$ model and the explanation in terms of a misprediction of the reactor antineutrino flux are cast into two hypotheses, which are subsequently tested against each other. This is possible because the precise measurement of the correlation between the composition of the reactor fuel and the detected rate reported by the Daya Bay collaboration allows for a disentanglement of the two hypotheses. In conclusions, the hypothesis of a wrong flux prediction is preferred over the $3+1$ framework when only considering a single rate measurement like Daya Bay. But also in this case, both hypotheses fit the data with a high GOF value. However, including experiments measuring spectra instead of mere rates drastically reduces this preference. Using the most recent, preliminary results from DANSS [50] even reverses the conclusion. However, on the basis of reactor data only, the most likely scenario is an improved reactor flux model in combination with the $3+1$ framework. Accordingly, when the flux model is left free to the fit in the "flux-free" approach explained in section 4.3.1, oscillations into sterile neutrinos are favored over the best fit flux model without such oscillations at the 2.9σ CL. This conclusion is mainly driven by the measurements of reactor spectra. Since the analysis of spectra is solely based on ratios, this result is independent from any concrete flux model. On the other hand, comitting to the flux predictions at face value would increase the evidence to 3.5σ.

The inclusion of the remaining data in the $\overset{(-)}{\nu}_e$ disappearance channel still allows for a rather consistent fit, although the reactor data and the data corresponding to the gallium anomaly are in slight tension quantified by a p-value of $p_{\mathrm{PG}} = 3.1\%$. Nevertheless, the evidence for the $3+1$ framework in the $\overset{(-)}{\nu}_e$ channel is between $\sim 3\sigma$ and $\sim 4\sigma$, depending on the reactor flux model. In this channel, the preferred parameters of the $3+1$ framework are $\Delta m^2_{41} \sim 1.3\,\mathrm{eV}^2$ and $|U_{e4}| \sim 0.1$.

Similarly, the combined fit to the global data in the $\overset{(-)}{\nu}_e$ appearance channel favors the $3+1$ framework over the standard oscillation model with a very high significance of up to 6.5σ, depending on which of the LSND datasets are included in the fit. The corresponding preferred parameters of the $3+1$ framework are $\Delta m^2_{41} \sim 0.6\,\mathrm{eV}^2$ and $4|U_{e4}|^2|U_{\mu 4}|^2 \sim 7 \times 10^{-3}$. Despite the strong evidence for the $3+1$ framework, a GOF value of 3.3% indicates, however, that this model cannot reproduce particular features of the data, especially in the MiniBooNE spectra.

By contrast, the $\overset{(-)}{\nu}_\mu$ channel provides no evidence at all for oscillations involving sterile neutrinos. Instead, in particular the most recent MINOS and IceCube data allow to derive stringent constraints on the parameter space of the $3+1$ framework in the $\overset{(-)}{\nu}_\mu$ channel. In this channel, almost uniformly across the valid range of Δm^2_{41}, the parameter $|U_{\mu 4}|$ is limited to less than $|U_{\mu 4}| \lesssim 0.1$. Obviously this strong limit in combination with the rather small value favored by the analysis in the $\overset{(-)}{\nu}_e$ disappearance channel is in conflict with the pronounced preference of the data in the $\overset{(-)}{\nu}_e$ appearance channel for a comparably high value of the product $4|U_{e4}|^2|U_{\mu 4}|^2$.

Indeed, the combined fit to the global data presented in section 4.7 proves that the different subsets are incompatible with each other at the 4.7σ CL. This conclusion is examined in detail by fitting various combination of experimental results. The corresponding PG values are reported in table 4.8. This table illustrates that neither removing individual datasets considered anomalous nor removing individual datasets contributing to the strong constraints on the $3+1$ framework relaxes this tension completely. Furthermore, as a comparison to table 4.7 reveals, the tension is rather independent from the underlying reactor flux model. The only experiment that leads to a significant improvement of the PG value when excluded from the global fit is LSND. On the other hand, discarding all data in the $\overset{(-)}{\nu}_\mu$ disappearance channel would also result in an acceptable PG value. However, no theoretical or experimental indication justifies the exclusion of this channel. Hence in conclusion, the tension in particular between the $\overset{(-)}{\nu}_\mu$ disappearance channel on the one hand and the $\overset{(-)}{\nu}_e$ appearance and $\overset{(-)}{\nu}_e$ disappearance channels on the other hand is mainly driven by LSND. However, even when the LSND data are discarded, significant tension remains due to the MiniBooNE results. This conclusion is robust with regard to the choice of the underlying dataset and the underlying reactor flux model. Therefore, the $3+1$ framework provides no consistent model for all the data measured in neutrino oscillation experiments. However, it provides a viable model for the global data, in particular including the gallium anomalies and the RAAs if the anomalies in the $\overset{(-)}{\nu}_e$ appearance channel are resolved independently. An investigation of these anomalies in the $\overset{(-)}{\nu}_e$ appearance channel, in particular with regard to the background estimation in MiniBooNE, is currently under way in the "Short-Baseline Neutrino Program" at Fermilab [134]. Hence new results expected in the next years might indeed resolve the anomalies in the $\overset{(-)}{\nu}_e$ appearance channel, which would require a stringent re-examination of the $3+1$ framework as fiducial model for neutrino oscillations.

While the $3+1$ framework thus still provides an interesting and viable model for at least a significant subset of the global data measured in neutrino oscillation experiments, the sterile neutrino introduced in this framework is in conflict with the constraints from cosmology. This is because the mixing parameter $|U_{e4}| \sim 0.1$ required to explain the RAA in the $3+1$ framework would result in an initial thermal equilibrium between the sterile neutrinos and the SM particles. Hence in this case, an additional species of neutrino-like particles exists in the early universe, which is in conflict with the bounds on N_{eff} reviewed in section 3.2.2. Similarly, the preferred mass parameter $\Delta m_{41}^2 \sim 1\,\text{eV}^2$ is in significant tension with the limits on the sum of masses of neutrino-like particles, $\sum m_\nu$, reviewed in section 3.2.4.

However, the various cosmological probes can only constrain the properties of particles that were present during the periods of time associated with these probes. Hence if the production of sterile neutrinos in the early universe was prevented, the tension with constraints on N_{eff} and $\sum m_\nu$ could be resolved. A rather minimalist mechanism that indeed can significantly suppress the production of sterile neutrinos is the secret interaction scenario introduced in section 5.1. In this scenario, by analogy to the SM MSW effect, coherent sterile neutrino scattering processes due to the secret interaction induce a temperature dependent, effective potential. This effective potential V_{eff} drastically decreases the mixing between SM neutrinos and sterile neutrinos at high temperatures. Consequently, the production of sterile neutrinos in the early universe is inhibited. However, as described in section 5.2, as soon as V_{eff} gets smaller, incoherent scattering processes and oscillations are no longer suppressed efficiently. The combination of these two processes gives rise to the Doddelson-Widrow mechanism, which brings sterile neutrinos into thermal equilibrium with the active neutrinos. Depending on when this recoupling occurs, different cosmological probes on N_{eff} and $\sum m_\nu$ are affected by the presence of sterile neutrinos and their corresponding constraints are no longer evaded. On the other hand, increasing the secret interaction strength, which decreases the effect of sterile neutrinos on the probes on N_{eff} and $\sum m_\nu$, reduces the free-streaming of active neutrinos due to the active-sterile mixing. But the free-streaming property of active neutrinos is also constrained tightly by cosmology, as explained in section 3.2.3, resulting again in strong tension with the secret interaction model. Thus, it was argued in the literature that the secret interaction scenario is ruled out at all points of parameter space.

Based on the publication [4], a major part of this thesis is dedicated to the reinvestigation of the secret interaction scenario. To this end, the recoupling of active and sterile neutrinos is explored by two complementary approaches. In the first approach, the recoupling temperature is explicitly calculated using analytic expressions for the scattering processes involving sterile neutrinos. Because this temperature determines when recoupling happens and hence which cosmological probes are affected, this approach allows to examine which constraint applies at a particular parameter point of the secret interaction scenario. The conclusion of this approach is that the secret interaction scenario is indeed ruled out at each point of the parameter space. In large parts this result is driven by the amplification of incoherent scattering due to a resonance in the s-channel and due to efficient collinear scattering in the t-channel. However, the particular constraints leading to the exclusion of an individual parameter point vary across the parameter space. The multi-flavor evolution used as the second approach provides a cross-check of these results. It is a numerically simulation of the evolution of the active and sterile neutrinos including oscillations and scattering. Hence, this approach captures the dynamics of the recoupling process, in particular its time dependence and the quantum Zeno effect. Both approaches are found to be in good agreement. Based on the combined results of both approaches the parameter space of the secret interaction model is classified into three regions which are ruled out due to constraints on free-streaming, constraints on $\sum m_\nu$ and constraints on $\sum m_\nu$ in combination with N_{eff}, respectively, as presented in fig. 5.6. This result provides a guideline indicating what extensions of the secret interaction model might still be compatible with the different cosmological constraints. Finally, the reinvestigation of the secret interactions scenario concludes by proposing three such potential extensions that could reconcile this scenario with cosmological constraints.

As cosmological probes constraining N_{eff} and $\sum m_\nu$ are only sensitive to sterile neutrinos after recoupling, these constraints can be avoided if recoupling is inhibited until very late times. This is possible in scenarios with inverse symmetry breaking, where a gauge symmetry is broken at high temperatures, resulting in a vev for the corresponding boson. At low temperatures the symmetry is restored and the vev vanishes. If the secret interaction is mediated by a scalar mediator instead of a vector mediator, the secret interaction term can serve as a Dirac mass term for the sterile neutrino at high temperatures. If the mass of the sterile neutrinos is high enough, their production is kinematically forbidden at high temperatures. On the other hand, sterile neutrinos could still be as light as required to explain the anomalies in the $3+1$ framework framework once the symmetry is restored at low temperatures. In conclusion, a very simplistic implementation of this model indeed prevents recoupling. However, the parameter values required in this model seem rather unnatural.

The secret interaction scenario is also reconciled with cosmological constraints if additional processes compensate or at least dilute the effect of sterile neutrinos on cosmological probes. Hence, a second extension of the secret interaction scenario introduces additional relativistic DOFs. These additional DOFs can be free-streaming and thus compensate for the reduction of free-streaming in the regions of the parameter space where the secret interaction would else be ruled out. On the other hand, the conflict of the secret interaction scenario with the constraints on $\sum m_\nu$ is mainly correlated with the energy density in the comparably heavy sterile neutrinos. Hence, if this energy density in the sterile neutrinos was very small, the bound on $\sum m_\nu$ would not be violated. This would be the case if the energy density in the neutrino sector was spread among a couple of additional, very light particles. This can be realized invoking additional sterile neutrinos charged under the secret gauge group. All sterile neutrinos would recouple only with the active neutrinos once these have decoupled from the thermal bath, such that the total energy density in the neutrino sector cannot change anymore. Thus, the energy density in each of the neutrino species, and consequently also in the critical sterile neutrino with $m \sim 1\,\text{eV}^2$ would be small and bounds on $\sum m_\nu$ could be evaded.

Finally, the possibility of sterile neutrino decay can potentially reconcile the secret interaction scenario with cosmological probes. If the decay was fast enough, no sterile neutrinos would exist throughout most of the thermal history of the universe. Consequently, similar to the inverse symmetry scenario, sterile neutrinos would not leave any imprints on cosmological probes. Independent from these considerations, sterile neutrino decay can be used to explain the SBL anomalies in the $\overset{(-)}{\nu}_e$ appearance channel, as was shown for example in [133].

In conclusion the investigations presented in this thesis prove that while new physics seems to be necessary in the neutrino sector, some of the most straightforward extensions of the SM are excluded by results in oscillation experiments and cosmological data. Within the $3+1$ framework the datasets corresponding to different oscillation channels are incompatible with each other. Furthermore, this model is in conflict with various constraints from cosmological probes. The secret interaction scenario, a minimalist extension that suppresses the production of sterile neutrinos in the early universe is not sufficient to reconcile active-sterile neutrino oscillations with cosmological constraints. Nevertheless, these models remain interesting, because the $3+1$ framework could serve as a consistent explanation for at least a subset of the global oscillation data, while several possible extensions of the secret interaction scenario could diminish the tensions with constraints from cosmology. In this regard it is particularly notable that the $3+1$ framework could provide a viable framework for the global oscillation data if the SBL anomalies in the $\overset{(-)}{\nu}_e$ channel measured by LSND and MiniBooNE could be accounted to a different physical process. Such a process could be fast sterile neutrino decay. On the other hand, sterile neutrino decay is one of the processes that can reconcile sterile neutrinos with cosmological constraints. Upcoming experimental results for example from the Short-Baseline Neutrino Program at Fermilab as well as new cosmological data will probe this scenario.

In summary the analyses presented in this thesis reject some straightforward and simplistic new physics models in the neutrino sector, whereas no evidence for a consistent theory of neutrino physics explaining all data was found. Therefore, neutrinos continue to be interesting objects to study, both, from a theoretical as well as from an experimental point of view. Finally, from a subjective perspective, the remaining open problems do not make neutrinos boring or annoying, but maybe the most exciting particles in the SM.

Bibliography

[1] A. Falkowski (Jester), "Résonaances particle physics blog." `https://resonaances.blogspot.com/2012/02/other-neutrino-anomalies.html`. Accessed 30 Oct 2018.

[2] M. Dentler, Á. Hernández-Cabezudo, J. Kopp, M. Maltoni, and T. Schwetz, "Sterile neutrinos or flux uncertainties? — Status of the reactor anti-neutrino anomaly," *JHEP*, vol. 11, p. 099, 2017.

[3] M. Dentler, Á. Hernández-Cabezudo, J. Kopp, P. Machado, M. Maltoni, I. Martinez-Soler, and T. Schwetz, "Updated Global Analysis of Neutrino Oscillations in the Presence of eV-Scale Sterile Neutrinos," *JHEP*, vol. 08, p. 010, 2018.

[4] X. Chu, B. Dasgupta, M. Dentler, J. Kopp, and N. Saviano, "Sterile Neutrinos with Secret Interactions–Cosmological Discord?," *arXiv preprint arXiv:1806.10629*, 2018.

[5] J. B. Bronzan, "Parametrization of SU (3)," *Physical Review D*, vol. 38, no. 6, p. 1994, 1988.

[6] A. Rasin, "Diagonalization of quark mass matrices and the Cabibbo-Kobayashi-Maskawa matrix," *arXiv preprint hep-ph/9708216*, 1997.

[7] M. Tanabashi *et al.*, "Review of particle physics," *Phys. Rev. D*, vol. 98, p. 030001, 2018.

[8] NobelPrize.org. Nobel Media AB 2018, "The Nobel Prize in Physics 2015." `https://www.nobelprize.org/prizes/physics/2015/summary/`. Accessed 18 Oct 2018.

[9] S. M. Bilenky, C. Giunti, and W. Grimus, "Phenomenology of neutrino oscillations," *Progress in Particle and Nuclear Physics*, vol. 43, pp. 1–86, 1999.

[10] V. Aseev, A. Belesev, A. Berlev, E. Geraskin, A. Golubev, N. Likhovid, V. Lobashev, A. Nozik, V. Pantuev, V. Parfenov, *et al.*, "Upper limit on the electron antineutrino mass from the Troitsk experiment," *Physical Review D*, no. 11, p. 112003, 2011.

[11] E. K. Akhmedov and A. Y. Smirnov, "Paradoxes of neutrino oscillations," *Physics of Atomic Nuclei*, vol. 72, no. 8, pp. 1363–1381, 2009.

[12] T. Kuo and J. Pantaleone, "Neutrino oscillations in matter," *Rev. Mod. Phys.*, vol. 61, p. 937, 1989.

[13] E. K. Akhmedov and J. Kopp, "Neutrino oscillations: Quantum mechanics vs. quantum field theory," *Journal of High Energy Physics*, vol. 2010, no. 4, p. 8, 2010.

[14] M. Beuthe, "Oscillations of neutrinos and mesons in quantum field theory," *Physics Reports*, vol. 375, no. 2-3, pp. 105–218, 2003.

[15] C. Jarlskog, "Commutator of the quark mass matrices in the standard electroweak model and a measure of maximal CP nonconservation," *Physical Review Letters*, vol. 55, no. 10, p. 1039, 1985.

[16] D. Nötzold and G. Raffelt, "Neutrino dispersion at finite temperature and density," *Nuclear Physics B*, vol. 307, no. 4, pp. 924–936, 1988.

[17] J. Kopp, "Theoretical Neutrino Physics." `https://www.staff.uni-mainz.de/jkopp/neutrino2015-material/neutrino-physics.pdf`. Johannes Gutenberg University, Mainz, Lecture notes.

[18] S. Bergmann, Y. Grossman, and E. Nardi, "Neutrino propagation in matter with general interactions," *Physical Review D*, vol. 60, no. 9, p. 093008, 1999.

[19] K. Kiers and N. Weiss, "Coherent neutrino interactions in a dense medium," *Physical Review D*, vol. 56, no. 9, p. 5776, 1997.

[20] M. E. Peskin and D. V. Schroeder, *An Introduction To Quantum Field Theory.* Westview Press Incorporated, 1995.

[21] A. Niemi and G. Semenoff, "Nucl. Phys. B230, 181 (1984).," *Nucl. Phys.*, vol. 230, p. 181, 1984.

[22] H. A. Weldon, "Effective fermion masses of order gT in high-temperature gauge theories with exact chiral invariance," *Phys. Rev. D*, vol. 26, pp. 2789–2796, Nov 1982.

[23] S. Mikheyev and A. Y. Smirnov, "Resonance enhancement of oscillations in matter and solar neutrino spectroscopy," *Yadernaya Fizika*, vol. 42, pp. 1441–1448, 1985.

[24] L. Wolfenstein, "Neutrino oscillations in matter," *Physical Review D*, vol. 17, no. 9, p. 2369, 1978.

[25] C. Giunti and M. Laveder, "Neutrino mixing," 2003.

[26] M. Tanabashi *et al.*, "Big-Bang Cosmology," in *Review of particle physics*, vol. 98, p. 030001, 2018.

[27] A. L. Besse, *Einstein manifolds.* Springer Science & Business Media, 2007.

[28] J. Lesgourgues and S. Pastor, "Massive neutrinos and cosmology," *Physics Reports*, vol. 429, no. 6, pp. 307–379, 2006.

[29] H. Kurki-Suonio, "Cosmological Perturbation Theory." `http://www.helsinki.fi/~hkurkisu/`. University of Helsinki, Lecture notes.

[30] S. Dodelson, *Modern cosmology.* Elsevier, 2003.

[31] H. Kurki-Suonio, "Cosmology I." `http://www.helsinki.fi/~hkurkisu/`. University of Helsinki, Lecture notes.

[32] M. Tanabashi *et al.*, "Neutrinos in Cosmology," in *Review of particle physics*, vol. 98, p. 030001, 2018.

[33] P. F. de Salas and S. Pastor, "Relic neutrino decoupling with flavour oscillations revisited," *Journal of Cosmology and Astroparticle Physics*, vol. 2016, no. 07, p. 051, 2016.

[34] M. Tanabashi *et al.*, "Big-Bang Nucleosynthesis," in *Review of particle physics*, vol. 98, p. 030001, 2018.

[35] R. Tojeiro, "Understanding the CMB temperature power spectrum." `http://www.roe.ac.uk/ifa/postgrad/pedagogy/2006_tojeiro.pdf`, 2006. Pedagogical seminar at the University of Edinburgh.

[36] M. Tanabashi *et al.*, "Cosmic microwave background," in *Review of particle physics*, vol. 98, p. 030001, 2018.

[37] S. Bashinsky and U. Seljak, "Signatures of relativistic neutrinos in CMB anisotropy and matter clustering," *Physical Review D*, vol. 69, no. 8, p. 083002, 2004.

[38] N. Aghanim *et al.*, "Planck 2018 results. VI. Cosmological parameters," *arXiv preprint arXiv:1807.06209*, 2018.

[39] P. A. Ade *et al.*, "Planck 2015 results-xiii. cosmological parameters," *Astronomy & Astrophysics*, vol. 594, p. A13, 2016.

[40] W. Hu, "CMB Tutorials." `http://background.uchicago.edu/index.html`. Introductory material on CMB physics.

[41] S. M. Bilenky, C. Giunti, and W. Grimus, "Phenomenology of neutrino oscillations," *Prog. Part. Nucl. Phys.*, vol. 43, pp. 1–86, 1999.

[42] P. Huber, J. Kopp, M. Lindner, M. Rolinec, and W. Winter, "New features in the simulation of neutrino oscillation experiments with GLoBES 3.0: General Long Baseline Experiment Simulator," *Comput. Phys. Commun.*, vol. 177, pp. 432–438, 2007.

[43] P. Huber, M. Lindner, and W. Winter, "Simulation of long-baseline neutrino oscillation experiments with GLoBES (General Long Baseline Experiment Simulator)," *Comput. Phys. Commun.*, vol. 167, p. 195, 2005.

[44] M. Maltoni and T. Schwetz, "Testing the statistical compatibility of independent data sets," *Phys. Rev.*, vol. D68, p. 033020, 2003.

[45] P. Huber, "On the determination of anti-neutrino spectra from nuclear reactors," *Phys.Rev.*, vol. C84, p. 024617, 2011.

[46] T. Mueller, D. Lhuillier, M. Fallot, A. Letourneau, S. Cormon, *et al.*, "Improved Predictions of Reactor Antineutrino Spectra," *Phys.Rev.*, vol. C83, p. 054615, 2011.

[47] G. Mention, M. Vivier, J. Gaffiot, T. Lasserre, A. Letourneau, and T. Materna, "Reactor antineutrino shoulder explained by energy scale nonlinearities?," *Phys. Lett.*, vol. B773, pp. 307–312, 2017.

[48] F. P. An *et al.*, "Evolution of the Reactor Antineutrino Flux and Spectrum at Daya Bay," *Phys. Rev. Lett.*, vol. 118, no. 25, p. 251801, 2017.

[49] M. Danilov, "Search for sterile neutrinos at the DANSS and Neutrino-4 experiments," 2017. talk given on behalf of the DANSS Collaboration at the 52nd Rencontres de Moriond EW 2017, La Thuile, Italy; `https://indico.in2p3.fr/event/13763/`.

[50] M. Danilov, "Search for sterile neutrinos at the DANSS experiment," 2017. talk given on behalf of the DANSS Collaboration at the Solvay Workshop 'Beyond the Standard model with Neutrinos and Nuclear Physics', 29 Nov.–1 Dec. 2017, Brussels, Belgium.

[51] J. Kopp, P. A. N. Machado, M. Maltoni, and T. Schwetz, "Sterile Neutrino Oscillations: The Global Picture," *JHEP*, vol. 1305, p. 050, 2013.

[52] H. Kwon, F. Boehm, A. Hahn, H. Henrikson, J. Vuilleumier, *et al.*, "Search for neutrino oscillations at a fission reactor," *Phys.Rev.*, vol. D24, pp. 1097–1111, 1981.

[53] G. Zacek *et al.*, “Neutrino Oscillation Experiments at the Gosgen Nuclear Power Reactor,” *Phys.Rev.*, vol. D34, pp. 2621–2636, 1986.

[54] G. Vidyakin, V. Vyrodov, I. Gurevich, Y. Kozlov, V. Martemyanov, *et al.*, “DETECTION OF ANTI-NEUTRINOS IN THE FLUX FROM TWO REACTORS,” *Sov.Phys.JETP*, vol. 66, pp. 243–247, 1987.

[55] G. S. Vidyakin *et al.*, “Limitations on the characteristics of neutrino oscillations,” *JETP Lett.*, vol. 59, pp. 390–393, 1994. [Pisma Zh. Eksp. Teor. Fiz.59,364(1994)].

[56] Yu. V. Kozlov *et al.*, “Today and Future Neutrino Experiments at Krasnoyarsk Nuclear Reactor,” *Nucl. Phys. Proc. Suppl.*, vol. 87, pp. 514–516, 2000.

[57] A. Afonin, S. Ketov, V. Kopeikin, L. Mikaelyan, M. Skorokhvatov, *et al.*, “A study of the reaction $\bar{\nu}_e + p \to e^+ + n$ on a nuclear reactor,” *Sov.Phys.JETP*, vol. 67, pp. 213–221, 1988.

[58] A. Kuvshinnikov, L. Mikaelyan, S. Nikolaev, M. Skorokhvatov, and A. Etenko, “Measuring the $\bar{\nu}_e + p \to n + e^+$ cross-section and beta decay axial constant in a new experiment at Rovno NPP reactor. (In Russian),” *JETP Lett.*, vol. 54, pp. 253–257, 1991.

[59] Y. Declais, J. Favier, A. Metref, H. Pessard, B. Achkar, *et al.*, “Search for neutrino oscillations at 15-meters, 40-meters, and 95-meters from a nuclear power reactor at Bugey,” *Nucl.Phys.*, vol. B434, pp. 503–534, 1995.

[60] Y. Declais, H. de Kerret, B. Lefievre, M. Obolensky, A. Etenko, *et al.*, “Study of reactor anti-neutrino interaction with proton at Bugey nuclear power plant,” *Phys.Lett.*, vol. B338, pp. 383–389, 1994.

[61] Z. Greenwood, W. Kropp, M. Mandelkern, S. Nakamura, E. Pasierb-Love, *et al.*, “Results of a two position reactor neutrino oscillation experiment,” *Phys.Rev.*, vol. D53, pp. 6054–6064, 1996.

[62] Y. J. Ko *et al.*, “Sterile Neutrino Search at the Neos Experiment,” *Phys. Rev. Lett.*, vol. 118, no. 12, p. 121802, 2017.

[63] F. P. An *et al.*, “Improved Measurement of the Reactor Antineutrino Flux and Spectrum at Daya Bay,” *Chin. Phys.*, vol. C41, no. 1, p. 013002, 2017.

[64] C. Giunti, “Precise Determination of the ^{235}U Reactor Antineutrino Cross Section Per Fission,” *Phys. Lett.*, vol. B764, pp. 145–149, 2017.

[65] H. Seo, “New Results from RENO,” 2017. talk given on behalf of the RENO Collaboration at the EPS conference on High Energy Physics, Venice, Italy, July 5–11, 2017.

[66] S.-H. Seo, “New Results from RENO,” 2014. talk given on behalf of the RENO Collaboration at the XXVI International Conference on Neutrino Physics and Astrophysics, Boston, USA, June 2–7, 2014.

[67] F. P. An *et al.*, “Measurement of Electron Antineutrino Oscillation Based on 1230 Days of Operation of the Daya Bay Experiment,” *Phys. Rev.*, vol. D95, no. 7, p. 072006, 2017.

[68] A. Gando *et al.*, “Constraints on θ_{13} from A Three-Flavor Oscillation Analysis of Reactor Antineutrinos at KamLAND,” *Phys.Rev.*, vol. D83, p. 052002, 2011.

[69] B. T. Cleveland *et al.*, “Measurement of the solar electron neutrino flux with the Homestake chlorine detector,” *Astrophys. J.*, vol. 496, pp. 505–526, 1998.

[70] F. Kaether, W. Hampel, G. Heusser, J. Kiko, and T. Kirsten, “Reanalysis of the GALLEX solar neutrino flux and source experiments,” *Phys.Lett.*, vol. B685, pp. 47–54, 2010.

[71] J. N. Abdurashitov *et al.*, “Measurement of the solar neutrino capture rate with gallium metal. III: Results for the 2002–2007 data-taking period,” *Phys. Rev.*, vol. C80, p. 015807, 2009.

[72] J. Hosaka *et al.*, “Solar neutrino measurements in Super-Kamiokande-I,” *Phys. Rev.*, vol. D73, p. 112001, 2006.

[73] J. P. Cravens *et al.*, “Solar neutrino measurements in Super-Kamiokande-II,” *Phys. Rev.*, vol. D78, p. 032002, 2008.

[74] K. Abe *et al.*, “Solar neutrino results in Super-Kamiokande-III,” *Phys.Rev.*, vol. D83, p. 052010, 2011.

[75] Y. Nakano, *^8B solar neutrino spectrum measurement using Super-Kamiokande IV.* PhD thesis, Tokyo U., 2016-02.

[76] B. Aharmim *et al.*, “Measurement of the nu/e and total B-8 solar neutrino fluxes with the Sudbury Neutrino Observatory phase I data set,” *Phys. Rev.*, vol. C75, p. 045502, 2007.

[77] B. Aharmim *et al.*, “Electron energy spectra, fluxes, and day-night asymmetries of B-8 solar neutrinos from the 391-day salt phase SNO data set,” *Phys. Rev.*, vol. C72, p. 055502, 2005.

[78] B. Aharmim *et al.*, “An Independent Measurement of the Total Active ^{8}B Solar Neutrino Flux Using an Array of ^{3}He Proportional Counters at the Sudbury Neutrino Observatory,” *Phys. Rev. Lett.*, vol. 101, p. 111301, 2008.

[79] G. Bellini *et al.*, “Precision measurement of the ^{7}Be solar neutrino interaction rate in Borexino,” *Phys.Rev.Lett.*, vol. 107, p. 141302, 2011.

[80] G. Bellini *et al.*, “Measurement of the solar ^{8}B neutrino rate with a liquid scintillator target and 3 MeV energy threshold in the Borexino detector,” *Phys.Rev.*, vol. D82, p. 033006, 2010.

[81] G. Bellini *et al.*, “Neutrinos from the primary proton–proton fusion process in the Sun,” *Nature*, vol. 512, no. 7515, pp. 383–386, 2014.

[82] J. Reichenbacher, *Final KARMEN results on neutrino oscillations and neutrino nucleus interactions in the energy regime of supernovae.* PhD thesis, Karlsruhe U., 2005.

[83] B. Armbruster, I. Blair, B. Bodmann, N. Booth, G. Drexlin, *et al.*, “KARMEN limits on $\nu_e \to \nu_\tau$ oscillations in two neutrino and three neutrino mixing schemes,” *Phys.Rev.*, vol. C57, pp. 3414–3424, 1998.

[84] J. Conrad and M. Shaevitz, “Limits on Electron Neutrino Disappearance from the KARMEN and LSND ν_e–Carbon Cross Section Data,” *Phys.Rev.*, vol. D85, p. 013017, 2012. Published version.

[85] L. Auerbach *et al.*, “Measurements of charged current reactions of ν_e on ^{12}C,” *Phys.Rev.*, vol. C64, p. 065501, 2001.

[86] W. Hampel *et al.*, “Final results of the Cr-51 neutrino source experiments in GALLEX,” *Phys.Lett.*, vol. B420, pp. 114–126, 1998.

[87] J. Abdurashitov *et al.*, “Measurement of the response of the Russian-American gallium experiment to neutrinos from a Cr-51 source,” *Phys.Rev.*, vol. C59, pp. 2246–2263, 1999.

[88] J. Abdurashitov, V. Gavrin, S. Girin, V. Gorbachev, P. Gurkina, *et al.*, “Measurement of the response of a Ga solar neutrino experiment to neutrinos from an Ar-37 source,” *Phys.Rev.*, vol. C73, p. 045805, 2006.

[89] C. Giunti and Y. F. Li, “Matter Effects in Active-Sterile Solar Neutrino Oscillations,” *Phys. Rev.*, vol. D80, p. 113007, 2009.

[90] D. Frekers, H. Ejiri, H. Akimune, T. Adachi, B. Bilgier, *et al.*, “The Ga-71(He-3, t) reaction and the low-energy neutrino response,” *Phys.Lett.*, vol. B706, pp. 134–138, 2011.

[91] M. Maltoni and T. Schwetz, "Sterile neutrino oscillations after first MiniBooNE results," *Phys. Rev.*, vol. D76, p. 093005, 2007.

[92] A. A. Aguilar-Arevalo *et al.*, "Observation of a Significant Excess of Electron-Like Events in the MiniBooNE Short-Baseline Neutrino Experiment," May 2018.

[93] A. Aguilar-Arevalo *et al.*, "Improved Search for $\bar{\nu}_\mu \to \bar{\nu}_e$ Oscillations in the MiniBooNE Experiment," *Phys.Rev.Lett.*, vol. 110, p. 161801, 2013.

[94] "Data release for arXiv:1207.4809." `http://www-boone.fnal.gov/for_physicists/data_release/nue_nuebar_2012/combined.html#fit200`.

[95] A. Aguilar *et al.*, "Evidence for neutrino oscillations from the observation of $\bar{\nu}_e$ appearance in a $\bar{\nu}_\mu$ beam," *Phys. Rev.*, vol. D64, p. 112007, 2001.

[96] B. Armbruster *et al.*, "Upper limits for neutrino oscillations muon-antineutrino to electron-antineutrino from muon decay at rest," *Phys. Rev.*, vol. D65, p. 112001, 2002.

[97] P. Astier *et al.*, "Search for $\nu_\mu \to \nu_e$ oscillations in the NOMAD experiment," *Phys.Lett.*, vol. B570, pp. 19–31, 2003.

[98] L. Borodovsky, C. Chi, Y. Ho, N. Kondakis, W.-Y. Lee, *et al.*, "Search for muon-neutrino oscillations $\nu_\mu \to \nu_e(\bar{\nu}_\mu \to \bar{\nu}_e)$ in a wide-band neutrino beam," *Phys.Rev.Lett.*, vol. 68, pp. 274–277, 1992.

[99] M. Antonello *et al.*, "Experimental Search for the "LSND Anomaly" with the Icarus Detector in the CNGS Neutrino Beam," *Eur. Phys. J.*, vol. C73, no. 3, p. 2345, 2013.

[100] C. Farnese, "Some recent results from ICARUS," *AIP Conf. Proc.*, vol. 1666, p. 110002, 2015. see also slides available from `https://indico.fnal.gov/materialDisplay.py?contribId=265&sessionId=18&materialId=slides&confId=8022`.

[101] N. Agafonova *et al.*, "Search for $\nu_\mu \to \nu_e$ oscillations with the OPERA experiment in the CNGS beam," *JHEP*, vol. 07, p. 004, 2013. [Addendum: JHEP07,085(2013)].

[102] M. G. Aartsen *et al.*, "Searches for Sterile Neutrinos with the Icecube Detector," *Phys. Rev. Lett.*, vol. 117, no. 7, p. 071801, 2016. Data accessible at `http://icecube.wisc.edu/science/data/IC86-sterile-neutrino`.

[103] B. J. P. Jones, *Sterile neutrinos in cold climates.* PhD thesis, Massachusetts Institute of Technology, 2015. available from `http://hdl.handle.net/1721.1/101327`.

[104] C. A. Argüelles, *New Physics with Atmospheric Neutrinos.* PhD thesis, University of Wisconsin, Madison, 2015. available from `https://docushare.icecube.wisc.edu/dsweb/Get/Document-75669/tesis.pdf`.

[105] F. Dydak, G. Feldman, C. Guyot, J. Merlo, H. Meyer, *et al.*, "A Search for Muon-neutrino Oscillations in the Delta m**2 Range 0.3-eV**2 to 90-eV**2," *Phys.Lett.*, vol. B134, p. 281, 1984.

[106] A. A. Aguilar-Arevalo *et al.*, "A Search for muon neutrino and antineutrino disappearance in MiniBooNE," *Phys.Rev.Lett.*, vol. 103, p. 061802, 2009.

[107] G. Cheng *et al.*, "Dual baseline search for muon antineutrino disappearance at 0.1 $\mathrm{eV}^2 < \Delta m^2 < 100\ \mathrm{eV}^2$," *Phys.Rev.*, vol. D86, p. 052009, 2012.

[108] "Data release for arXiv:0903.2465." `http://www-boone.fnal.gov/for_physicists/data_release/numu_numubar/`.

[109] R. Wendell *et al.*, "Atmospheric neutrino oscillation analysis with subleading effects in Super-Kamiokande I, II, and III," *Phys.Rev.*, vol. D81, p. 092004, 2010.

[110] R. Wendell, "Atmospheric Results from Super-Kamiokande," *AIP Conf. Proc.*, vol. 1666, p. 100001, 2015. slides available at `https://indico.fnal.gov/event/8022/other-view?view=standard`.

[111] M. G. Aartsen *et al.*, "Determining neutrino oscillation parameters from atmospheric muon neutrino disappearance with three years of IceCube DeepCore data," *Phys. Rev.*, vol. D91, no. 7, p. 072004, 2015.

[112] J. P. Yañez *et al.*, "IceCube Oscillations: 3 years muon neutrino disappearance data." `http://icecube.wisc.edu/science/data/nu_osc`.

[113] P. Adamson *et al.*, "Search for Active-Sterile Neutrino Mixing Using Neutral-Current Interactions in NOvA," *Phys. Rev.*, vol. D96, no. 7, p. 072006, 2017.

[114] P. Adamson *et al.*, "Search for Sterile Neutrinos in MINOS and MINOS+ Using a Two-Detector Fit," *Submitted to: Phys. Rev. Lett.*, 2017.

[115] S. M. Bilenky, C. Giunti, W. Grimus, and T. Schwetz, "Four neutrino mass spectra and the Super-Kamiokande atmospheric up - down asymmetry," *Phys. Rev.*, vol. D60, p. 073007, 1999.

[116] H. Nunokawa, O. L. G. Peres, and R. Zukanovich Funchal, "Probing the Lsnd Mass Scale and Four Neutrino Scenarios with a Neutrino Telescope," *Phys. Lett.*, vol. B562, pp. 279–290, 2003.

[117] A. Esmaili and A. Y. Smirnov, “Restricting the LSND and MiniBooNE sterile neutrinos with the IceCube atmospheric neutrino data,” *Journal of High Energy Physics*, vol. 2013, p. 14, Dec 2013.

[118] W. C. Louis, “Problems With the MINOS/MINOS+ Sterile Neutrino Muon-Neutrino Disappearance Result,” 2018.

[119] K. Kodama *et al.*, “Observation of tau neutrino interactions,” *Phys. Lett.*, vol. B504, pp. 218–224, 2001.

[120] M. Maltoni, T. Schwetz, M. A. Tortola, and J. W. F. Valle, “Ruling Out Four Neutrino Oscillation Interpretations of the LSND Anomaly?,” *Nucl. Phys.*, vol. B643, pp. 321–338, 2002.

[121] B. Dasgupta and J. Kopp, “Cosmologically Safe eV-Scale Sterile Neutrinos and Improved Dark Matter Structure,” *Phys. Rev. Lett.*, vol. 112, no. 3, p. 031803, 2014.

[122] S. Dodelson and L. M. Widrow, “Sterile-neutrinos as dark matter,” *Phys.Rev.Lett.*, vol. 72, pp. 17–20, 1994.

[123] N. Saviano, O. Pisanti, G. Mangano, and A. Mirizzi, “Unveiling secret interactions among sterile neutrinos with big-bang nucleosynthesis,” 2014.

[124] J. F. Cherry, A. Friedland, and I. M. Shoemaker, “Short-baseline neutrino oscillations, Planck, and IceCube,” 2016.

[125] F. Forastieri, M. Lattanzi, G. Mangano, A. Mirizzi, P. Natoli, and N. Saviano, “Cosmic microwave background constraints on secret interactions among sterile neutrinos,” 2017.

[126] G. Sigl and G. Raffelt, “General kinetic description of relativistic mixed neutrinos,” *Nuclear Physics B*, no. 1, pp. 423–451.

[127] A. Mirizzi, G. Mangano, O. Pisanti, and N. Saviano, “Tension between secret sterile neutrino interactions and cosmological neutrino mass bounds,” 2014.

[128] X. Chu, B. Dasgupta, and J. Kopp, “Sterile Neutrinos with Secret Interactions - Lasting Friendship with Cosmology,” 2015.

[129] N. Song, M. Gonzalez-Garcia, and J. Salvado, “Cosmological constraints with self-interacting sterile neutrinos,” *arXiv preprint arXiv:1805.08218*, 2018.

[130] S. Weinberg, “Gauge and Global Symmetries at High Temperature,” *Phys. Rev.*, vol. D9, pp. 3357–3378, 1974.

[131] R. N. Mohapatra and G. Senjanovic, "Broken Symmetries at High Temperature," *Phys. Rev.*, vol. D20, pp. 3390–3398, 1979.

[132] B. Bajc, "High temperature symmetry nonrestoration," in *Proceedings, 3rd International Conference on Particle Physics and the Early Universe (COSMO 1999): Trieste, Italy, September 27-October 3, 1999*, pp. 247–253, 2000.

[133] Y. Bai, R. Lu, S. Lu, J. Salvado, and B. A. Stefanek, "Three Twin Neutrinos: Evidence from LSND and MiniBooNE," 2015.

[134] M. Antonello *et al.*, "A Proposal for a Three Detector Short-Baseline Neutrino Oscillation Program in the Fermilab Booster Neutrino Beam," 2015.